

Fatigue of skin-stiffener intersections in composite wind turbine blade structures
by Robert B Morehead, III

A thesis submitted in partial fulfillment of the requirements for the degree of Master of Science in Mechanical Engineering
Montana State University
© Copyright by Robert B Morehead, III (2000)

Abstract:
This thesis is a combined experimental and finite element modeling study of the fatigue resistance of skin-stiffener substructures for wind turbine blades. Composite wind turbine blades possess a stiffening spar running the length of the blade to transfer shear and resist buckling. The interface at the stiffener and skin is a region that has large out-of-plane stresses which initiate fracture due to the relatively low transverse strength properties of laminated composites. Design lifetimes of a wind turbine blade include more cycles than those of the typical aircraft, bridge, or helicopter structures. Damage can initiate at very low stresses in turbine blades due to repeated loading over the turbine lifetime.

Initial damage sites in skin-stiffeners were experimentally determined. Damage initiation, propagation, coalescence and failure in the skin-stiffener were observed. An interlaminar database consisting of crack growth curves was established for the design of substructure architectures.

A strength-based failure criterion was used to predict initial damage locations within the skin-stiffener. Fracture, mechanics was used to predict delamination growth after damage was present. Finite element results for critical strain energy release rates (Gi and GII) at the critical load for crack growth are compared with experimental GI and GII from double Cantilever Beam (DCB) and End-Notch Flexure (ENF) tests. The cracks in the skin-stiffener are mixed-mode, with both GI and GII components. The values of GI and GII calculated for the skin-stiffener at the static delamination load are far below the GIC and GIIC values from the interlaminar fracture tests for the same ply interface. Corresponding differences are observed at particular rates of fatigue crack growth. To rationalize the apparently very low G values for the skin-stiffener, the use of a mixed-mode criterion for crack growth has been investigated.

The effect of matrix resin toughness on the skin-stiffener fatigue lifetime has been investigated. Tougher resins produce stronger sections with greater fatigue resistance over the load range tested; the improvement from the tougher resins diminishes at lower loads and longer lifetimes. Design guidelines and numerical analysis methodologies have been established to predict skin-stiffener service lifetimes in typical wind turbine blade structures.

FATIGUE OF SKIN-STIFFENER INTERSECTIONS IN COMPOSITE WIND TURBINE BLADE STRUCTURES

by

Robert B. Morehead, III

A thesis submitted in partial fulfillment
of the requirements for the degree

of

Master of Science

in

Mechanical Engineering

MONTANA STATE UNIVERSITY-BOZEMAN
Bozeman, Montana

August 2000

N378
M8135

APPROVAL

of a thesis submitted by

Robert B. Morehead III

This thesis has been read by each member of the thesis committee and has been found to be satisfactory regarding content, English usage, format, citations, bibliographic style, and consistency, and is ready for submission to the College of Graduate Studies.

Dr. Douglas Cairns — Douglas S. Cairns — Chairperson, Graduate Committee — 9/11/00 — Date

Approved for the Department of Mechanical Engineering

Dr. Vic Cundy — Department Head — 9/14/00 — Date

Approved for the College of Graduate Studies

Dr. Bruce McLeod — Bruce R. McLeod — Graduate Dean — 9-14-00 — Date

STATEMENT OF PERMISSION TO USE

In presenting this thesis in partial fulfillment of the requirements for a master's degree at Montana State University-Bozeman, I agree that the Library shall make it available to borrowers under rules of the Library.

If I have indicated my intention to copyright this thesis by including a copyright notice page, copying is allowable only for scholarly purposes, consistent with "fair use" as prescribed in the U.S. Copyright Law. Requests for permission for extended quotation from or reproduction of this thesis in whole or in parts may be granted only by the copyright holder.

Signature Robert B Mahr III

Date 8/11/00

ACKNOWLEDGMENTS

I gratefully acknowledge the guidance of Dr. Douglas Cairns and Dr. John Mandell in this research effort. Their support and guidance throughout my graduate career have made this project possible. Thanks are directed to Dr. Robert Oakberg for serving as a graduate committee member. To Dan Samborsky, special thanks for your assistance in the Instron and Composite Laboratories toward the end of the experimental research. Finally, special thanks to my wife and friend, Rachel. Your support and love have always helped me to attain my goals and strive to always do my best.

This work was supported by the U.S. Department of Energy and the State of Montana through the Montana DOE EPSCoR Program (Contract # DEFC02-91ER75681) and Sandia National Laboratories.

TABLE OF CONTENTS

LIST OF TABLES vii

LIST OF FIGURES viii

ABSTRACT xi

1. INTRODUCTION 1
    Motivation and Approach 3

2. BACKGROUND 5
    Failure Criterion 6
    Fatigue 9
    Fracture Mechanics 11
        Mixed-Mode Fracture Criteria 13
        Numerical Methods to Predict Strain Energy Release Rates 14

3. EXPERIMENTAL METHODS 17
        Resin and Fabric Systems 17
        Manufacturing Equipment 18
        Testing Machines 20
        DCB and ENF Specimens 21
            Static DCB Test Procedure 30
            DCB Fatigue Test Procedure 31
            Static ENF Test Procedure 32
            ENF Fatigue Test Procedure 33
        Substructure Specimens 34
            Static Test Procedure 37
            Fatigue Test Procedure 38

4. NUMERICAL METHODS 40
    DCB Models 40
    Skin-Stiffener Models 45

5. EXPERIMENTAL RESULTS AND DISCUSSION 50
    Static G_I Crack Tests 50
        (90°/45°) Ply Interface 50
        (45°/45°) Ply Interface 51
    G_I Fatigue Crack Growth Tests 53
    Static G_{II} Crack Tests 56

G_{II} Fatigue Crack Growth Tests 59
Static Skin-Stiffener Tests 61
Ortho-Polyester Matrix 61
Resin Comparison for Static Tests 63
Skin-Stiffener Fatigue Tests 65
Ortho-Polyester Fatigue Tests 65
Resin Comparison Fatigue Tests 67

6. FINITE ELEMENT RESULTS AND CORRELATION WITH EXPERIMENTS 71
DCB Models 71
Skin-Stiffener Models 76
Static Skin-Stiffener Comparison 77
Skin-Stiffener Fatigue Comparison 83
Use of Methodology in Design 91

7. SUMMARY, CONCLUSIONS AND RECOMMENDATIONS 94
Experimental Summary and Conclusions 94
DCB and ENF Specimens 94
Skin-Stiffener Specimens 95
Numerical Techniques and Correlations with Experimental Results 95
Future Work 96

REFERENCES CITED 97

APPENDIX A
Test Results 100

APPENDIX B
Part A Static Sample Calculation 117
Part B Fatigue Sample Calculation 120

APPENDIX C
Determination of FEA Initial Crack Length 123

APPENDIX D
Sample FEA Batch File 127

APPENDIX E
Data Acquisition Programs 131

LIST OF TABLES

Table Page

1. Table of DCB and ENF Series ID and Motivation 28
2. Summary of Skin-Stiffener Test Matrix 36
3. Static Longitudinal, Transverse, and Simulated Shear Properties for D155 and DB120 Unidirectional Materials 43
4. Physical Elastic Constants for D155 Ortho-polyester Resin 44
5. G_{Ic} Values from Static DCB Tests 52
6. G_{IIc} Values for Static ENF Tests 59
7. Static Load and Crack Length Data for Ortho-polyester Skin-Stiffeners 62
8. Table of Load and Displacement Data for Different Resin Skin-Stiffener 64
9. Comparison of Three Methods for Calculation of G_I Values in DCB Specimens: MBT, 3-D FEA, and 2-D FEA (DCB Specimen 780 with a 42.7mm Crack Length) 74
10. Predicted Initial Damage Load and Location 80
11. Strain Energies for 129 N/cm Load and 2.48mm Crack in Bend Region of Skin-stiffener 81
12. G Values, Interaction Sums and Predicted Critical Loads for the FEA Skin-Stiffener Model 85
13. Strain Energies and Crack Length for DCB and ENF Crack Growth Compared with Skin-Stiffener Values at the Same Crack Growth Rate 87
14. Experimental and Predicted Loads for Different Crack Growth Rates in Bend Region of Cyclic Loaded Skin-stiffeners 87

LIST OF FIGURES

Figure Page

1. Cross Section of Wind Turbine Blade 2
2. Fiber and Transverse Directions in a Unidirectional Composite 5
3. Typical S-N Curve for Various Fatigue Driven Designs 9
4. Uniform Cyclic Loading of a Specimen 10
5. Fatigue Crack Growth Rate 11
6. Fracture Modes – Three Modes of Fracture 12
7. Normal Stress σ_y Distribution Ahead of the Crack Tip 15
8. 4-Noded Quadrilateral Finite Element 16
9. E-Glass Fabrics used in Test Specimens 18
10. Flat Plate RTM Mold for DCB and ENF Specimens 18
11. Peristaltic Pump and Skin-Stiffener Mold 19
12. Servo Electric Test Machine with 445 N Load Cell 20
13. Servo Hydraulic Test Machine 21
14. Double Cantilever Beam (DCB) Specimen 22
15. Typical Load versus Actuator Displacement Curve for DCB Specimen 23
16. Area Enclosed by Loading-Unloading Loop 24
17. Mode II Fracture Specimen Geometry 25
18. Typical Load versus Actuator Displacement Curve for an ENF Specimen 26
19. Typical Log-log Relationship between da/dN and ΔG 27
20. Scaled Loupe Used to Monitor Crack Fronts 29

21 DCB Test with Conductive Copper Tape 31

22. ENF Test in Progress 33

23. Skin-Stiffener Loading, Geometry and Dimensions 35

24. Test Apparatus used for ENF and Skin-Stiffener Specimens 36

25. Typical Skin-Stiffener Tensile Test 37

26. Typical Static Tensile Load versus Displacement Curve for Skin-Stiffener 38

27. 3-D DCB Model with Applied Loads and Constraints 41

28. 2-D DCB Model with Applied Loads and Constraints 42

29. Symmetric Finite Element Model for Skin-Stiffener 46

30. Coordinate Systems and Mesh for Symmetric Skin-Stiffener Model 47

31. FEA Model for Crack Propagation 48

32. Coordinate System and Mesh for Skin-Stiffener Crack Propagation 49

33. G_{Ic} Fracture Toughness versus Crack Extension 51

34. Detail of Static Crack, (90°/45°) Interface, DCB Specimen 53

35. Detail of Fatigue Crack, (90°/45°) Interface, DCB Specimen 54

36. Mode I – (da/dN) versus G_{Imax}. $[(45)_9,90,(45)_8]$ Laminates Cracked in the (90°/45°) Interface. Short Crack Data (below 5 mm), R = 0.1, DCB Specimen 55

37. Typical Load versus Actuator Displacement for an ENF Specimen 57

38. ENF Test in Progress with Stable Crack Growth 57

39. Detail of Static Crack during Stable Crack Growth, ENF Specimen 58

40. Crack Growth Rate versus G_{IImax}, R = 0.1, ENF Specimens 60

41. Detail of Fatigue Crack Front ENF Specimen 59

42. Location of Delamination and Nomenclature for Crack Fronts 62

43. Load versus Displacement for 8084 Vinyl Ester Skin-Stiffener 64

44. Skin-Stiffener Crack Sequence during Fatigue Loading 66

45. Ortho-polyester Skin-Stiffener Maximum Cyclic Displacement versus Number of Cycles 67

46. Crack Growth Rate versus G_{max} in (90°/45°) Interface for Ortho-polyester Skin-stiffeners 68

47. Maximum Cyclic Load versus Number of Cycles to reach a Deflection of 0.43 cm 69

48. Maximum Cyclic Load/Ultimate Load versus Number of Cycles to reach a Deflection of 0.43 cm 70

49. 3-D DCB FEA Model 72

50. Normalized Strain Energy Release Rate for DCB Model with a 42.7 mm Crack Length (3D Solid Elements) 73

51. G_{Ic} versus Crack Length Calculated by 2-D Plane Strain FEA Model and MBT (DCB 780 Specimen) 75

52. Deformed DCB Model with Transverse Stress Field Contour Plot 76

53. Comparison of Load versus Displacement for FEA Model and Three Experimental Ortho-polyester Skin-Stiffener Test Results 77

54. Skin-Stiffener Tangential Strain Plot at the Bend Region (no crack) 78

55. Skin-Stiffener Radial Strain Plot at the Bend Region (no crack) 79

56. FEA Tangential Strain Plot with Crack Front Locations 81

57. G_I and G_{II} versus Applied Load, Skin-Stiffener Geometry 82

58. Sequence of Events for Static Analysis of Skin-Stiffener 84

59. G_T versus Crack Length for Crack Front #2 86

60. Normalized G_I/G_T versus Crack Length for Crack Front #2 in Bend Region 86

61. (da/dN) versus (Maximum Cyclic Strain Energy/Average Static Strain Energy), Ortho-polyester Skin-Stiffener Specimens and ENF Specimens 89

62. (da/dN) versus Maximum Cyclic Strain Energy/Average Static Strain Energy), Ortho-polyester Skin-Stiffener Specimens and DCB Specimens 89

63. Sequence of Events for Fatigue Analysis of Skin-Stiffener 90

ABSTRACT

This thesis is a combined experimental and finite element modeling study of the fatigue resistance of skin-stiffener substructures for wind turbine blades. Composite wind turbine blades possess a stiffening spar running the length of the blade to transfer shear and resist buckling. The interface at the stiffener and skin is a region that has large out-of-plane stresses which initiate fracture due to the relatively low transverse strength properties of laminated composites. Design lifetimes of a wind turbine blade include more cycles than those of the typical aircraft, bridge, or helicopter structures. Damage can initiate at very low stresses in turbine blades due to repeated loading over the turbine lifetime.

Initial damage sites in skin-stiffeners were experimentally determined. Damage initiation, propagation, coalescence and failure in the skin-stiffener were observed. An interlaminar database consisting of crack growth curves was established for the design of substructure architectures.

A strength-based failure criterion was used to predict initial damage locations within the skin-stiffener. Fracture mechanics was used to predict delamination growth after damage was present. Finite element results for critical strain energy release rates (G_I and G_{II}) at the critical load for crack growth are compared with experimental G_I and G_{II} from double Cantilever Beam (DCB) and End-Notch Flexure (ENF) tests. The cracks in the skin-stiffener are mixed-mode, with both G_I and G_{II} components. The values of G_I and G_{II} calculated for the skin-stiffener at the static delamination load are far below the G_{Ic} and G_{IIc} values from the interlaminar fracture tests for the same ply interface. Corresponding differences are observed at particular rates of fatigue crack growth. To rationalize the apparently very low G values for the skin-stiffener, the use of a mixed-mode criterion for crack growth has been investigated.

The effect of matrix resin toughness on the skin-stiffener fatigue lifetime has been investigated. Tougher resins produce stronger sections with greater fatigue resistance over the load range tested; the improvement from the tougher resins diminishes at lower loads and longer lifetimes. Design guidelines and numerical analysis methodologies have been established to predict skin-stiffener service lifetimes in typical wind turbine blade structures.

CHAPTER 1

INTRODUCTION

Wind energy development has been expanding rapidly throughout the world for the last decade. The cost of wind generated power depends strongly on the cost and reliability of wind turbines [1]. Fiber-reinforced polymer composites are becoming the material of choice for turbine blades due to their superior in-plane mechanical properties, such as specific strength and stiffness, as well as the ability to tailor material characteristics for a particular design requirement. Montana State University has been pursuing studies of composite materials that are viable candidates for the wind turbine industry [2, 3]. A greater understanding of composites and their respective manufacturing processes could reduce costs and increase blade reliability.

The reliability of composite structures depends significantly on the design of the specific structural details in load transfer areas. Most wind turbine blades are designed with a longitudinal stiffening spar that is bonded to the skin as shown in Figure 1. The spar resists buckling and transfers shear loading through the blade.

Stress conditions near the fillet of the spar produce a multi-axial stress state, including interlaminar (thickness direction) stresses which can nucleate crack initiation and growth under fatigue loading. Composite wind turbine blades share many of the structural components and loading conditions that are common in fixed wing aircraft and rotorcraft structures.

Over the years, there have been a number of fatigue failures in aircraft. The British Comet I was the first commercial jet passenger aircraft. Two of these crashed in

1954, one of them four days following an inspection. The wreckage was examined carefully and the conclusion reached that the pressurized cabin had failed, beginning with small cracks at the corner of a window. Each pressurization and return to atmospheric pressure at landing represented a cycle of stressing, of which there had been 1290 in one plane and 900 in the other plane. All Comet aircraft of the type were grounded and fatigue became the focus of increased study [4]. One of the major aspects of the findings

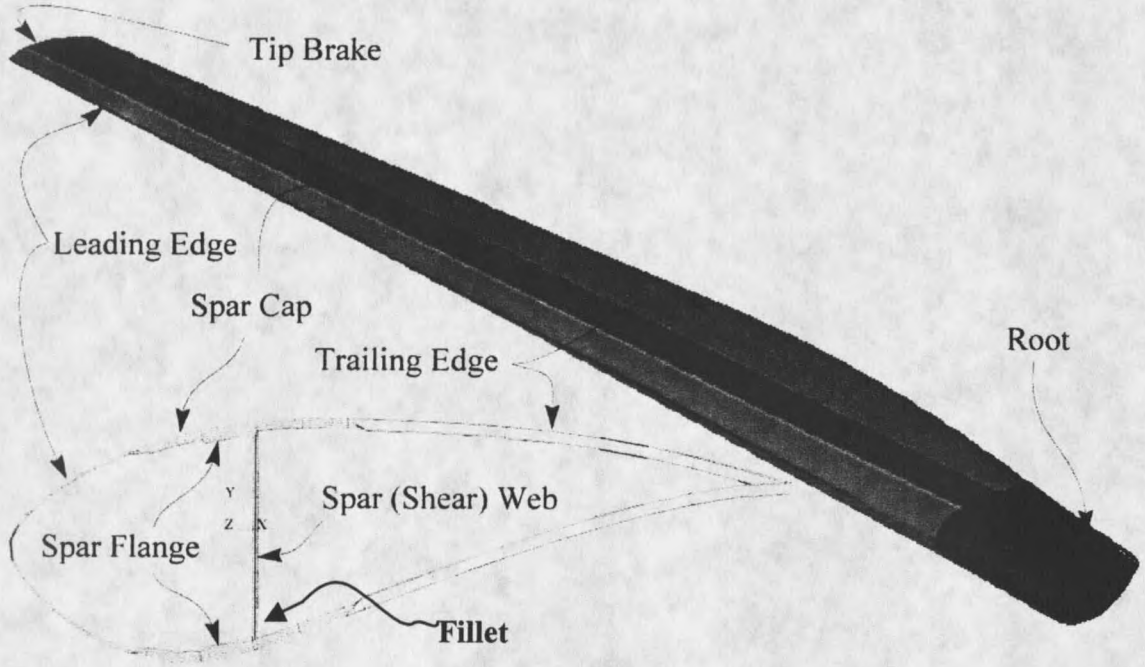


Figure 1. Cross Section of Wind Turbine Blade

was that the use of new materials accelerated crack growth. It is desired to mitigate any similar scenarios with this study.

Blade designs must strive to minimize weight and cost, making a more efficient

power generator, but they must also provide a durable structure with adequate life expectancy. The successful design must possess a combination of efficiency and reliability. The turbine must be efficient, minimum cost and weight, to compete with traditional power sources, but must be durable enough to withstand 30-40 years of service. Over the past ten years, Montana State University has performed research to produce a database of material properties and fatigue performance characteristics of composite material candidates for use in the wind turbine industry [3]. However, complex structural details such as skin-stiffener intersections, where out-of-plane stresses are important, cannot be designed directly with the database of in-plane properties.

Motivation and Approach

Previous research has focused on predicting quasi-static fracture of the critical skin-stiffener intersections using finite element analysis and experimental validation [5]. To ensure cost effective efficient designs, wind turbine blades must endure service loading lives beyond typical fatigue driven designs. This, along with an absence of adequate understanding of the damage mechanics that lead to fatigue failure in detail regions of blades, gives motivation for this thesis.

In order to investigate the fatigue failures in detail regions, an approach combining experimental fatigue testing and numerical analysis was employed. Initial damage sites in skin-stiffeners were experimentally determined. Damage propagation, coalescence and failure of the stiffener were observed. An interlaminar database consisting of crack growth curves was established for the analysis and design of

substructure architectures. Finite element model predictions for static and fatigue damage were compared with experimental results. The effects of matrix resin toughness on skin-stiffener performance were investigated for several resins. Design guidelines and numerical analysis methodologies were ultimately established to predict stiffener strength and damage growth rates.

CHAPTER 2

BACKGROUND

Addressed in this chapter are design issues associated with fatigue loading of skin-stiffeners and other detail regions. A discussion of common modes of failure and classical methods of analysis are presented.

A composite consists of a reinforcing phase, such as carbon or glass fibers, and a binder agent, or matrix, consisting of a thermoset or thermoplastic resin. Thermoset resins are the most common type of matrix system due to good "wet out" of fibers, low processing temperatures and generally lower cost than their thermoplastic counterparts. Unlike thermosets, thermoplastic resins are not cross-linked. Thus, upon heating, the thermoplastic polymer chains disentangle to form a viscous liquid. Since thermoplastics yield and can undergo large deformations, they are generally tougher than thermosets. However, their high viscosities create difficulties in processing.

Laminated composites inherently possess excellent properties in the fiber direction shown in Figure 2. Loaded perpendicular to the fiber direction, commonly referred to as the transverse direction, they exhibit poor mechanical properties. The load is not entirely carried by the fiber and ultimately gets transferred through the matrix material. As a result, properties perpendicular to the fibers are matrix driven. Similarly, loading perpendicular to the thickness direction can produce interlaminar cracking and peeling between the layers of layered composites.

Failure Criterion

Failure of fiber-reinforced materials is a complex topic, and is an ongoing activity.

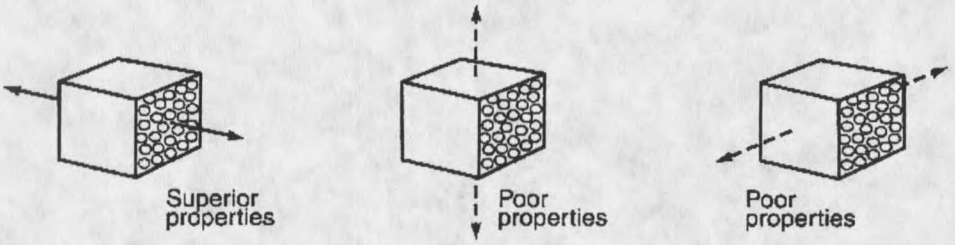


Figure 2. Fiber and Transverse Directions in a Unidirectional Composite [6]

There is not an all-encompassing orthotropic failure criterion that accurately predicts all modes of failure [6]. This statement also holds true for isotropic materials; some fail by yielding and others fail by brittle fracture. Composite failure criteria can be broken into two generalized catagories: compression and tension. Each of these catagories can be subdivided into matrix (through thickness and transverse) or fiber dominated failure.

The maximum strain failure criterion, as it applies to the plane-stress case, is stated by Hyer [6] as the following:

"A fiber-reinforced composite material in a general state of stress will fail when either:

1. The maximum strain in the fiber direction equals the maximum strain in a uniaxial specimen of the same material loaded in the fiber direction when it fails; or,

2. The maximum strain perpendicular to the fiber direction equals the maximum strain in a uniaxial specimen of the same material loaded perpendicular to the fiber direction when it fails; or,
3. The maximum shear strain in the 1-2 plane equals the maximum shear strain in a specimen of the same material loaded in shear in the 1-2 plane when it fails."

Thus, the material will not fail when

$$\varepsilon_1^C < \varepsilon_1 < \varepsilon_1^T \quad (1)$$

$$\varepsilon_2^C < \varepsilon_2 < \varepsilon_2^T \quad (2)$$

$$|\varepsilon_{12}| < \varepsilon_{12}^S \quad (3)$$

where 1 and 2 are the longitudinal and transverse directions for the fibers and C refers to the ultimate strains in tension, compression and shear, respectively.

For matrix dominated failure, the following failure criterion, Equation 1, is widely used. This strength criterion accounts for stress interactions that can be important in matrix failure [7].

$$\left(\frac{\sigma_{22}}{S_{22}}\right)^2 + \left(\frac{\sigma_{33}}{S_{33}}\right)^2 + \left(\frac{\sigma_{23}}{S_{23}}\right)^2 < 1 \quad (4)$$

Where the left hand side of the equation is a function of $F(\sigma_{22},\sigma_{33},\sigma_{23})$. Failure occurs when the left hand side exceeds 1.0.

An extension of the von Mises criterion for orthotropic materials [6] can be expressed by an equation of the form

$$F(\sigma_{11},\sigma_{22},\sigma_{33},\sigma_{23},\sigma_{13},\sigma_{12}) < 1 \quad (5)$$

Tsi and Wu [8] expressed this as

$$F_1\sigma_1 + F_2\sigma_2 + F_{11}\sigma_1^2 + F_{22}\sigma_2^2 + F_{66}\sigma_{12}^2 - \sqrt{F_{11}F_{12}}\sigma_1\sigma_2 < 1 \quad (6)$$

Where

$$F_1 = \left(\frac{1}{\sigma_1^T} + \frac{1}{\sigma_1^C}\right) \quad (7)$$

$$F_2 = \left(\frac{1}{\sigma_2^T} + \frac{1}{\sigma_2^C}\right) \quad (8)$$

$$F_{66} = \left(\frac{1}{\sigma_{12}^F}\right) \quad (9)$$

$$F_{11} = -\left(\frac{1}{\sigma_1^T\sigma_1^C}\right) \quad (10)$$

$$F_{22} = -\left(\frac{1}{\sigma_2^T\sigma_2^C}\right) \quad (11)$$

This failure criterion works well for principal material tensile stresses, but is nonconservative for compression failures [7].

Note that in the failure criterion described above, all stresses must be transformed into the principal material directions of the composite using the equations below [8]. Strains also must be transformed into the principal material directions using similar transformation equations.

$$\sigma_{11} = \sigma_x \cos(\theta)^2 + \sigma_y \sin(\theta)^2 + \sigma_{xy} \sin(2\theta) \quad (12)$$

$$\sigma_{22} = \sigma_x \sin(\theta)^2 + \cos(\theta)\left(\sigma_y \cos(\theta) - 2\sigma_{xy} \sin(\theta)\right) \quad (13)$$

$$\sigma_{12} = \frac{1}{2}\left(-\sigma_x \sin(2\theta) + \sigma_y \sin(2\theta) + 2\sigma_{xy} \cos(2\theta)\right) \quad (14)$$

where σ_{11},σ_{22}, and σ_{12} are transformed stresses in the principal material directions and σ_x,

σ_y, and σ_{xy} are the applied stresses.

Fatigue

Fatigue is often one of the primary design drivers of wind turbine subtructures due to long operating lives. Fatigue life is usually expressed in cycles to failure, which is the number of repetitions of significant loads that can be sustained before cracks initiate and propagate to cause structural failure. Design lifetimes of a wind turbine blade include more cycles than those of the typical aircraft, bridge or helicopter, as shown in Figure 3 [1].

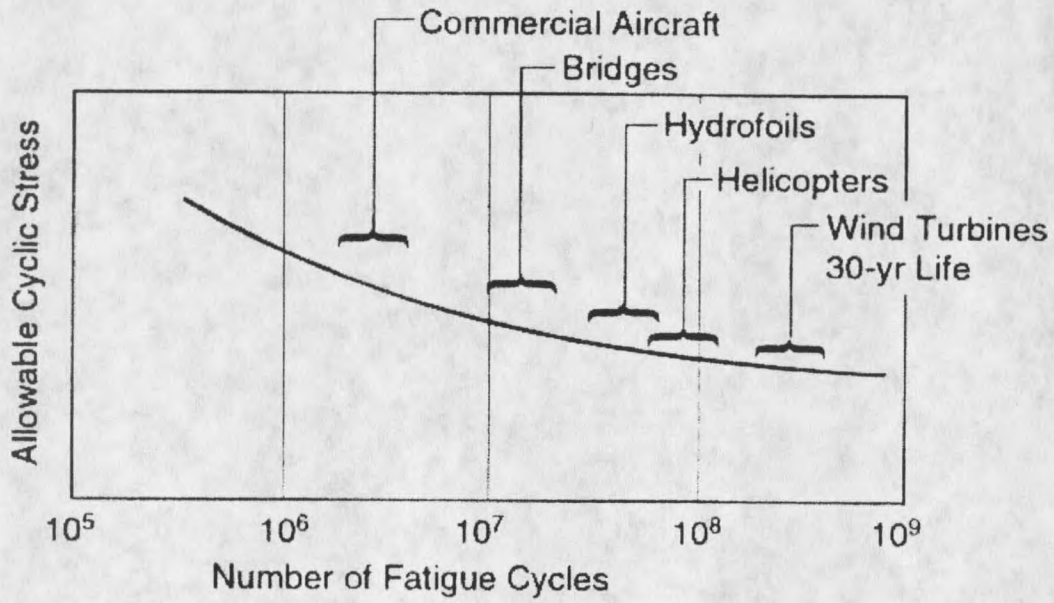


Figure 3. Typical S-N Curve for Various Fatigue Driven Designs [1]

Structures often experience loading that is applied and removed many times over the life of the structure. Uniform cyclic loading and unloading of a specimen over time is represented in Figure 4, where the relationships between the various stress parameters

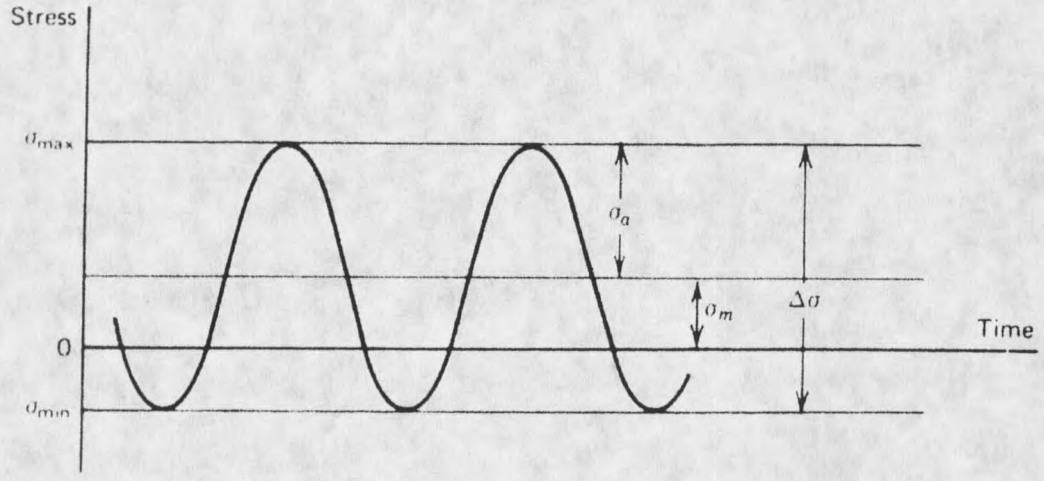


Figure 4. Uniform Cyclic Loading of a Specimen

(Equations 15, 16, 17) are:

$$\sigma_m = \sigma_{mean} = \frac{1}{2}(\sigma_{\max} + \sigma_{\min}) \tag{15}$$

$$\sigma_a = \sigma_{alt} = \frac{1}{2}(\sigma_{\max} - \sigma_{\min}) \tag{16}$$

$$R = \frac{\sigma_{\min}}{\sigma_{\max}} \tag{17}$$

Common values of the R ratio are 0.1 (tension/tension), 10 (compression/compression), and –1 for reverse loading (tension/compression).

Analysis of crack growth is essential in situations where a crack in a substructure may propagate to cause structural failure. The remaining life can be calculated in the context of fracture mechanics to determine whether the crack may be ignored, whether repair or replacement is needed immediately, or whether repair can be postponed until a more convenient time. Crack growth caused by cyclic loading is known as fatigue crack growth. The rate of growth with cycles can be characterized by the ratio $\Delta a/\Delta N$, or for

small intervals, by the derivative da/dN, where a is the crack length and N is cycles. The fatigue crack growth rate, da/dN, is the slope at a point on a crack versus cycle curves as shown in Figure 5.

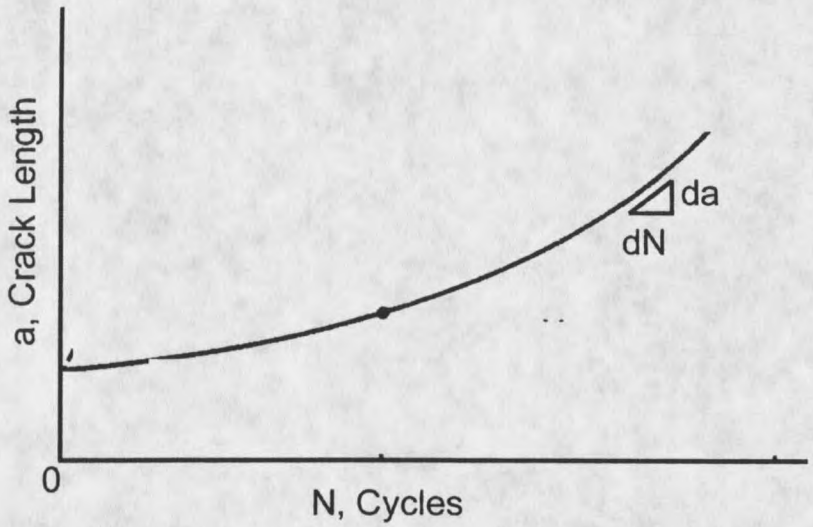


Figure 5. Fatigue Crack Growth Rate

Fracture Mechanics

Delaminations may develop during manufacture due to incomplete wetout or other factors. They may also result from high interlaminar stresses at or near free edges, matrix cracks, or other stress concentrations. These delaminations may then grow when the structure is subjected to cyclic loading. When a structure contains flaws, standard stress or strength based analysis may no longer accurately predict behavior, due to high stress gradients near flaws. Engineering fracture mechanics can provide the methodologies to compensate for the weaknesses of classical strength based analysis. All cracks and delaminations can be classified by three modes of growth as shown in Figure 6. Mode I consists of a crack face opening, mode II consists of shear loading, and mode

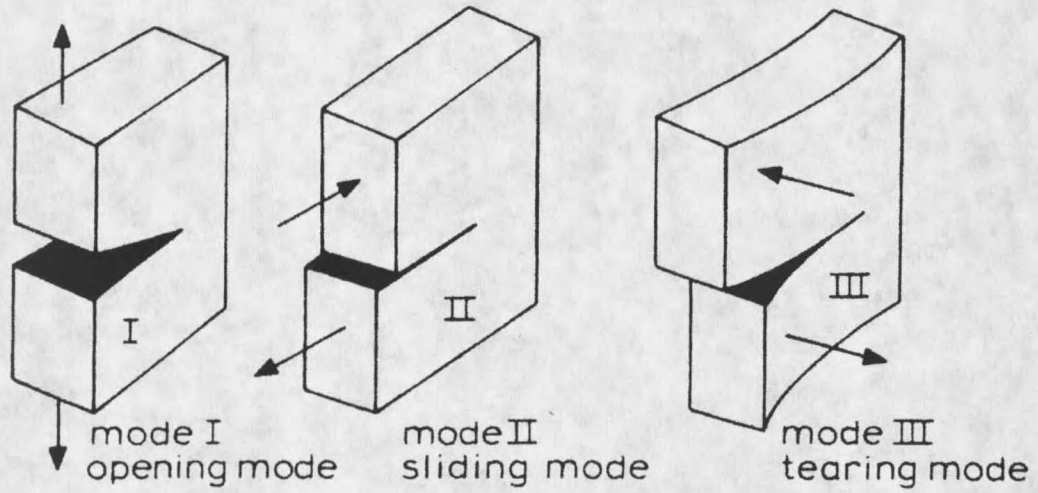


Figure 6. Fracture Modes: Three Modes of Fracture

III is tearing.

Griffith stated that "crack propagation will occur if the energy released upon crack growth is sufficient to provide all the energy that is required for crack growth" [9]. In order for a crack to propagate, the following condition must be met:

$$\frac{dU}{da} \geq \frac{dW}{da} \tag{18}$$

Where U is the elastic energy and W the energy required for crack growth. G, the strain energy release rate (SERR) or crack driving force, is equal to dU/da. The energy consumed in crack propagation is denoted by R = dW/da, which is called the crack resistance [9]. Thus, when G is greater than or equal to R, crack propagation will occur.

Mixed-Mode Fracture Criteria

Complex structures often have a mixed mode interaction at crack fronts. Once a database of fracture toughness has been established for Mode I and II, a mixed-mode fracture criteria must be established for use in the complex architectures. Russell and Street [10] suggest that it is of value to examine a database of Mode I and II toughness in terms of available empirical relationships for mixed-mode fracture toughness behavior. They proposed a form of

$$\left(\frac{K_I}{K_{Ic}}\right)^m + \left(\frac{K_{II}}{K_{IIc}}\right)^n = F \qquad (19)$$

for the I-II tension shear quadrant. The coefficients m and n are determined by curve-fitting and the K values are the stress intensity factors and c indicates the critical value for unstable crack growth. The K values are proportional to the square root of the G values [8].

Reeder [11] suggests that strain energy release is a good measure of a material's resistance to delamination growth and most of the failure criteria can be expressed in terms of a critical strain energy release rate or fracture toughness. This can be expressed in terms of fracture energies as

$$\left(\frac{G_I}{G_{Ic}}\right)^{m/2} + \left(\frac{G_{II}}{G_{IIc}}\right)^{n/2} = F \qquad (20)$$

where the coefficients m and n are determined by curve-fitting and the G values are the fracture energies. When the sum of the two terms (F) is greater than 1.0 crack growth

will occur.

Russell and Street [10, 12] found m = n = 2 for delamination data for unidirectional graphite/epoxy laminates. Wu found that m = 1 and n = 2 best represented the extensive database for splitting balsa wood and unidirectional S-glass/epoxy materials [12].

Crews and Reeder [13, 14, 15] developed the mixed-mode bending (MMB) test apparatus to investigate the mode interaction for laminated composites. The MMB test apparatus is a simple combination of mode I and mode II loading.

Russell and Street [12] point out that simple curve-fitting procedures fail to offer any insight into the mechanisms of failure, their usefulness is limited to interpolation over a specific fracture envelope for the material, geometry, and environment under consideration.

Numerical Methods to Predict Strain Energy Release Rates

This study used a direct method for numerically predicting G from finite element alnalysis: the Virtual Crack Closure Technique (VCCT).

Irwin postulated that if a crack extends from a to a + Δ, for infinitesimal values of Δ, the crack opening displacement behind the new crack tip will be approximately the same as those behind the original crack tip [16]. Then the work necessary to extend the crack from a to a + Δ is the same as that necessary to close the crack tip from a + Δ to a (Equation 21).

$$W = \frac{1}{2}\int_0^{\Delta} v(r)\sigma_y(\Delta - r)\,dr \qquad (21)$$

where v(r) is the crack opening displacement at a distance r behind the crack tip, a + Δ, σ_y is the normal stress distribution ahead of the crack, and Δ is the change in crack length, shown in Figure 7.

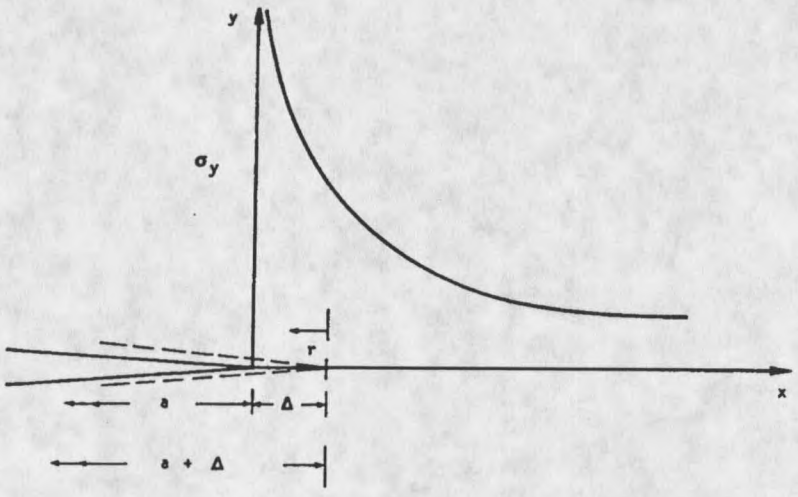


Figure 7. Normal Stress σ_y Distribution Ahead of the Crack Tip [17]

Irwin then calculated G using Equation 22 as

$$G = Lim_{\Delta \to 0}\frac{W}{\Delta} = Lim_{\Delta \to 0}\frac{1}{2\Delta}\int_0^{\Delta} v(r)\sigma_y(\Delta - r)\,dr \qquad (22)$$

where G is the amount of work required to close the crack an infinitesimal length Δ. Rybicki and Kanninen [16] then applied the Irwin Crack Closure Method to a 4-noded quadrilateral finite element, as

$$G_I = \frac{1}{2\Delta}[F_{y_i}\ (v_k - v_{k'})] \qquad (23)$$

$$G_{II} = \frac{1}{2\Delta}[F_{x_i}\ (u_k - u_{k'})] \qquad (24)$$

where: Δ is the width of the element, F is the force on node, u is the horizontal displacement of the node and v is the vertical displacement of the node and shown in Figure 8. This was the basic method used for the studies presented herein.

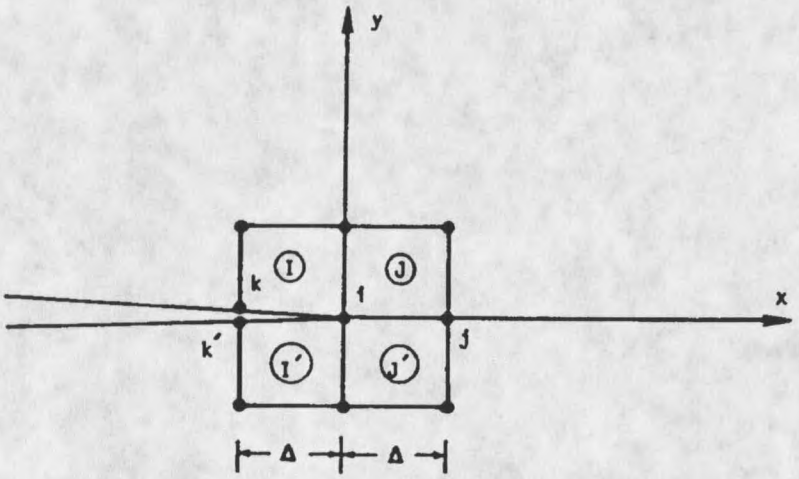


Figure 8. 4-Noded Quadrilateral Finite Element [17]

CHAPTER 3

EXPERIMENTAL METHODS

Resin and Fabric Systems

Fiberglass composites consist of a glass fabric reinforcing phase and a resin matrix binding agent. The majority of specimens used in this study were processed using CoRezyn 63-AX-051, an unsaturated ortho-polyester resin. Interplastic Corporation manufactured the resin. This resin, when combined with Lupersol DDM-9 methyl ethyl ketone peroxide (MEKP) at 1-2% by volume, yields a composite that is representative of those used in wind turbine blade components.

Vinyl Esters are also common in the manufacturing of composite wind turbine blades. Therefore, selected skin-stiffeners were also manufactured using two Vinyl Ester resins, Derakane 8084 (rubber modified) and Derakane 411C-50. Dow Chemical supplied the Vinyl Ester resin systems. Vinyl Esters were cured with 0.5% by volume Cobalt Naphthenate-6% (CoNap) promoted with 2% by volume Trigonox 239A catalyst. All polyester and Vinyl Ester samples were postcured at 60°C for a period of two hours. Molds and glass plates were coated with A1380 mold release to ease removal of Vinyl Ester samples.

The E-glass fabrics used in this study were manufactured by Owens-Corning Fabrics. All samples consisted of two architecturally different ply layers. The first fabric is D155 (areal dry weight of 526 g/m^2) which is a stitched unidirectional (90°) fabric. The second fabric is the DB120 (areal dry weight of 407 g/m^2) which is a double bias stitched ±45° fabric, as shown in Figure 9.

Manufacturing Equipment

The mold base for the DCB and ENF specimens, Figure 10, consisted of a 1.3 mm thick aluminum plate. A 12.7 mm x 12.7 mm groove was machined for the silicone gasket material. The mold base was topped with a 12.7mm thick tempered glass plate.

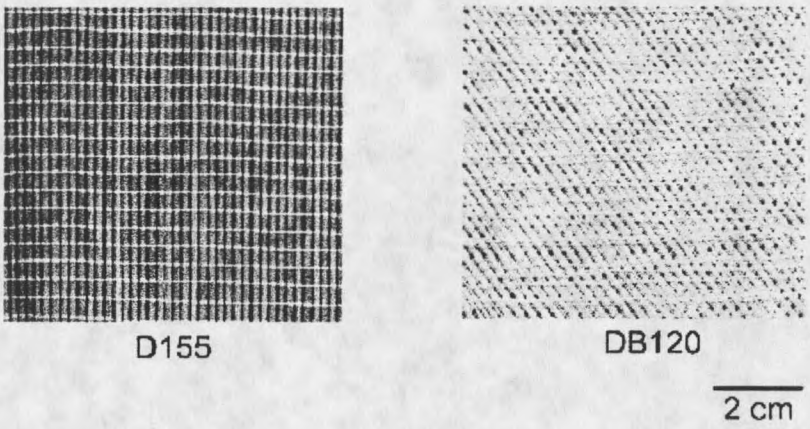


Figure 9. E-Glass Fabrics used in Test Specimens

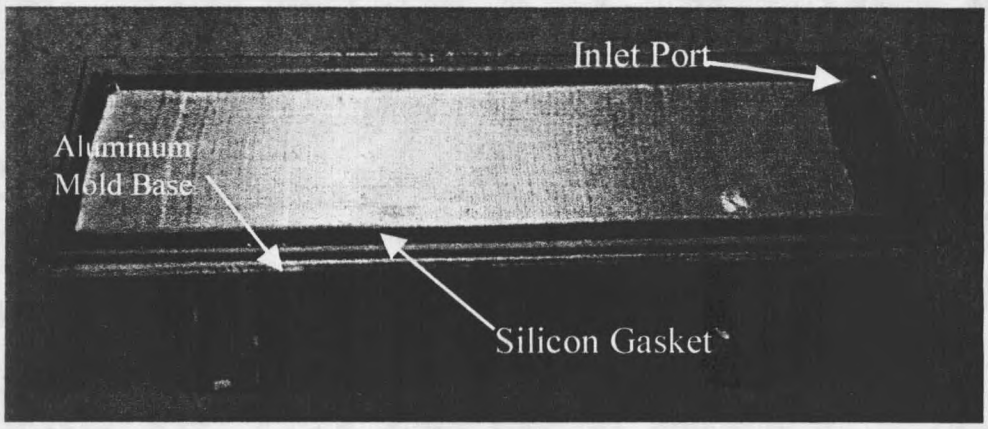


Figure 10. Flat Plate RTM Mold for DCB and ENF Specimens

The glass was secured to the mold base with 10 C-clamps.

A peristaltic pump was used for manufacturing all specimens used in this study, shown in Figure 11.

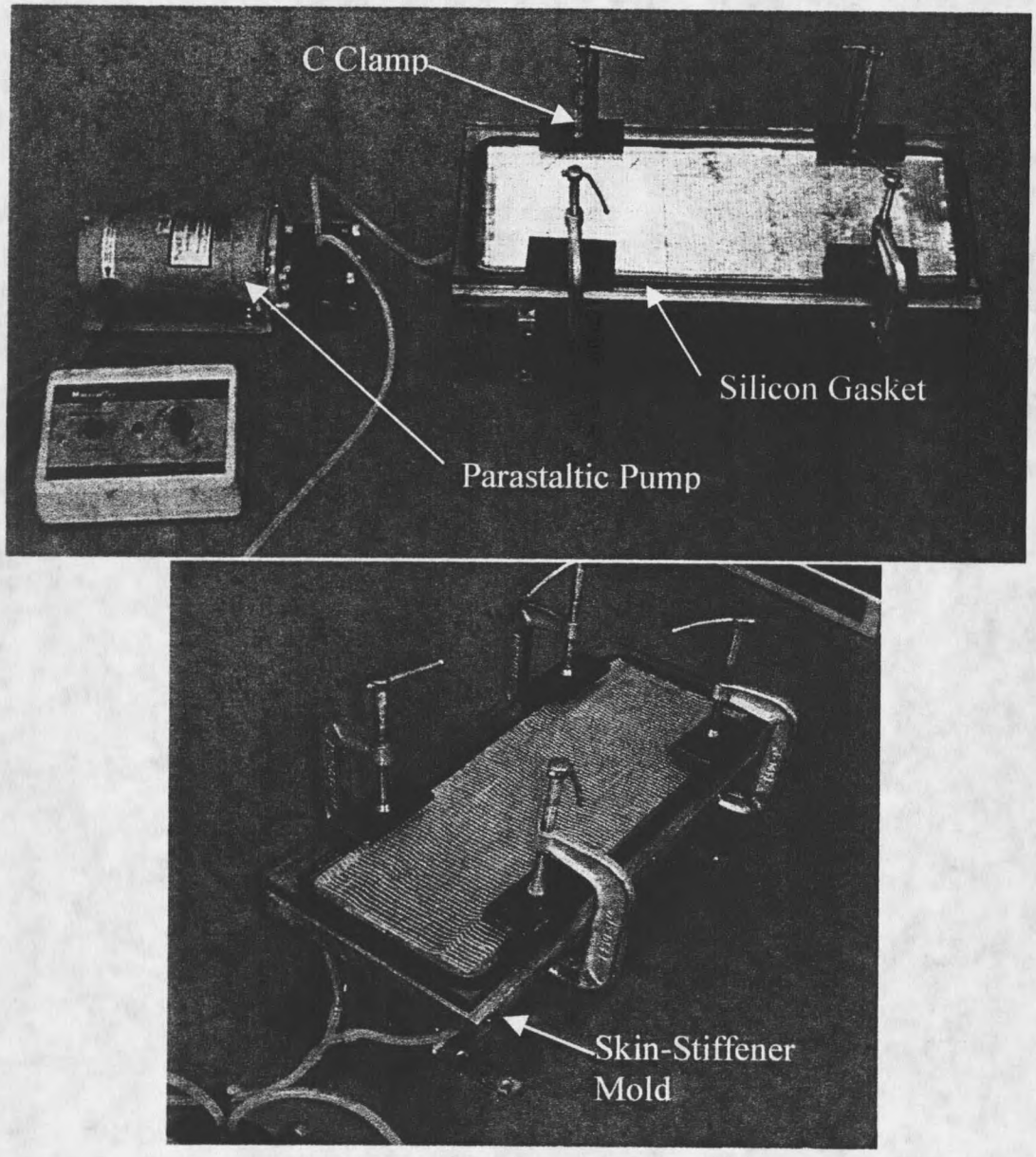


Figure 11. Peristaltic Pump and Skin-Stiffener Mold

The C Clamps were torqued such that the gap between the glass plate and aluminum mold base was 4.5 mm, which ensured that the skin and web thickness were each 4.5 mm.

Testing Machines

Two testing machines were used to perform the experimental tests. The static DCB specimens were tested using an Instron model 8562. This test machine is a servo electric driven machine with a 22480 N load cell, shown in Figure 12.

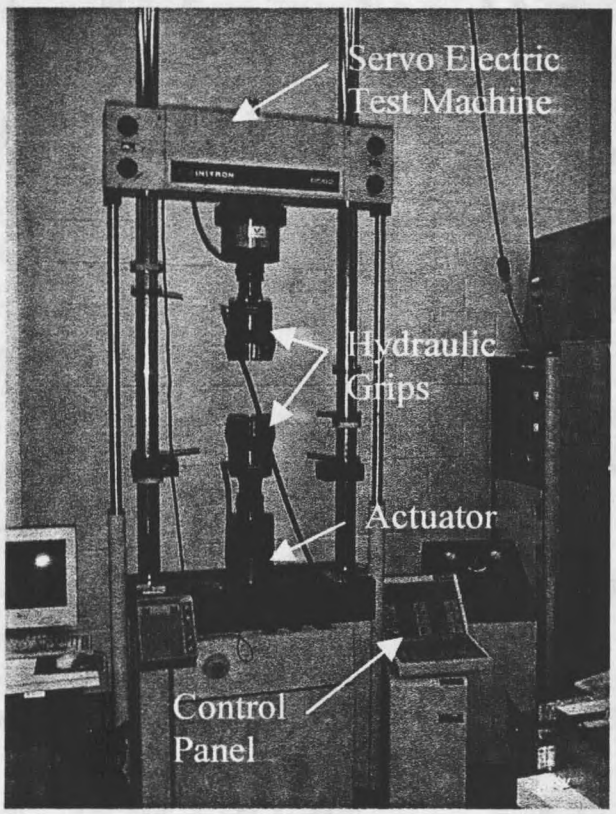


Figure 12. Servo Electric Test Machine with 445 N Load Cell

All of the remaining specimens were tested using an Instron Model 8511. This test machine is a servo hydraulic driven machine with a 4480 N load cell, shown in Figure 13.

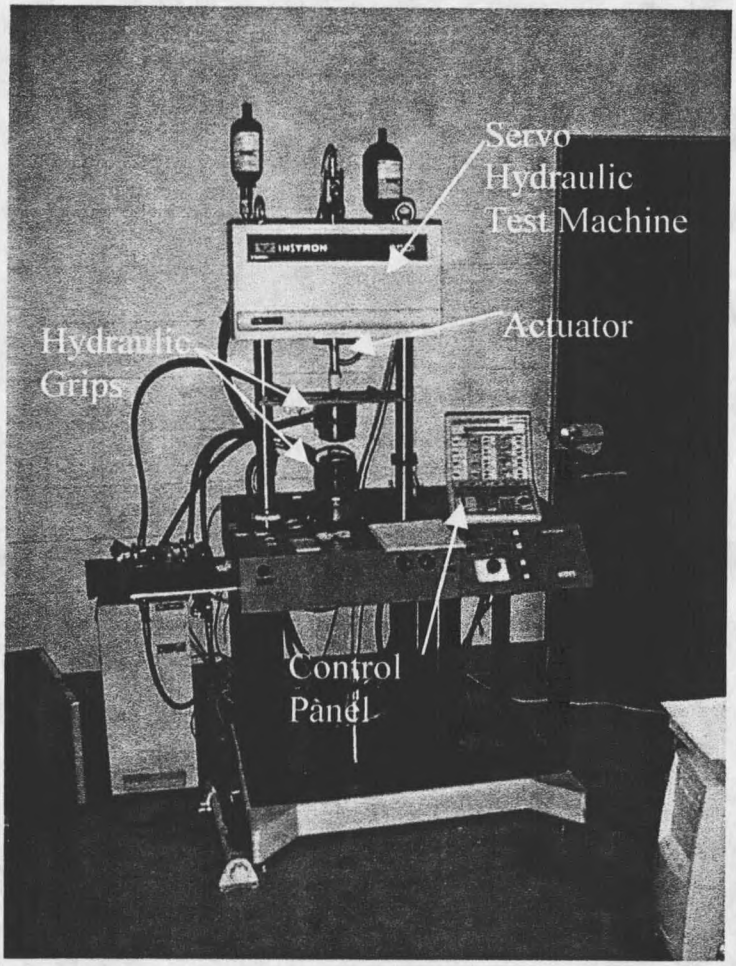


Figure 13. Servo Hydraulic Test Machine

DCB and ENF Specimens

Mode I interlaminar fracture toughness was obtained using the Double Cantilever Beam (DCB) test, see Figure 14.

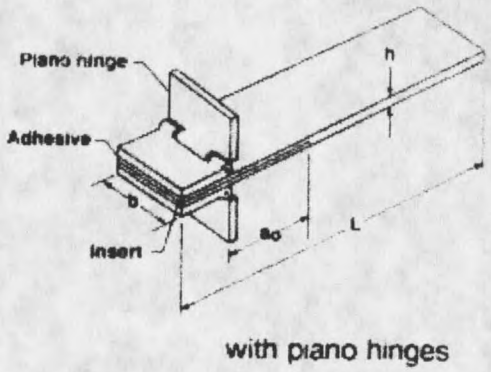


Figure 14. Double Cantilever Beam (DCB) Specimen

A teflon strip is positioned at the mid thickness between glass fiber layers during the manufacturing process to represent a flaw or crack. Loading hinges are bonded to the DCB specimens. The beam is loaded in displacement control using a tensile test machine until the crack front moves a measurable amount. The beam is then unloaded and final crack length is recorded. Load and displacement are continuously recorded during loading and unloading of the specimen. A typical load versus displacement plot is shown in Figure 15. ASTM has a detailed description of the DCB testing procedure and in depth analysis of several methods for calculating G values [18]. The detailed experimental testing procedures used in this thesis are discussed later in this chapter for further clarification and testing repeatability.

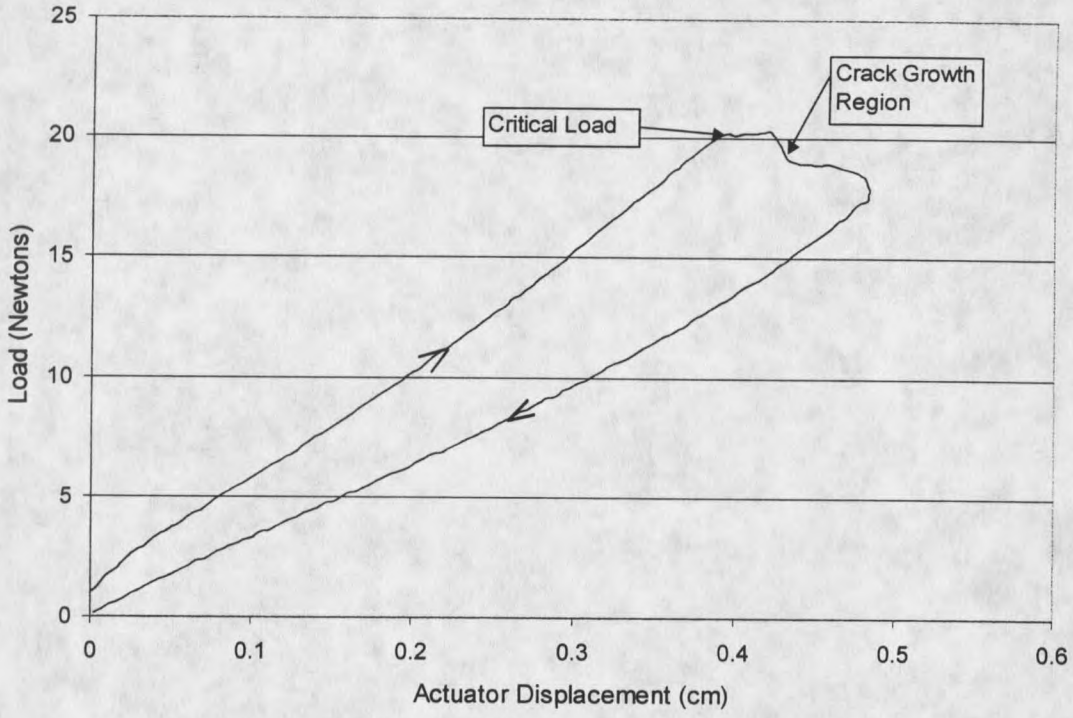


Figure 15. Typical Load versus Actuator Displacement Curve for DCB Specimen

Common methods of determining the G_{Ic} are the Modified Beam Theory (MBT) and the Area Method [18]. The MBT method is derived from elementary beam theory while the Area Method is a graphical approach. The Mode I strain energy release rate, G_{Ic}, using the MBT method (Equation 25) is:

$$G_I = \frac{3P_{cr}\delta_{cr}}{2ba} \tag{25}$$

where P_{cr} is the critical load, δ_{cr} is the critical displacement at the applied load location, b

is the specimen width, and a is the delamination length measured from the load application point (piano hinge) (Figure 14).

The area enclosed by the load versus displacement curve is the amount of energy, SERR, required to grow the crack some distance Δa. The G_{Ic}, from Equation 26 is thus calculated by:

$$G_{II} = \frac{Area}{b\Delta a} \tag{26}$$

where area is the area enclosed by loading-unloading loop (Figure 16), b is the width of the specimen and Δa is the change in crack length.

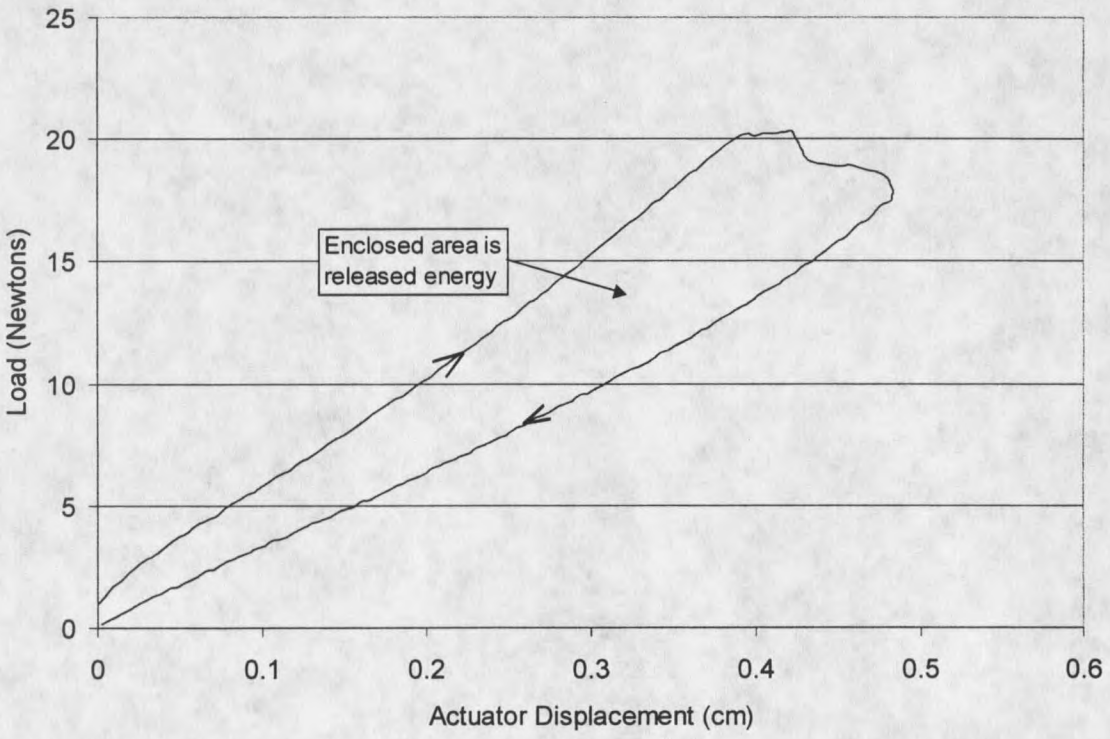


Figure 16. Area Enclosed by Loading-Unloading Loop

Mode 2 interlaminar fracture toughness is determined by the End Notch Flexure Test (ENF) as shown in Figure 17. Russell and Street [19] originally developed the

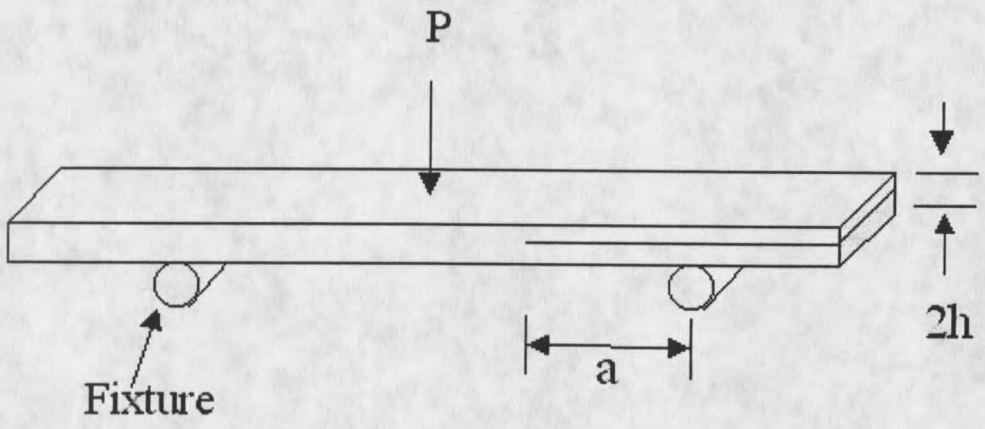


Figure 17. Mode II Fracture Specimen Geometry

testing procedure. The teflon strip is positioned between the glass fiber laminates in the composite during the manufacturing process. The beam is placed in a three point loading fixture. The specimen is loaded at the midspan until the crack front moves some measurable amount, Δa. The beam is then unloaded. A typical load versus displacement plot is shown in Figure 18.

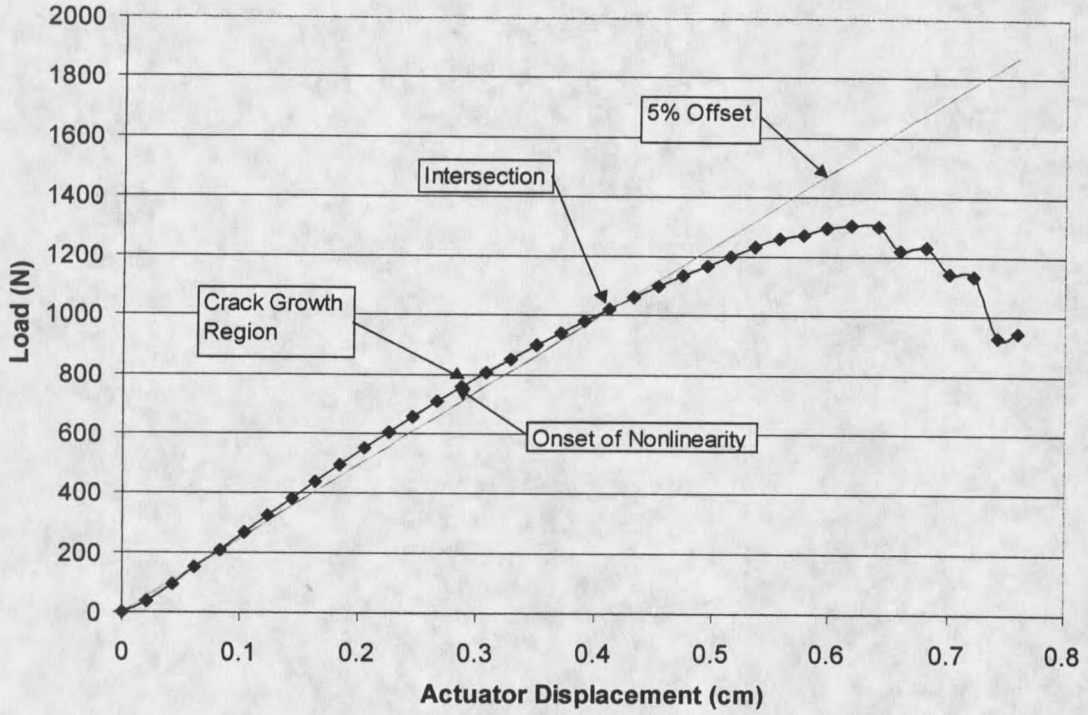


Figure 18. Typical Load versus Actuator Displacement Curve for an ENF Specimen

A closed form equation for G_{IIc} associated with delamination growth by Russel and Street [19] yields Equation 27

$$G_{II} = \frac{9P^2a^2}{16b^2Eh^3} \tag{27}$$

where P is the applied load for crack growth, a is the initial crack length in specimen, b is the specimen width, h is the half height of composite beam, and E is the flexural modulus. The load taken for the calculation is the intersection of the load-displacement curve with the 5% tangent line shown in Figure 18.

Fatigue testing of DCB and ENF specimens is a common method of characterizing crack growth rates for specific composite architectures. A procedure [20, 21] for obtaining delamination growth rates is described as follows. The following values are recorded at specified intervals: a, the crack length, N, the number of load cycles, and δ, the actuator displacement. An empirical relation is then determined for change in crack length per cycle, da/dN. Once a crack length to number of cycles relationship has been obtained, the SERR and delamination growth rate can be determined using the methods described earlier in the chapter. A typical log-log relationship between da/dN and ΔG is shown in Figure 19, where ΔG is the range of G between the maximum and minimum loads.

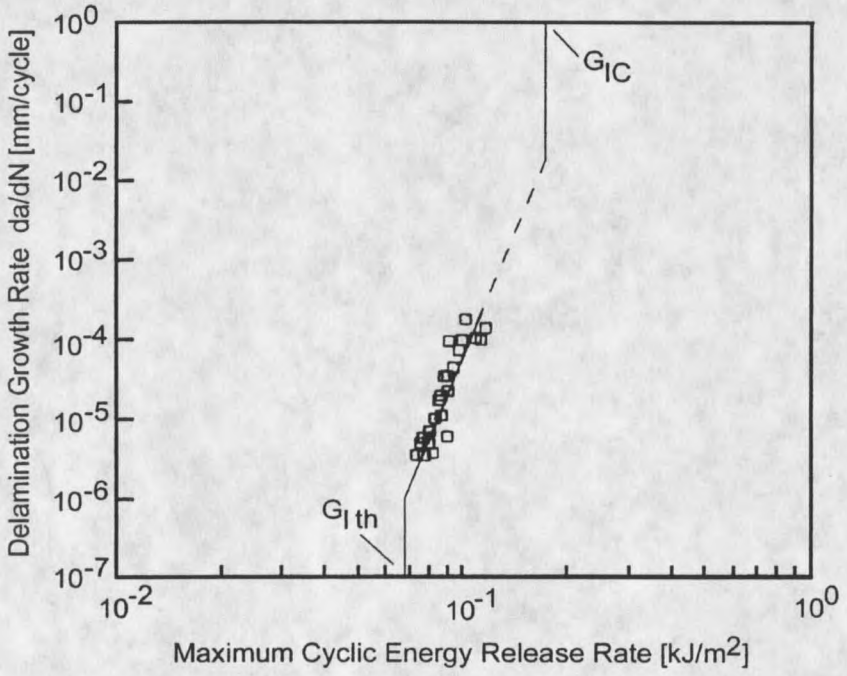


Figure 19. Typical Log-log Relationship between da/dN and ΔG

From the da/dN versus ΔG curve, a power law relationship (Equation 28), known as Paris Law [20], can be defined using a standard curve fitting computer package.

$$\frac{da}{dN} = A G^n \qquad (28)$$

where da/dN is the delamination growth rate, A is a material parameter, n is a material parameter and G is the strain energy release rate at the maximum load in the fatigue cycle. The range of G in the cycle, ΔG, is more commonly used for metals [22].

The two specimen configurations were investigated to determine static and fatigue G values for Mode I and II, shown in Table 1.

Series ID	Specimen Type	Layup	Crack Interface	Number of Tests	Motivation
6XX	DCB	$[(45),(90)_2,(45)]_4$	(45°/45°)	14	static G_I test
6XX	DCB	$[(45),(90)_2,(45)]_4$	(45°/45°)	8	fatigue G_I test
7XX	DCB	$[(45)_9,(90),(45)_8]$	(90°/45°)	18	static G_I test
7XX	DCB	$[(45)_9,(90),(45)_8]$	(90°/45°)	8	fatigue G_I test
8XX	ENF	$[(45)_9,(90),(45)_8]$	(90°/45°)	3	static G_{II} test
7XX-8XX	ENF	$[(45)_9,(90),(45)_8]$	(90°/45°)	14	fatigue G_{II} test

Table 1. Table of DCB and ENF Series ID and Motivation

The DCB and ENF specimens were prepared using the flat plate mold and inserting teflon release film at the center of the fabric lay-up to form an initiation crack. Both types of specimens were cut into 2.54 cm widths using a diamond bit wet cut table saw. DCB specimens were sanded with 100-grit sandpaper where the loading hinges were mounted to remove any release agent from the manufacturing process. Loading

hinges were adhered to the samples using a two-part epoxy, Hysol EA9302.2NA. The edges of the specimens were wet sanded and polished with 400 grit sandpaper so crack fronts could easily be identified and measured.

Several methods of crack length monitoring were investigated. Two electrical resistance methods were attempted using copper tape and silver colloidal paint. Visual inspection with a scaled loupe microscope, shown in Figure 20, was used in parallel with tape and paint techniques to ensure accurate crack front readings. The copper tape was obtained from 3M, Electrical Tape Division, Part # 3224-1. The silver colloidal paint was obtained from Ted Pella, Inc., Catalog # 16031. The conductive materials were adhered to the surface of the crack specimen, shown in Figure 21. A voltage was applied to a three-quarter wheatstone bridge. The DCB with the conductive material served as the fourth resistor to complete the bridge circuit.

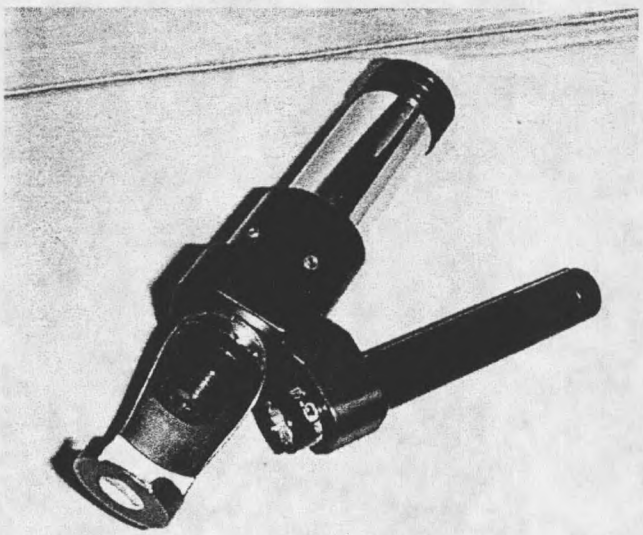


Figure 20. Scaled Loupe Used to Monitor Crack Fronts

The voltage across the DCB could then potentially be measured during the test operation. A function could then have been obtained for crack length as a function of voltage. The copper tape and silver colloidal paint monitoring systems functioned with little or no success as a consequence of coating variability. Thus, subsequent tests consisted of visual inspection only.

In order determine a valid value for G_{Ic}, the specimens were precracked a small distance (2-3 mm) to eliminate erroneous results due to a resin rich region at the tip of the starter film. Tests were performed by loading and unloading the specimens so that a complete load history could be recorded for future reference. All crack growth was monitored within a 0.1 mm using a scaled loupe microscope. Crack fronts were generally uniform across the width of the beam.

DCB Static Test Procedure

1. Specimens were precracked with a small flat screwdriver, past the teflon strip, so the resin rich region would not influence G values.
2. Initial crack length was recorded using the scaled loupe to the nearest 0.1 mm.
3. Specimens were loaded using hinges mounted to aluminum straps placed in Instron grips, shown in Figure 21.
4. Specimens were loaded in displacement control at a rate of 0.254 mm/sec.
5. The critical load, used in the MBT equation, was determined as the point at which non-linearity occurred in the load-displacement curve and a drop in load occurred. This corresponded to an increase in compliance of the DCB specimen.

6. After onset of non-linearity, the specimen was then unloaded at a rate of 0.254 mm/sec to zero load.
7. Final crack length was recorded using the scaled loupe.
8. Subsequent values for G_{Ic} were then calculated using MBT (Equation 25). P_{cr} and δ_{cr} were entered into the MBT equation. The area enclosed by the load-displacement hystersis loop was numerically integrated using EasyPlot. This area divided by the projected area of crack growth is the strain energy release of the system during crack growth.

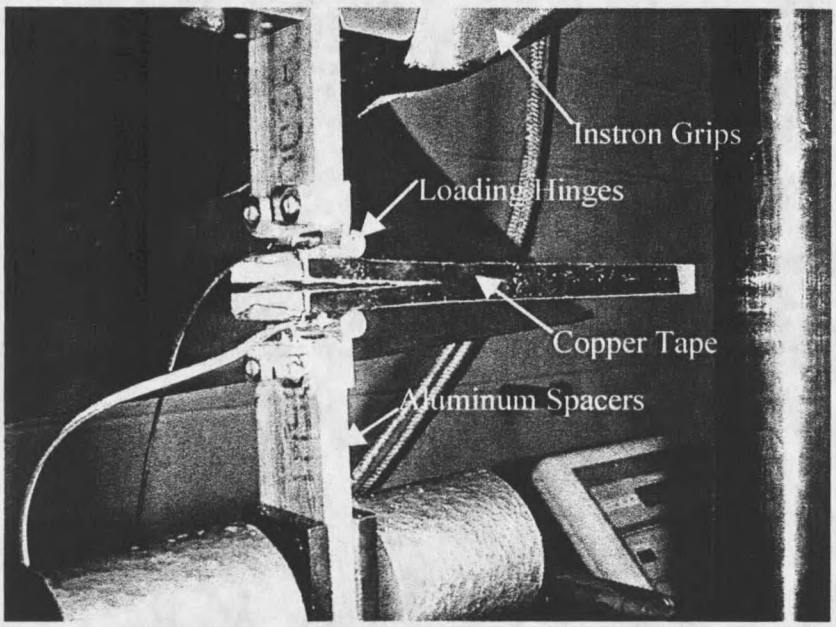


Figure 21. DCB Test with Conductive Copper Tape

DCB Fatigue Test Procedure

1. The specimen was precracked using a small screwdriver.
2. The initial crack length was recorded using scaled loupe.

3. The specimen was loaded using hinges mounted to aluminum straps placed in Instron grips shown in Figure 21.
4. The specimen was loaded to the average load in load control.
5. A load control sinusoidal waveform that produced an R-value of 0.1 was applied to the specimen at a frequency of 4-6 Hz. The adaptive control feature from the Instron control panel was set. This ensured that a constant load was applied to the specimen as the compliance increased when the crack front advanced.
6. The maximum displacement limits were set such that the DCB crack front could advance between 1 and 5 mm.
7. Once the displacement limit was tripped, final crack length, maximum cyclic load, number of loading cycles, and initial and final displacements were recorded. A Labview program was written to record cyclic data at specified intervals. Cyclic load data was typically recorded every 40 –60 cycles. This reduced the amount of computer CPU and disk space required for archival and handling of test data files. A copy of the Labview program used for DCB testing performed in this thesis is given in Appendix E.
8. Reduced data for da/dN and G_{Ic} (Equations 28 and 26), using the Power Law and MBT relationships, were determined as discussed earlier.

Static ENF Test Procedure

1. The specimens were precracked (as described previously).
2. The initial crack length was recorded using the scaled loupe.

3. The specimen was loaded in displacement control at a rate of 0.254 mm/sec.
4. The critical load was determined to be the point at which non-linearity occurred in the load-displacement curve or a drop in load occurred (Figure 18). At the point of non-linearity, the crack usually grew quickly in an unstable fashion. An ENF test in progress is shown in Figure 22.
5. The critical load and displacement values were inserted into Equation 27 for the determination of G_{IIc}.

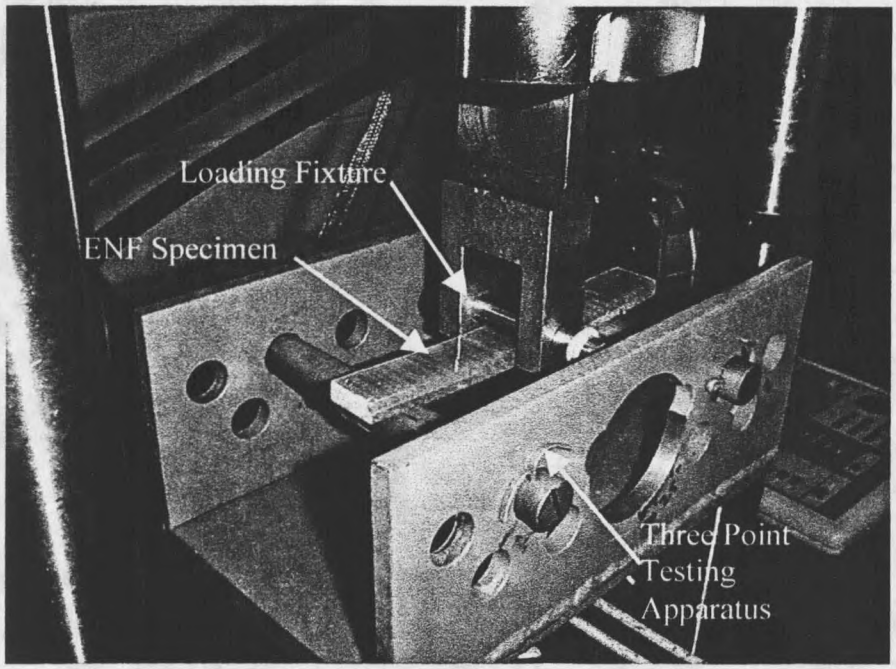


Figure 22. ENF Test in Progress

ENF Fatigue Test Procedure

1. The specimen was precracked.
2. The initial crack length was recorded using scaled loupe.

3. The specimen was loaded to the average compressive load in load control.
4. A sinusoidal waveform, in load control, that produced an R-value of 0.1 was applied to the specimen at a frequency of 4-6 Hz. The adaptive control feature from the Instron control panel was set.
5. The maximum displacement limits were set.
6. Once the displacement limit was tripped, final crack length, maximum load, number of loading cycles, and initial and final tip displacements were recorded. A Labview program was written to record cyclic data at specified intervals. Cyclic load data was typically recorded every 40–60 cycles. This reduced the amount of computer CPU and disk space required for archival and handling of test data files. A copy of the Labview program used for ENF testing is given in Appendix E.
7. Reduced data for da/dN (Equation 28) and G_{IIc}, using the Russel and Street Equation (Equation 27), were determined as discussed earlier.

Substructure Specimens

The skin-stiffener tests were performed to investigate the mechanisms and mode of fracture for intersection detail regions. The skin-stiffener, shown in Figure 23, was chosen for its relatively simple geometry and ease of manufacturing. These tests provided data for substructure modeling validation with the Ansys finite element code.

A variety of resin systems were used in the skin-stiffeners. A summary of the stiffener test matrix and motivations is presented in Table 2. The edges of the skin-stiffeners were polished to enhance the detectability of damage and crack growth within

the specimens. Load, displacement, bending strain and damage were monitored on all tests.

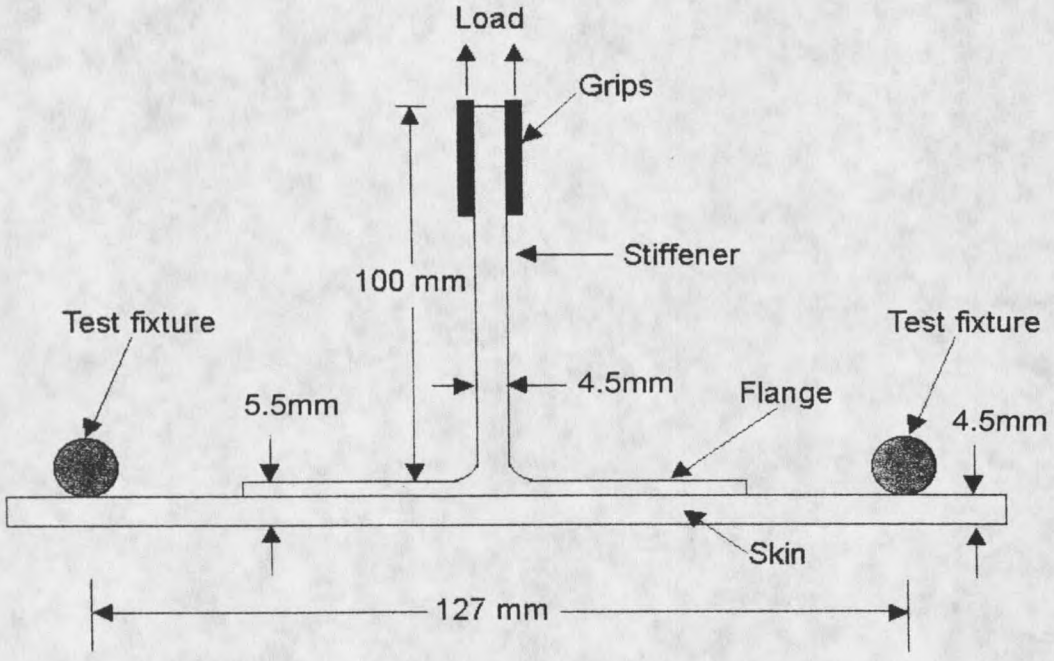


Figure 23. Skin-Stiffener Loading , Geometry and Dimensions

Two load cases were investigated. They were initial static tensile pull-off tests and cyclic tensile tests. These tests were performed with the simply supported testing apparatus shown in Figure 24. The load for both cases was applied to the specimen by gripping the upper 2.5 cm of the web in the hydraulic grips of the Instron and the

reacting load with the bars of the test fixture.

Series ID	Resin	Layup		Number of Tests	Motivation
		Web	Skin		
8TXX-10TXX	Ortho-polyester	$[(45),(90)_2,(45)]_s$	$[(45),(90)_2,(45)]_s$	3	static test – initial damage & maximum load
8TXX-10TXX	Ortho-polyester	$[(45),(90)_2,(45)]_s$	$[(45),(90)_2,(45)]_s$	17	fatigue test
18TXX	Ortho-polyester	$[(45),(90)_2,(45)]_s$	$[(45),(90)_2,(45)]_s$	6	static crack growth investigation
11TXX	8084 Vinyl Ester	$[(45),(90)_2,(45)]_s$	$[(45),(90)_2,(45)]_s$	3	static test – initial damage & maximum load
11TXX	8084 Vinyl Ester	$[(45),(90)_2,(45)]_s$	$[(45),(90)_2,(45)]_s$	8	fatigue test
14TXX	Iso-polyester	$[(45),(90)_2,(45)]_s$	$[(45),(90)_2,(45)]_s$	3	static test – initial damage & maximum load
14TXX	Iso-polyester	$[(45),(90)_2,(45)]_s$	$[(45),(90)_2,(45)]_s$	8	fatigue test
16TXX	411 Vinyester	$[(45),(90)_2,(45)]_s$	$[(45),(90)_2,(45)]_s$	3	static test – initial damage & maximum load
16TXX	411 Vinyl Ester	$[(45),(90)_2,(45)]_s$	$[(45),(90)_2,(45)]_s$	9	static & fatigue test

Table 2. Summary of Skin-Stiffener Test Matrix

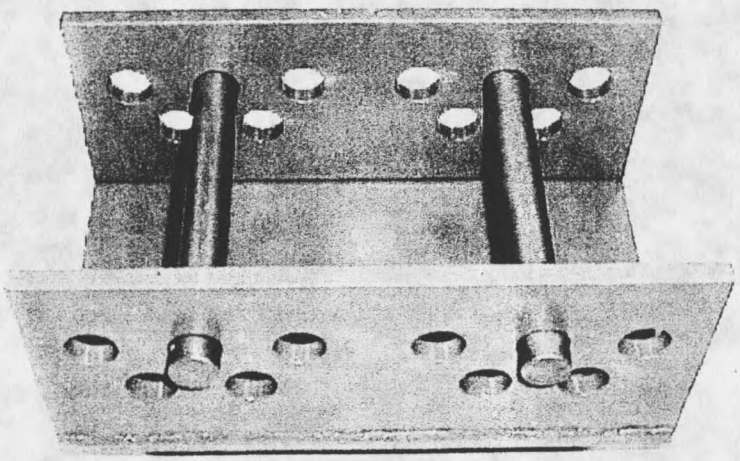


Figure 24. Test Apparatus used for ENF and Skin-Stiffener Specimens

During the cyclic fatigue loading experiments, the skin-stiffener was inserted between the reaction bars and secondary reaction bars with rubber bands to constrain downward movement of the skin shown in Figure 25.

This was a safety precaution to ensure that complete unloading of the specimen and unconstrained downward translation did not occur, resulting in impact of specimen to the lower plate of the testing apparatus.

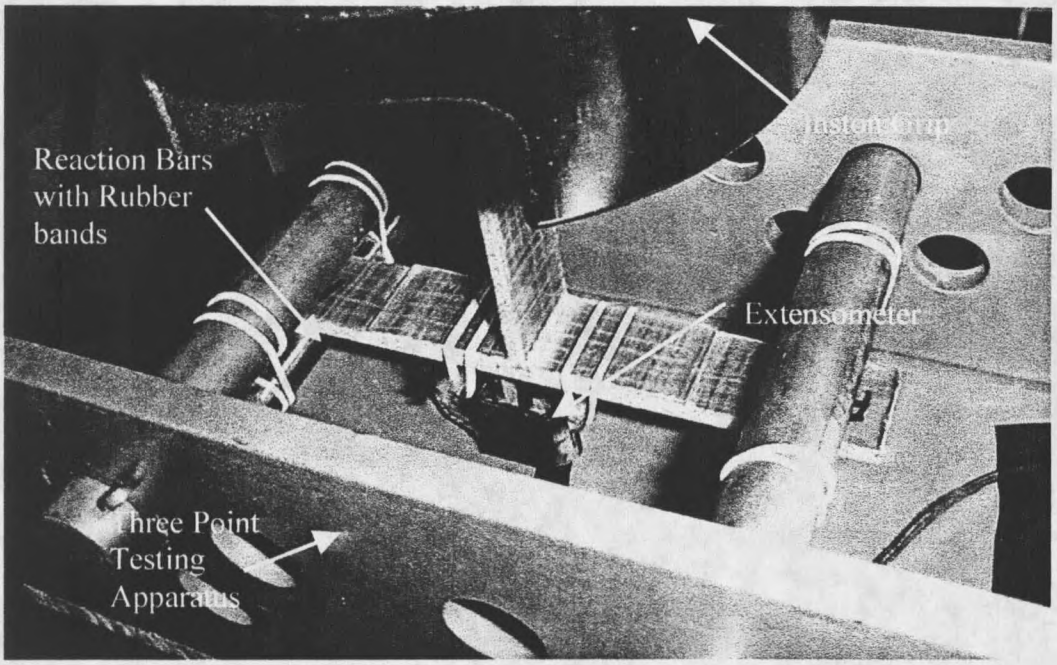


Figure 25. Typical Skin-Stiffener Tensile Test

Static Test Procedure

1. Specimens were loaded in displacement control at a rate of 0.254 mm/sec.
2. Data were collected for load, actuator displacement and skin bending strain. A typical load versus displacement curve is shown in Figure 26.

3. Initial damage onset was taken as the point where the load-displacement curve became non-linear. This correlated well with an audible "pop", where crack initiation occurred at the radius between the web and flange.

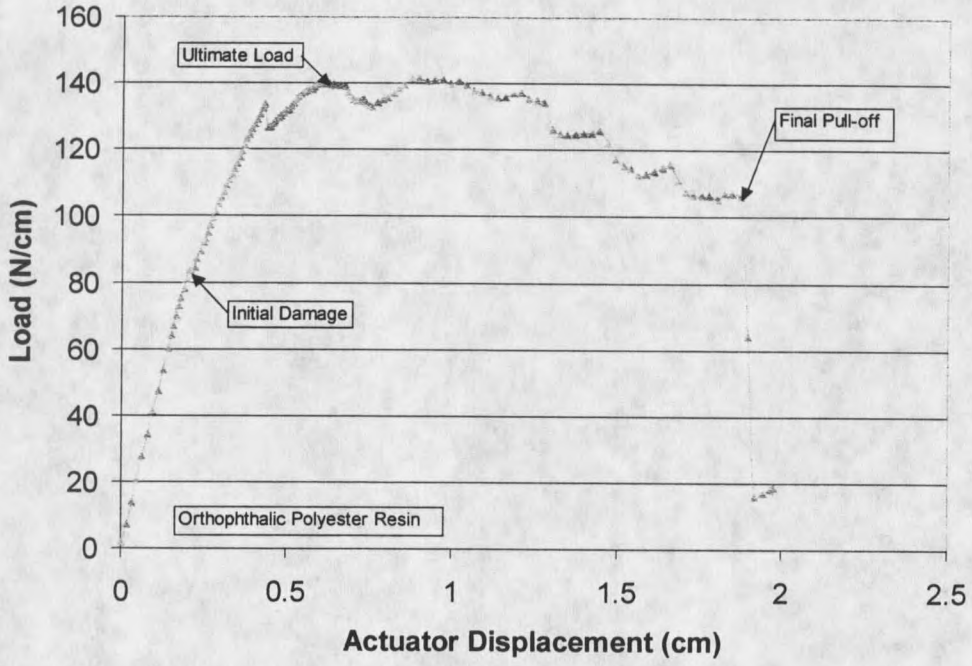


Figure 26. Typical Static Tensile Load Versus Displacement Curve for Skin-Stiffener Pull-Off Testing

Fatigue Test Procedure

1. Specimens were loaded to the mean load in load control.
2. A sinusoidal waveform that produced an R-value of 0.1 was applied to the specimen at a frequency of 2-4 Hz.

3. The maximum and minimum per cycle data was collected for load, actuator displacement, and skin bending strain. The Labview program recorded cyclic data at specified intervals. Cyclic data was typically recorded every 40 –60 cycles.
4. The maximum displacement limits were set at 0.635mm intervals.
5. Once the displacement limit was tripped, damage locations and crack lengths were recorded with a scaled loupe microscope.
6. Steps 1 through 5 are repeated until a change in maximum displacement of 5.08mm occurred. This change in displacement correlates to static initial damage onset for ortho-polyester skin-stiffener specimens.

CHAPTER 4

NUMERICAL METHODS

DCB specimens were modeled by finite element analysis (FEA) to validate the analysis against the established MBT formula (Equation 25). The FEA procedure was then used to determine G_I and G_{II} values for the skin-stiffener specimen. Ansys finite element DCB models for the double cantilever beam (DCB) specimen were constructed using 2-D (plane strain) and 3-D continuum elements. The 2-D model was employed for skin-stiffener geometry [23].

DCB Models

The DCB was initially modeled using 3-D continuum elements (solid 45) in Ansys 5.5. A 3-D analysis was performed to investigate edge effects during crack growth. Half symmetry about the longitudinal mid-plane of the DCB was used to simplify the model by restricting the nodes along the mid-plane to have zero horizontal (z)-displacement. The lower beam tip was constrained in the vertical (y) and longitudinal (x) directions as shown in Figure 27. The lower beam tip was constrained in the (x) and (z) directions to simulate hinge load points. The experimental load was halved and applied to the upper beam tip in the vertical (y) direction.

A 2-D DCB model was then constructed using 2-D (plane strain) continuum elements (plane 82). The lower beam tip was constrained in the horizontal (x) and vertical (y) directions as shown in Figure 28. The lower beam tip was constrained in the (x) direction to simulate the hinge load point. A vertical normalized load per unit width was applied to the upper beam tip.

A mesh sensitivity study performed by Haugen suggests that the ratio of total crack length to element width (a/da ratio) must be greater than 25 [5]. He reported that instability occurs for (a/da) ratios of less than 25 and invalid G results occur. Thus, in the localized region of all the crack front models, element size was minimized to obtain an (a/da) ratio greater than 25.

The models were constructed using individual lamina rather than smeared properties. This method requires more processing and CPU time, but is generally more accurate.

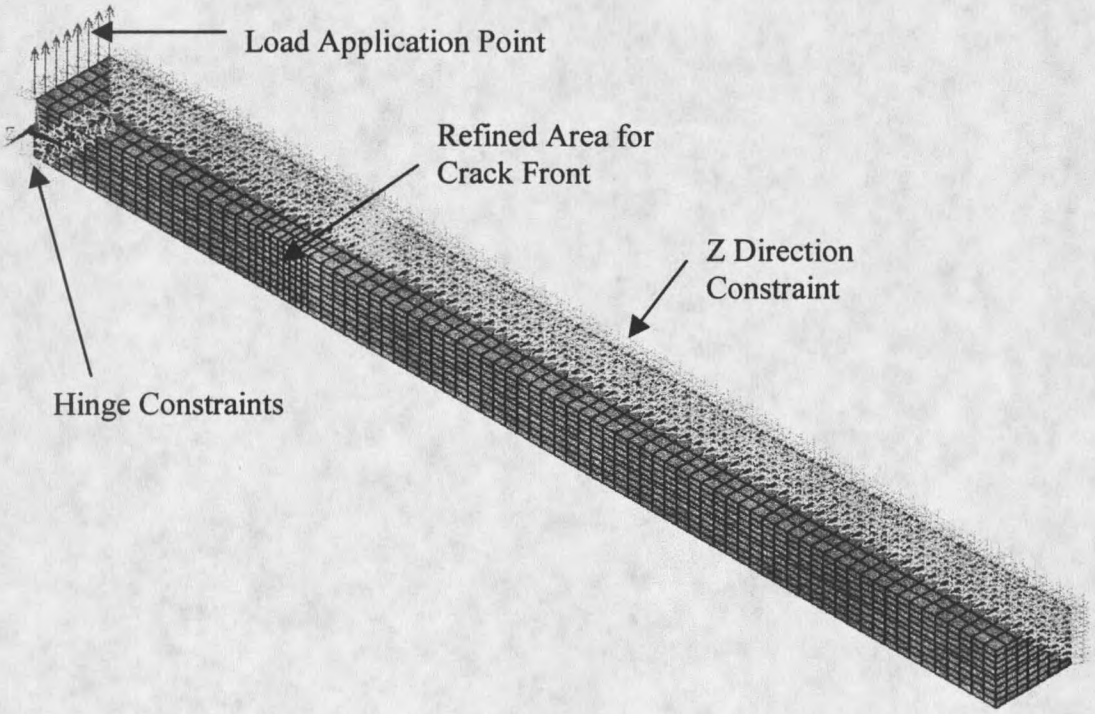


Figure 27. 3-D DCB Model with Applied Loads and Constraints

Individual lamina layer properties, nine independent properties for orthotropic materials, were entered into Ansys as separate material sets. The models are then constructed with a series of areas for 2-D analysis or volumes for 3-D analysis. The material set was set active for each area or volume being meshed. All models were constructed and analyzed with the use of batch files. The use of batch files reduces interaction time between the

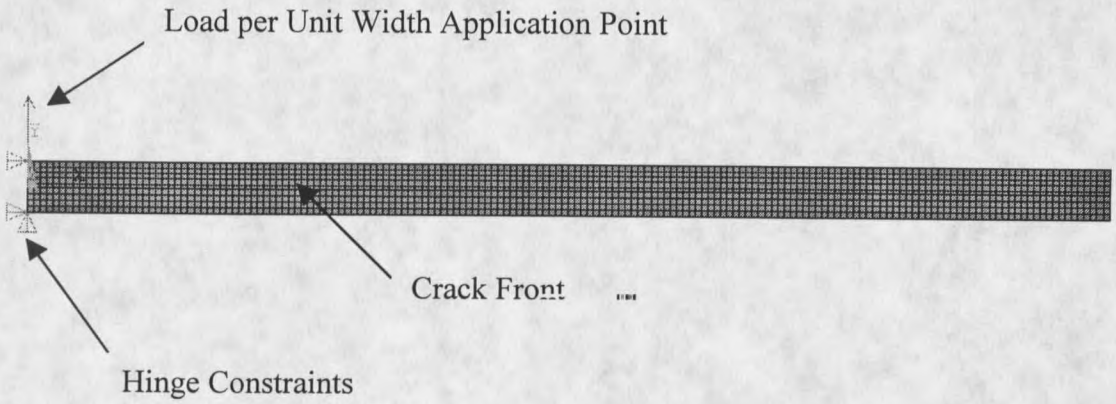


Figure 28. 2-D DCB Model with Applied Loads and Constraints

Ansys Graphic User Interface (GUI) and the user. Batch files can be easily modified to perform parametric studies on material properties, boundary conditions, loading cases, etc. A sample batch file is enclosed in Appendix D. Additional input lines can be added to reduce post-processing time if specific output is desired, thus reducing additional interaction with the Ansys GUI post-processor.

The material properties for the polyester E-glass plies were obtained from the MSU database published by Mandell and Samborsky [3]. Typical material properties for DB120 and D155 fabric layers are shown in Tables 3 and 4.

Static Longitudinal, Transverse and Simulated Shear Properties for E - Glass fabrics used in the MSU RTM composites															
			Longitudional Direction									Transverse Direction			
			Elastic Constants				Tension		Compression		Shear	Tension		Compression	
Fabric	layup	V_F %	E_L GPa	E_T GPa	υ_{LT}	G_{LT} GPa	UTS_L MPa	ϵ_U %	UCS_L MPa	ϵ_U %	τ_{TU} MPa	UTS_T MPa	ϵ_U %	UCS_T MPa	ϵ_U %
A130	$[0]_8$	45	36.3	8.76	0.32	3.48	868	2.53	-334	-0.92	87.1	33.8	0.39	-93.3	-1.05
D092	$[0]_{10}$	45	35.3	8.76	0.31	4.15	952	2.98	-773	-2.19	142	38.5	0.44	-133	-1.52
D155	$[0]_6$	45	37.0	8.99	0.31	4.10	986	2.83	-746	-2.02	94.2	27.2	0.30	-129	-1.67
DB120*	$[0]_{16}$	44	26.5	7.52	0.39	4.12	610	2.49	-551	-2.08	84.9	24.9	0.33	-90.8	-1.21
DB240*	$[0]_8$	46	31.0	7.38	0.35	3.74	697	2.64	-538	-1.74	68.7	19.7	0.27	-122	-1.69
0/90ROV*	$[0/90]_7$	46	23.9	23.9	0.26	4.08	382	2.27	-223	-0.93	99.9	382	2.27	-223	-0.93

Notes: E_L - Longitudional modulus, υ_{LT} - Poisson's ratio, G_{LT} and τ_{TU} - Shear modulus and ultimate shear stress from a simulated shear (±45) ASTM D 3518 test. UTS_L - Ultimate longitudional tensile strength, ϵ_U - Ultimate tensile strain, UCS_L - Ultimate longitudional compressive strength, ϵ_U - Ultimate compressive strain.
Coupons had a 100 mm gage length and tested with a 0.02 mm/s testing velocity. * DB120 and DB240 fabrics were separated into a +45 and a -45 orientation and then rotated to 0 degrees to form a unidirectional material. The 0/90 ROV material was tested as a 0/90 fabric.

Table 3. Static Longitudinal, Transverse and Simulated Shear Properties for D155 and DB120 Unidirectional Materials

Physical Elastic Constants of Material D155, V_F = 36%			
Property and test plane	Test Values	Average	s.d.
E_L,(LT plane),GPa	28.1, 27.0, 29.8	28.3	1.4
E_L, (LZ plane), GPa	28.0, 28.3, 27.6	28.0	0.4
E_T, (TZ plane), GPa	8.00, 7.31, 7.93	7.75	0.38
E_Z, (ZX plane), GPa	7.10, 7.65, 7.38	7.38	0.28
υ_{LT}	0.329, 0.320, 0.301	0.32	0.01
υ_{LZ}	0.305, 0.338, 0.331	0.33	0.02
υ_{TZ}	0.466, 0.395, 0.449	0.44	0.04
G_{LT}, GPa	3.31, 3.35, 3.23	3.30	0.06
G_{LZ}, GPa	3.03, 2.72, 2.70	2.82	0.19
G_{TZ}, GPa	2.78, 3.12, 1.76	2.55	0.71
Ultimate Strengths of Material D155, V_F = 36%			
Property and test plane	Test Values	Average	s.d.
UTS_L, (LT plane), MPa	891, 814, 883, 838	856	37
UTS_L, (LZ plane), MPa	679, 672, 685, 646	671	17
UTS_T, (TZ plane), MPa	26.6, 36.0, 30.4, 32.9, 29.0	31.0	3.6
UTS_Z, (ZT plane), MPa	21.7, 18.7, 20.4, 18.1	19.7	1.6
UTS_Z, (ZL plane), MPa	19.4, 17.7, 22.3, 17.1, 15.2	18.4	2.7
τ_{LT}, MPa	95.1, 82.1, 78.8	85.3	8.7
τ_{LZ}, MPa	79.6, 77.3, 77.1, 63.2	74.3	7.5
τ_{TZ}, MPa	19.9, 17.6, 12.0	16.5	4.0
*Shear properties listed were determined by notched beam, ASTM D5379			

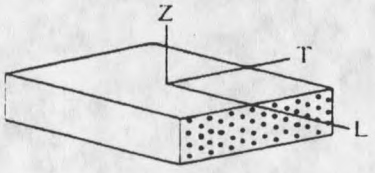


Table 4. Physical Elastic Constants for D155 Ortho-polyester Resin

Skin-Stiffener

Two models were constructed for the skin-stiffener geometry. The first model was built to analyze and confirm the elastic region of the stiffener experimental load-displacement curve. High strain gradient areas were located and analyzed using the failure criteria discussed in Chapter 2 to determine initial cracking locations. The second model was constructed to predict crack growth for monotonic and cyclic load cases after an initial crack was present.

A plane strain analysis using plane 82 quadrilateral elements was used in the skin-stiffener models, which were also constructed using individual lamina layers and not smeared properties. Half symmetry about the web of the stiffener was used to simplify the model by restricting the nodes along the mid-line to have zero (x)-displacement, shown in Figure 29. Three coordinate systems were constructed for the element generation of the first model. A coordinate system was developed for the web, bend region and the flange and skin regions. These coordinate systems were used to keep the orthotropic composite properties aligned with the local coordinate systems of the elements. Three material property sets were constructed. An orthotropic set was constructed for each glass fabric (DB120 and D155) and one isotropic set for the resin rich region between the web and stiffener. The coordinate systems and bend region mesh configuration are shown in Figure 30. The support from the test apparatus was modeled as a condition of no vertical (y)-displacement at a distance of 6.35 cm from the web

centerline. The vertical applied nodal force was normalized per unit width of the specimen and applied to the top of the web.

Once initial damage was introduced within the FEA model, the skin-stiffener was no longer symmetric. Thus, a full model was generated to represent the stiffener during crack propagation, shown in Figure 31.

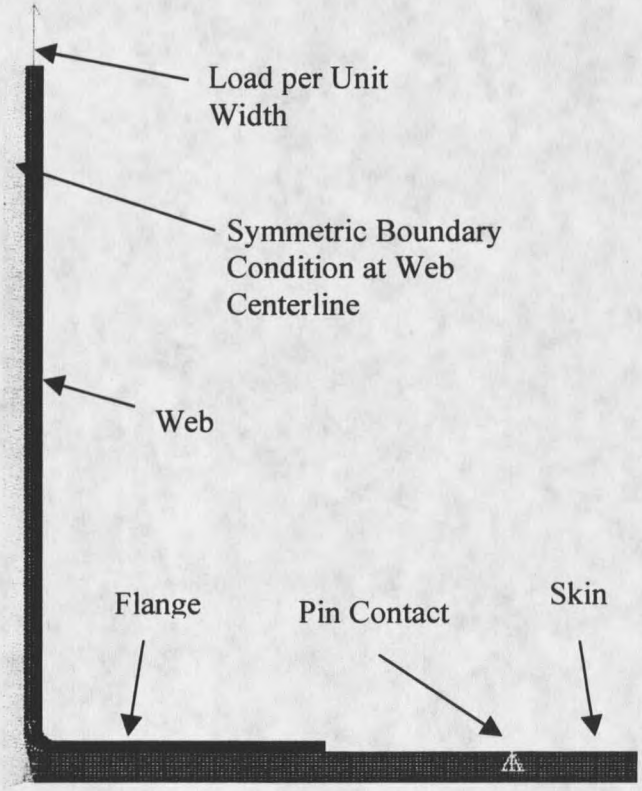


Figure 29. Symmetric Finite Element Model for Skin-Stiffener

Five coordinate systems were constructed for the discretization of the full model. The three sets of material properties that were used in the symmetric model were used in conjunction with the five local coordinate systems. One to one aspect ratios in areas that possessed high stress gradients were implemented while low stress gradient areas had

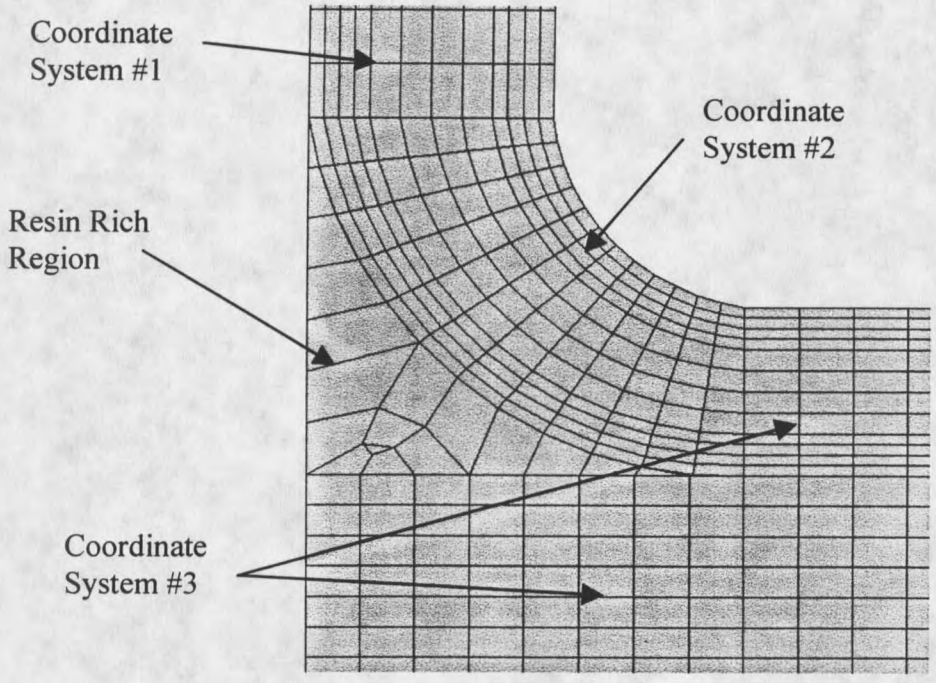


Figure 30. Coordinate Systems and Mesh for Symmetric Skin-Stiffener Model

aspect ratios of three to four. Elements surrounding the crack tip were highly refined to capture the stress gradients.

The increase in aspect ratios dramatically reduced the total number of elements required for mesh generation. One disadvantage of modeling individual fabric layers is that element heights can not exceed the height of the fabric layers. The use of smeared properties would eliminate this restriction. Much larger elements could then be used which in turn would lower the computer computational solution time. This skin-stiffener model was small enough that solving times were usually under five minutes on a Pentium 233Mhz machine. Smeared properties should be incorporated into larger 2-D or 3-D

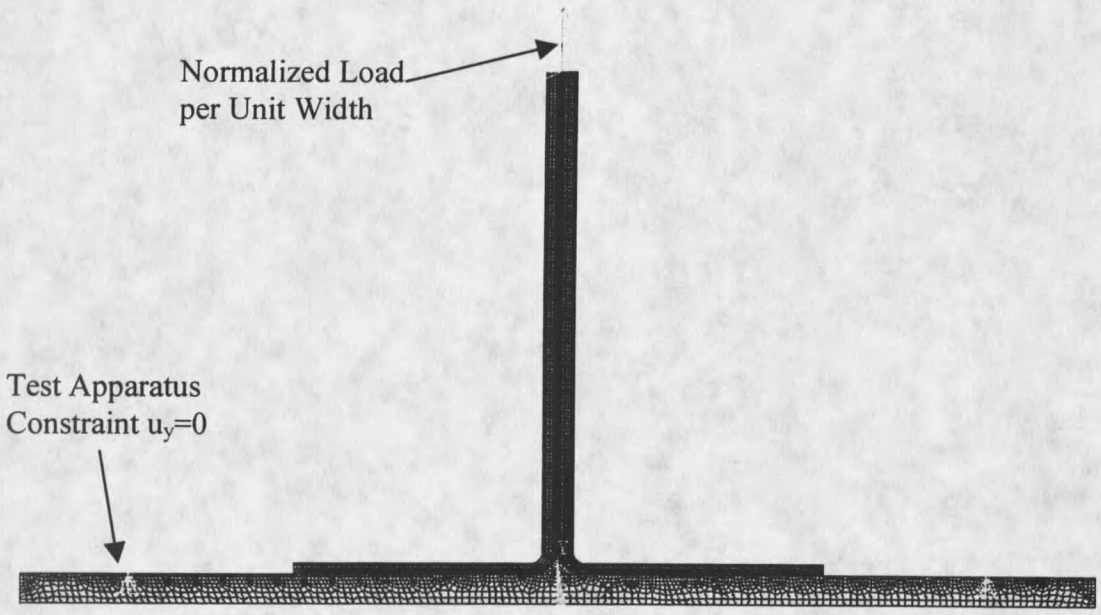


Figure 31. FEA Model for Crack Propagation

models with low stress gradient areas to minimize solution intervals. The final area and mesh configurations for the full model are shown in Figure 32.

The analysis of the specimens with FEA involved using the model without a crack to simulate initial behavior of the skin-stiffener in the elastic, undamaged state. High stress gradient regions were investigated at experimentally determined critical loads using the failure criteria previously described in Chapter 2. Delaminations were then inserted in the full non-symmetric stiffener model and G values were calculated using the VCCT method discussed previously in Chapter 2.

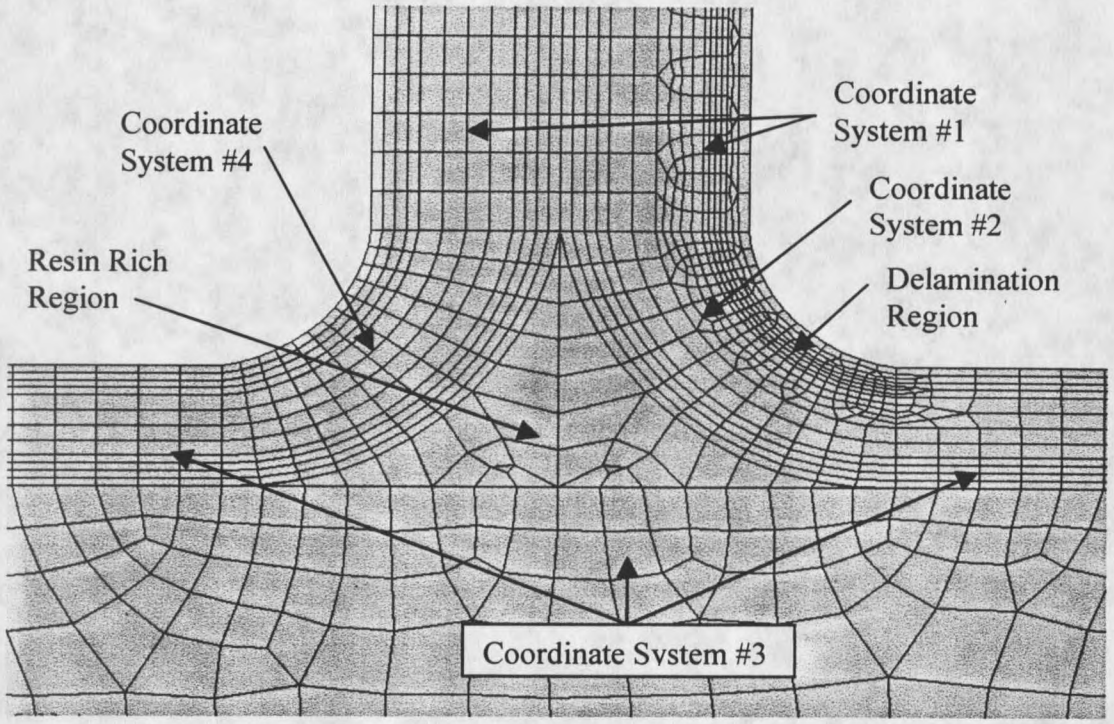


Figure 32. Coordinate System and Mesh For Skin-Stiffener Crack Propagation

CHAPTER 5

EXPERIMENTAL RESULTS AND DISCUSSION

A summary of the experimental results for the G_I, G_{II} and skin-stiffener test specimens are presented in this Chapter. Detailed results for each test are presented in Appendix A.

Static G_I Crack Tests

Static DCB Mode I (G_{Ic}) tests were conducted to examine interlaminar fracture toughness with the polyester CoRezyn matrix. Two ply configurations were tested: $[(\pm 45),90_2,(\pm 45)]_4$ and $[(\pm 45)_9, 90, (\pm 45)_8]$. Cracks were propagated along (45°/45°) and (90°/45°) interfaces to investigate toughness changes with different layup configurations, simulating crack locations in the skin-stiffener tests.

(90°/45°) Ply Interface

A plot of fracture toughness versus crack extension (where a* is the crack extension beyond the teflon starter film) is shown in Figure 33. The G_{Ic} versus crack length data were linear curve-fit for use in the FEA static crack growth analysis. G_{Ic} values calculated from the MBT method increased from an initiation value of 130 J/m^2 to an average plateau value of 461 J/m^2 once the crack had grown over 5 mm in length, as shown in Table 5. The results indicate that an R-curve effect exists in the polyester (90°/45°) configuration as noted by other investigators [5].

(45°/45°) Ply Interface

Fracture toughness versus crack extension data for the (90°/45°) ply interface is also shown in Figure 33. The (45°/45°) interface exhibited a similar R-curve behavior

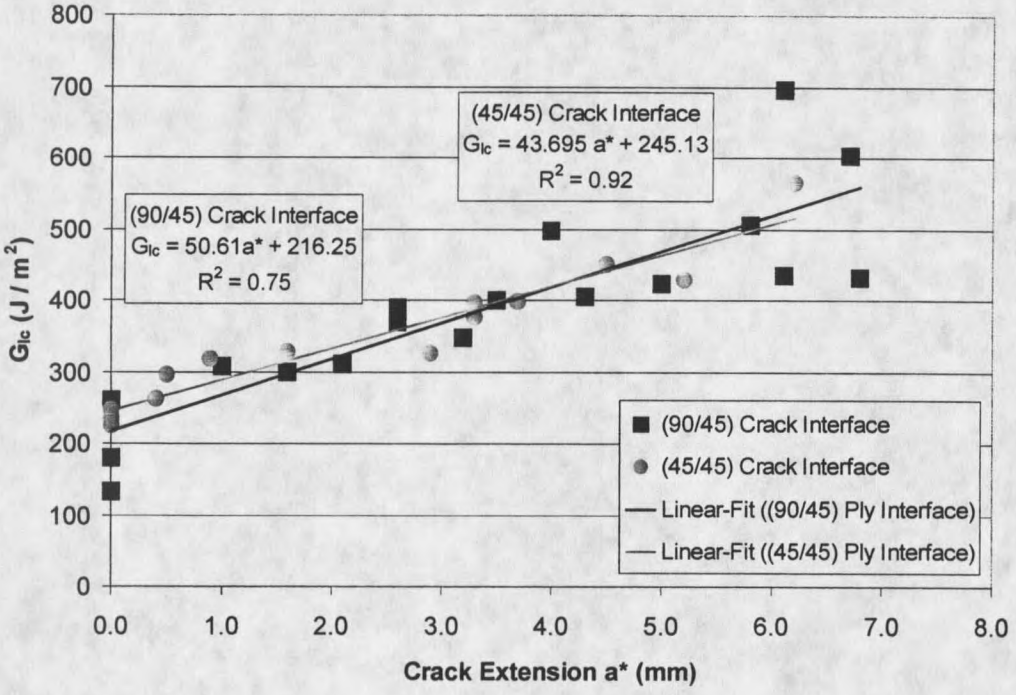


Figure 33. G_{Ic} Fracture Toughness versus Crack Extension

after initiation.

Other investigators have reported a similar R-curve behavior. Alif et al. [24] observed tow debonding in the fabric layers above and below the crack interface for a woven fabric carbon/epoxy interface. They reported that a single tow debond resulted in a G_{Ic} increase of 50 J/m^2. The excess energy involved in tow debonding was estimated from the difference between the smooth load/displacement curve and the peaks in

fracture toughness associated with the strand debonding process. Haugen [5] postulated that tow debonding effectively created a larger fracture process zone, as well as

DCB Layup (Ply Interface Delaminated)	G_{Ic} (J/m^2) a* < 2.1 mm	Std Dev.	# Points	G_{Ic} (J/m^2) a* > 2.1 mm	Std Dev.	# Points
$[(45)_9,90,(45)_8]$	248.8	75.4	5	462.1	106.5	12
$[(45),90_2,(45)]_4$	272.8	41.1	7	420.3	75.0	7

Table 5. G_{Ic} Values from Static DCB Tests

multiple crack paths. Delamination with multiple cracks required more energy than did a simple planar delamination. He observed that with tow debonding, the crack actually grows simultaneously at the mid-plane fracture surface and the tow-matrix interface one ply thickness away from the mid-plane. (Haugen [5] studied the multiple crack fronts in glass fiber/polyester resin $[(\pm 45)]_{10}$ DCBs). The increase in fracture toughness with crack length in the (90°/45°) interface was proposed to be the direct result of fiber bridging, multiple crack paths, and strand debonding. The larger process zone was observed in both sets of DCB specimens. A schematic of the crack profile is shown in Figure 34. The crack front began in the (90°/45°) interface, grew transversely through the 90° ply and delaminated the (90°/45°) interface and ultimately the (45°/45°) interface. The cracking in the (90°/45°) case grew along the path of least resistance. It is believed that the "actual" G_{Ic} values for the (90°/45°) DCB are slightly higher than the experimental results due to the fact that the crack front coalesced in the 45° plies and did not stay in the (90°/45°) interface.

The test results indicate a definite toughness increase with crack extension for both of the interfaces. Initiation values were very similar for both interfaces. The toughening in both cases can be attributed to fiber bridging and tow debonding. It should be noted that increases in fracture toughness were not great until the crack fronts had grown beyond 2 mm. This would indicate that the designer should not rely on fiber

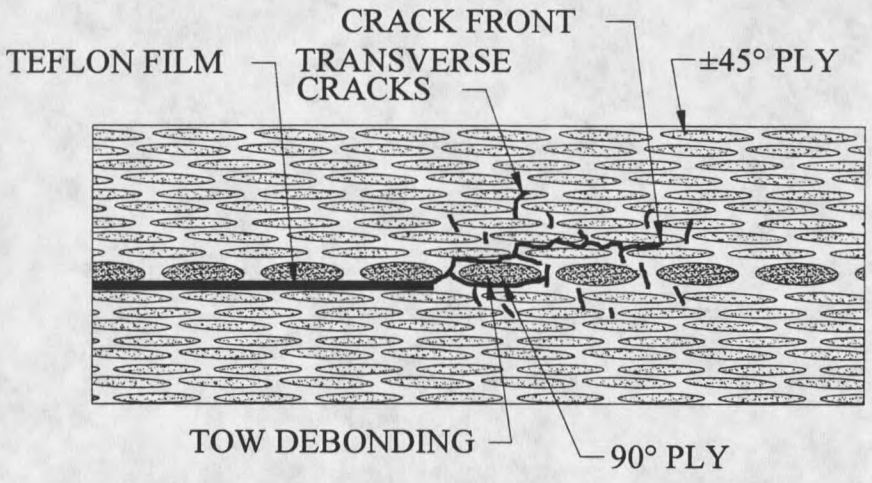


Figure 34. Detail of Static Crack, (90°/45°) Interface, DCB Specimen

bridging and strand debonding to increase fracture toughness for small cracks. A better method of design would be to assume small material flaws and insure that growth of these flaws will not occur at the G_{Ic} initial value. Interlaminar stresses could be reduced by changing reinforcement architecture [25].

G_I Fatigue Crack Growth Tests

Similar DCB Mode I crack growth tests were performed under fatigue loading. The fatigue cracks were propagated at the (90°/45°) ply interface at an R-value of 0.1. An

initial fatigue test showed an R-curve effect similar to that exhibited in the static tests for longer cracks. This was evident due to the fact that as measurements were taken during the cyclic tests, the growth rate became smaller as the G became larger. The DCB crack path is shown in Figure 35. The fatigue damage zone possessed little or no transverse cracking. The damage zone in the vicinity of the crack front was smaller than the static tests due to the fact that, during fatigue crack growth, smaller loads and displacements result in a lower strain energy within the specimen. The crack front had a tendency to propagate toward the (45°/45°) interface.

Subsequent fatigue tests were performed with crack extensions of 5 mm or less to reduce R curve influences. The R-curve effect was minimized so an accurate database

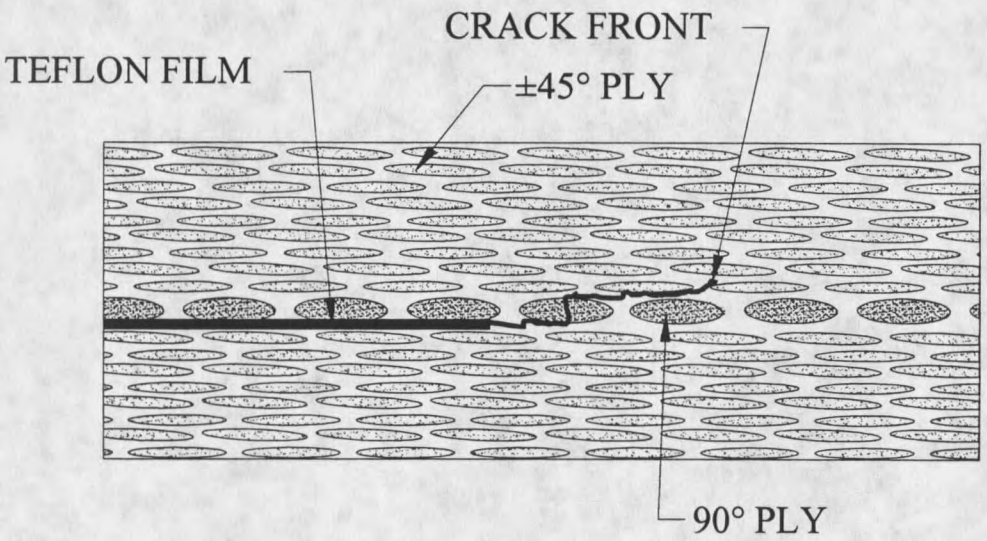


Figure 35. Detail of Fatigue Crack, (90°/45°) Interface, DCB Specimen

could be assembled for analysis of the early stages of damage initiation and growth. The test data indicate that R-curve effects are very small or virtually nonexistent for short

crack lengths. Once cracks grew to lengths over 5 mm, the R-curve began to "level off" and plateau. Other investigators have reported similar behavior. Mandell and Tsai [21] observed similar R-curve effects and plateau regions for wet and dry DCB carbon fiber tests. They proposed that this "leveling" effect was the result of the full development of the fiber bridging zone, as evidenced by the constant G_{Ic} values for long crack lengths.

The growth rate (the change in crack length per cycles (da/dN)) versus the maximum strain energy per cycle (G_{Imax}) is shown in Figure 36. The complete

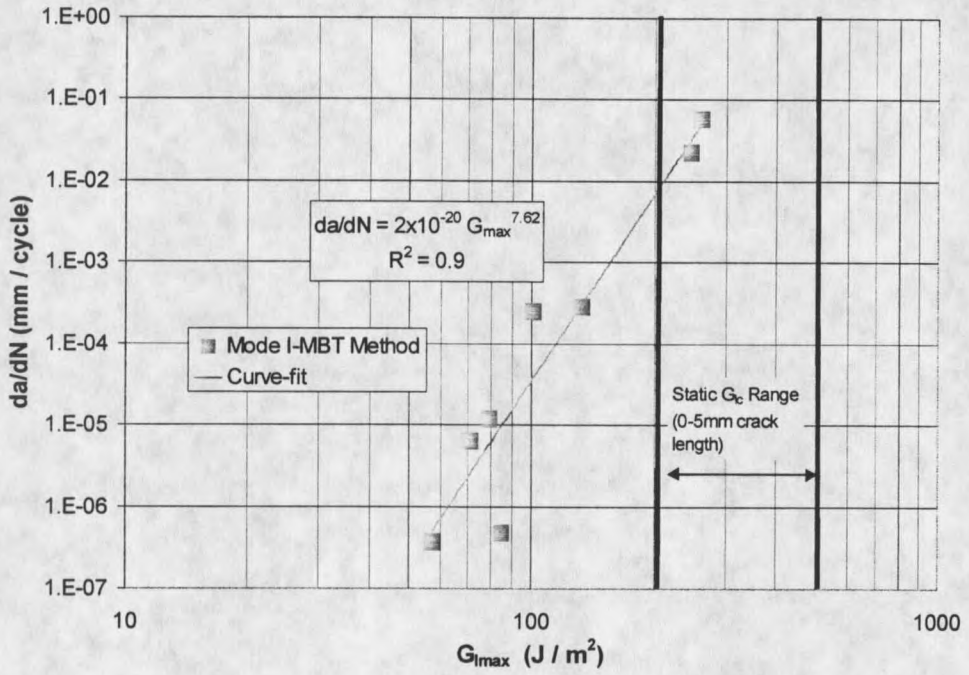


Figure 36. Mode I – (da/dN) versus G_{Imax}. $[(45)_9,90,(45)_8]$ Laminates Cracked in the (90°/45°) Interface. Short Crack Data (below 5 mm), R = 0.1, DCB Specimen.

characterization of delamination growth under cyclic loading should be bounded at the upper and lower ends. The lower bound is the threshold below which delamination

growth does not occur and is typically referred to as the Threshold Strain Energy, G_{th}. The upper bound is the Critical Strain Energy Release value G_{Ic}, above which the growth is unstable. The static G_{Ic} values are typically used to indicate the cyclic G_{Ic} because this is the point which growth occurs during one cycle. Cyclic mode I tests were performed at lower and lower load levels to converge on the threshold energy, G_{th}. No growth occurred on a DCB specimen with a calculated G_{Imax} of 50 J/m^2 for 2 million cycles. Thus, G_{th} was assumed to occur between 50 J/m^2 (no growth per cycle) and 57 J/m^2 (3.65×10^{-7}mm/cycle). The data were fitted by the power law relationship previously described in Chapter 2. An exponent of 7.6 best correlated the DCB data.

Static G_{IIc} Crack Tests

Static ENF tests were conducted to examine the Mode II interlaminar fracture toughness (G_{IIc}) of cracks propagated between (90°/45°) plies (Figure 30). The same specimens were used for ENF and DCB tests: ortho-polyester matrix with a $[(\pm 45)_9, 90, (\pm 45)_8]$ ply layup. A typical load versus actuator displacement curve is shown in Figure 37. Typically, while the ENF test is in progress, the crack grows in an unstable manner, creating a "popping" noise due to the large energy release once the critical load is reached. The (90°/45°) interface ENF cracks grew in a very stable manner for several millimeters up to 10 mm before the ENF midspan was reached, Figure 38. At that point, the critical load was reached and the crack grew in an unstable manner. Following the ASTM E399 metals fracture test standard, the G_{IIc} values were obtained by

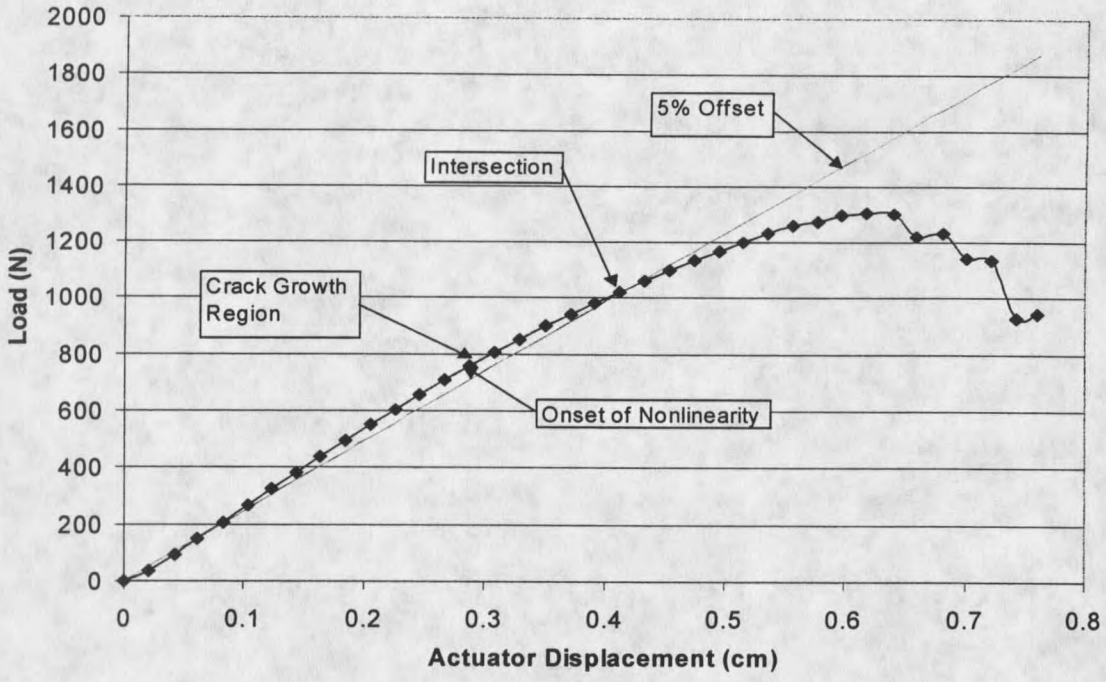


Figure 37. Typical Load versus Actuator Displacement for an ENF Specimen

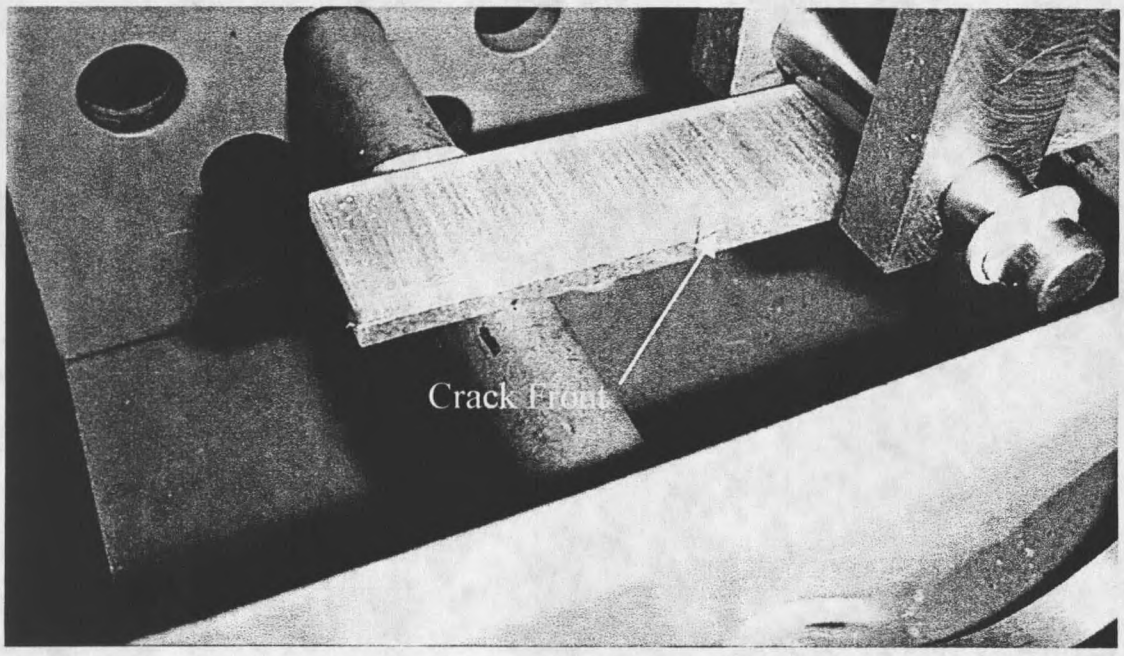


Figure 38. ENF Test in Progress with Stable Crack Growth

a 5% offset method, inserting a line at 95% of the slope of the linear portion of the load-displacement slope [26]. At the point of intersection, G_{IIc} was calculated using Equation 27, discussed in Chapter 2. This method ensured repeatability among test specimens since the initial change in slope could not be solely characterized as either crack growth or matrix cracking. It was assumed that some interaction of crack growth and matrix cracking contributed to the initial change in slope of the load-displacement curve.

After examining the ENF test specimens, it was apparent that a large damage zone existed that consisted of tortuous multiple crack fronts as shown in Figure 39. Multiple

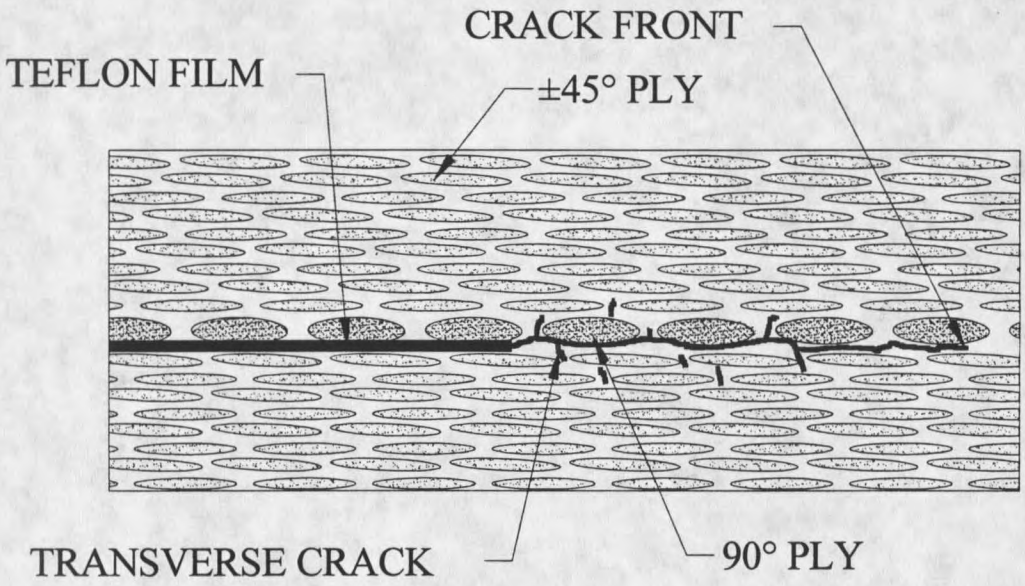


Figure 39. Detail of Static Crack during Stable Crack Growth, ENF Specimen

transverse cracks occurred in the 90° and ±45° plies. These multiple fronts blunted the damage zone and increased the resistance for growth of the main crack. Upon unstable crack growth, the main delamination site always followed the (90°/45°) interface, with no transverse cracking or branching. The static ENF test results are given in Table 6.

ENF Layup	Interface Delaminated	G_{IIc} (J/m^2)	Std Dev.	# Points
$[(45)_9,90,(45)_8]$	(90°/45°)	941.8	260.6	3

Table 6. G_{IIc} Values for Static ENF Tests

G_{II} Fatigue Crack Growth Tests

Mode II fatigue crack growth tests were also performed on the same (90°/45°) interface as for the static Mode I tests with an R-value of 0.1. The behavior of the initial fatigue test also showed an R-curve effect similar to the cyclic DCB tests discussed earlier. After the initial ENF cyclic test, subsequent tests were performed with crack extensions less than 5 mm. A plot of change in crack length per cycle (da/dN) versus G_{IImax} is shown in Figure 40.

The data were fitted to the power law relationship (Equation 28), previously described in Chapter 2, giving an exponent of 5.2. The cracks grew in a stable manner in the (90°/45°) interface as shown in Figure 41. No transverse cracking occurred in the ENF fatigue specimens in the G_{IImax} range shown. It is believed that this was primarily due to lower strain energy, relative to the static tests in the crack front vicinity due to lower cyclic loads and deflections. The tests were conducted for short cracks lengths (less than 5 mm) to reduce toughening and R-curve effects.

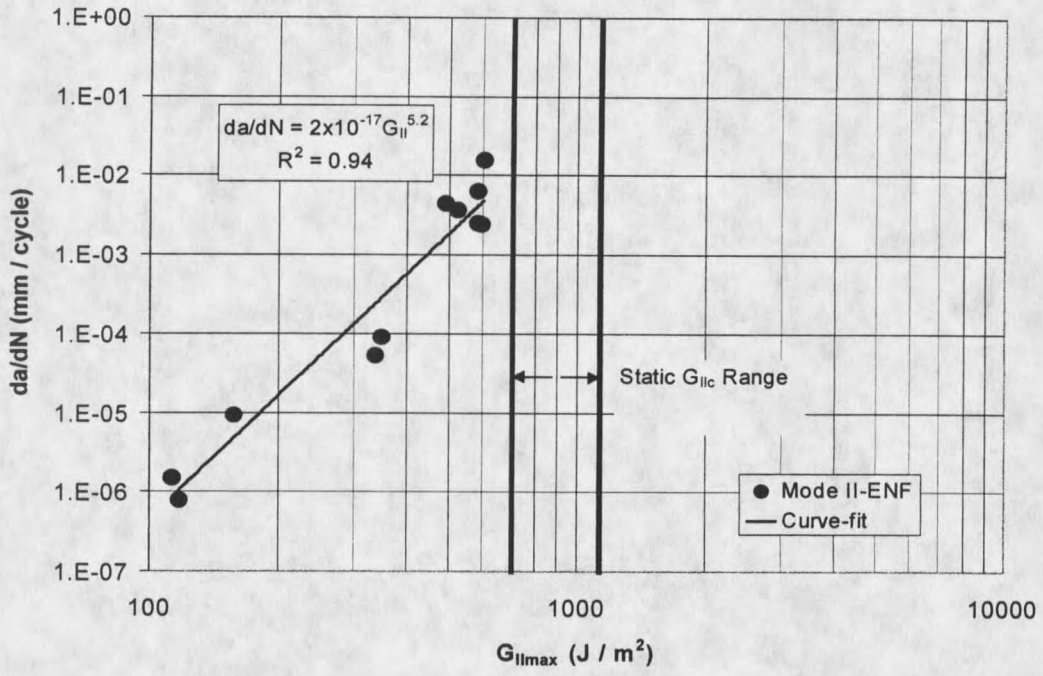


Figure 40. Crack Growth Rate versus G_{IImax}, R = 0.1, ENF Specimens

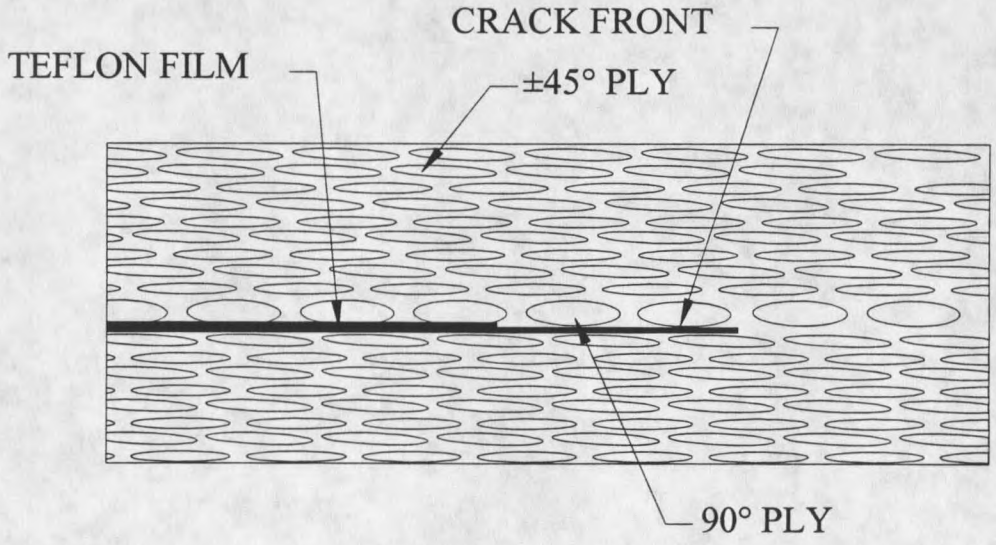


Figure 41. Detail of Fatigue Crack, ENF Specimen

Static Skin-Stiffener Tests

Two series of static pull-off tests were performed on the skin-stiffeners. The first series of tests used ortho-polyester matrix material substructures to determine the load when initial damage occurred and the critical load to drive the crack when the delamination was present. A second series of static pull-off tests were then performed using several resin systems to observe the matrix effect on initial damage and ultimate load.

Ortho-Polyester Matrix

For the ortho-polyester matrix specimens, the stiffeners were loaded manually until an initial crack "popin" was observed. Complete control of the test was necessary so that it could be stopped for inspection after initial damage had occurred. To achieve this result, the test was performed manually using the Instron actuator displacement keys located on the control panel. Initial damage of the skin-stiffener was accompanied by an audible "pop" during the test. The test specimen was immediately unloaded and the initiation load and initial crack length were recorded, using a scaled loupe, while the specimen was still in the three point test apparatus (Figure 24). By leaving the specimen in the test apparatus, continuity between initial and critical load tests was maintained.

The specimen was then manually loaded again until large scale delamination crack growth was observed. The maximum load to drive the crack was then recorded. The maximum values were gathered by the Instron computer ultimate values menu. The results of these test specimens are presented in Table 7.

The initial crack "popin" occurred in the fillet area between the web and flange. This was expected since the largest interlaminar strain gradient occurred in this area

(Chapter 6). The delamination crack was in the (90°/45°) interface, shown in Figure 42.

Initial Damage		Critical Load for Crack Growth (N / cm)	Number of Tests
Load (N / cm)	Crack Length (mm)		
94.9(6.8)	2.48 (0.2)	128.6 (7.9)	6

Table 7. Static Load and Crack Length Data for Ortho-polyester Skin-Stiffeners; ( ) indicate standard deviation

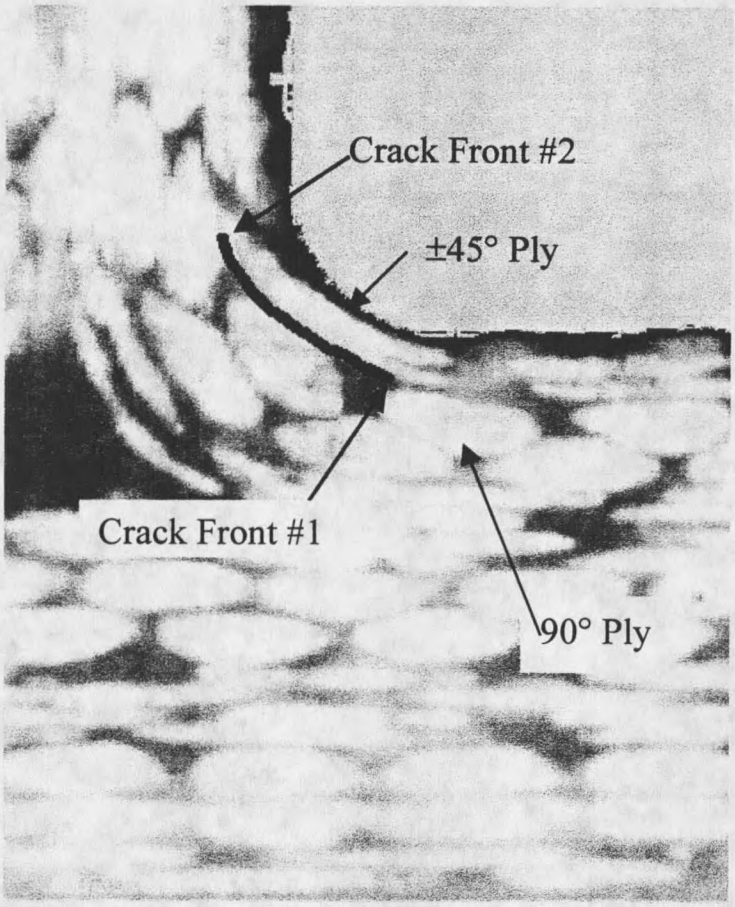


Figure 42. Location of Delamination and Nomenclature for Crack Fronts.

As the structure was loaded for the second time, the upper crack front (crack front #2) grew toward the web in the (90°/45°) interface. The lower crack front (crack front #1)

grew transversely through the 90° ply and arrested. Haugen observed similar delamination locations and growth for ortho-polyester skin-stiffeners [5].

Resin Comparison for Static Tests

Based upon these results, it appeared that the brittle ortho-polyester matrix material was a limiting factor in the delamination resistance of the stiffener. Therefore, increasing the resin toughness should result in greater delamination resistance. Resin toughness plays a dominant role in the interlaminar fracture of composites. Bradley [27] reported that increasing the ductility and decreasing the yield strength of the matrix resin increases the delamination fracture toughness by increasing the plastic zone size ahead of the crack tip, giving greater load redistribution away from the crack tip and more crack tip blunting. A number of resin systems have been investigated by Orozco [28] and Li [29], from which three other resin systems of interest were selected.

Skin-stiffener sections with two vinylester resins, 8084 and 411, and one additional polyester resin, isophthalic, previously described in Chapter 3, were tested. The results for initial damage and maximum load are presented in Table 8. The specimens were loaded with a displacement controlled ramp until final pull-off occurred. Pull-off was defined as flange-skin separation.

All of the skin-stiffeners delaminated in the bend region. The toughened vinylester 8084 matrix material demonstrated good resistance to damage with an initial damage load of 189.3 N/cm. A typical plot of load versus displacement for the vinylester 8084 skin-stiffener is shown in Figure 43. The 8084 vinylester was anticipated to perform the best in the pull-off tests since it was the only rubber modified toughened resin tested.

Matrix Material	Initial Damage Load (N/cm)	Displacement at Initial Damage Load (cm)	Ultimate Load (N/cm)	Number of Specimens
Ortho-polyester	87.0 (5.9)	0.22 (0.02)	143.7 (1.5)	3
Iso-polyester	98.2 (2.2)	0.24 (0.01)	166.1 (1.2)	3
411 vinylester	143.9 (60.7)	0.44 (0.24)	198.3 (1.0)	3
8084 vinylester	189.2 (25.6)	0.48 (0.08)	221.0 (10.6)	3

Table 8. Table of Load and Displacement Data for Different Resin Skin-Stiffener. ( ) indicate Standard Deviation



Figure 43. Load versus Displacement for 8084 Vinylester Skin-Stiffener

Skin-stiffener Fatigue Tests

Once a static baseline had been established for the skin-stiffeners, cyclic loading was investigated. Two series of cyclic tests were performed. The first series of tests used the ortho-polyester matrix material to determine initial damage location, rate of damage accumulation, change in structure stiffness, change in maximum bending strain and cycles to failure at specific load levels. The second series of fatigue tests was performed on skin-stiffeners with different resins to observe cycles to failure at specific load levels.

Ortho-polyester Fatigue Tests

An initial "popin" crack similar to that in static tests occurred in the fillet area between the web and flange for the fatigue specimens during the period of the cyclic test (crack #1). The delamination crack was in the (90°/45°) interface in the bend region (step #1) shown in Figure 44.

The upper crack front (step #2) grew into the web region but stayed in the (90°/45°) interface. The lower crack front (step #3) grew transversely through the 90° ply and arrested. It is believed that the load paths changed within the stiffener when the crack grew transversely through the 90° ply. When the transverse crack appeared, additional transverse cracks occurred at the (noodle/45°) interface (crack #2). A delamination then propagated between the flange and skin (45°/45°) interface causing a significant increase in compliance which resulted in stiffener/flange pull-off.

As damage accumulated within the bend region, a reduction in specimen stiffness occurred. This resulted in an increase in the maximum actuator displacement as shown in

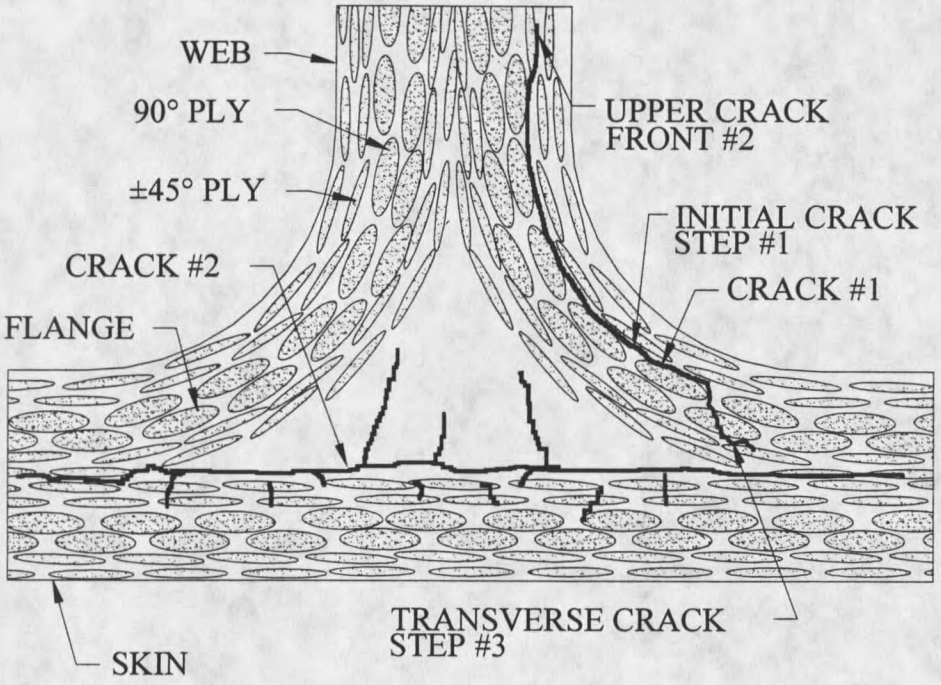


Figure 44. Skin-Stiffener Crack Sequence during Fatigue Loading

Figure 45. As the compliance of the stiffener increased, the maximum bending strain in the skin showed a similar trend. (This could be of interest in determining damage states in turbine blades. Changes in maximum strain could be recorded at areas of interest on the turbine blades. When damage initiates in the blade section, possible discontinuities or slope changes would occur in the strain plots.) The growth rate (da/dN) was obtained from crack growth observations during testing using a scaled loupe. G values were

determined using FEA VCCT stiffener models. A crack growth per cycle (da/dN) versus G_{max} plot is shown in Figure 46, where G_{max} was determined by FEA as described in Chapter 4.

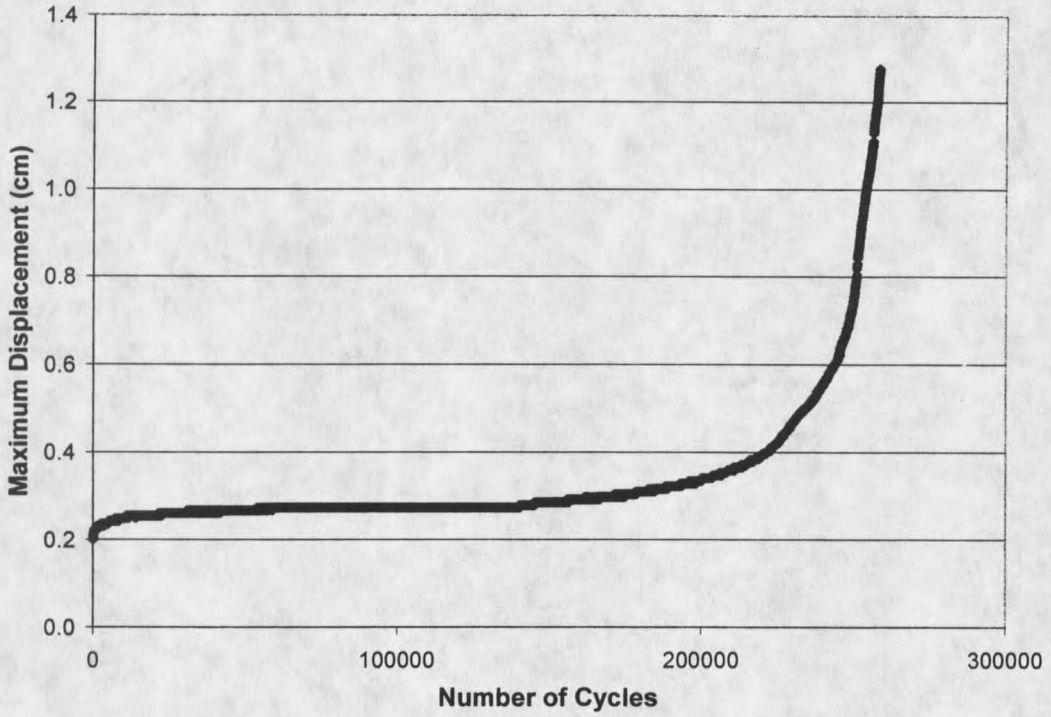


Figure 45. Ortho-polyester Skin-Stiffener Maximum Cyclic Displacement versus Number of Cycles

Resin Comparison in Fatigue Tests

Performance of the different matrix materials under cyclic loading conditions was investigated with an R-value of 0.1. As in the static tests, two vinylester resins, 8084 and 411, and one polyester resin, isophthalic, previously described in Chapter 3, were tested.

Damage was initiated within the bend region on all the skin-stiffener specimens.

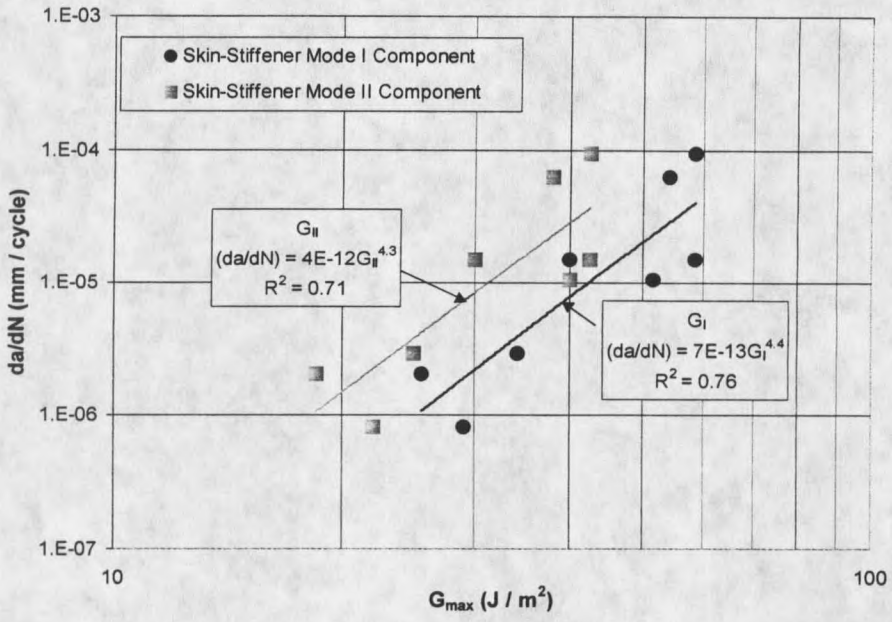


Figure 46. Fatigue Crack Growth Rate versus G_{max} in (90°/45°) Interface of Ortho-polyester Skin-stiffeners

All cracks formed in the (90°/45°) interface and propagated in a manner similar to the fatigue crack growth in the ortho-polyester stiffeners. Failure was defined as a maximum cyclic deflection of 0.43 cm. This was the displacement for initial damage for the static ortho-polyester skin-stiffener specimens.

The maximum cyclic load versus number of cycles to failure is plotted for each of the matrix materials in Figure 47. The vinylesters operated at the highest maximum loads to equivalent cycles to failure when compared to the three other matrix materials. The 8084 vinylester produced the largest initial and maximum loads during the static load tests, and also performed the best on an absolute load scale during fatigue testing. However, when the fatigue sensitivity is viewed relative to the static performance by

normalizing the cyclic loads by the static failure load, the order reverses. Now the 8084 system shows the most rapid loss in load carrying ability relative to its static strength (Figure 48). Also demonstrated in Figure 48, the polyester resin systems can operate at higher percentages of their maximum static loads when compared to the vinylester resin systems.

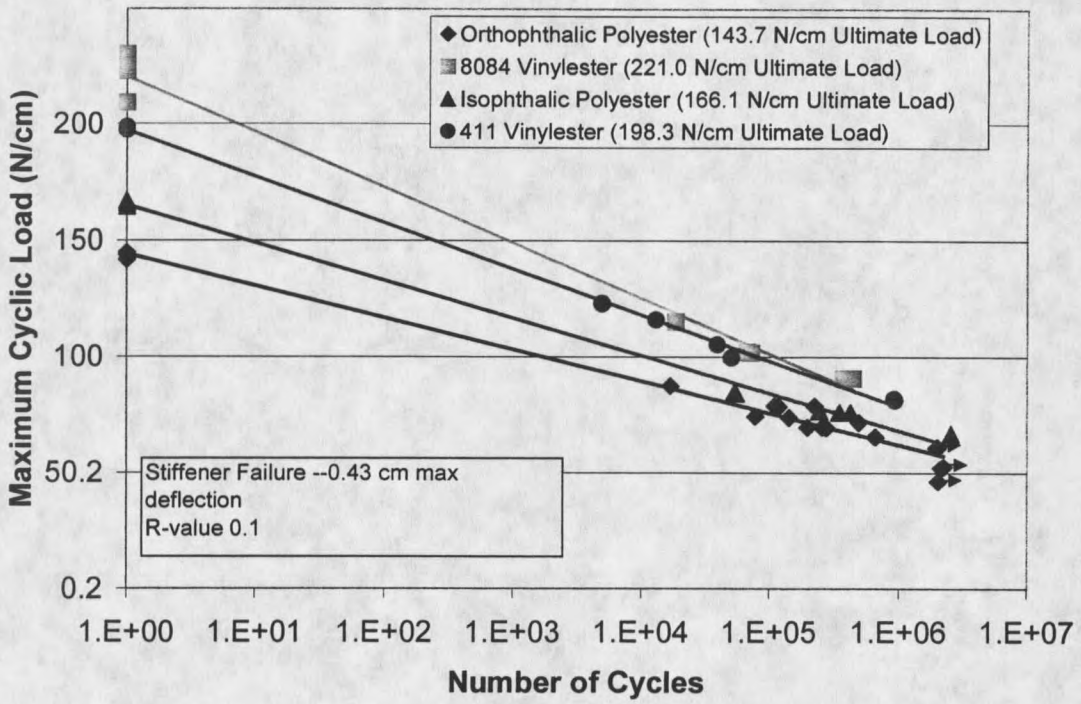


Figure 47. Maximum Cyclic Load versus Number of Cycles to reach a Deflection of 0.43 cm.

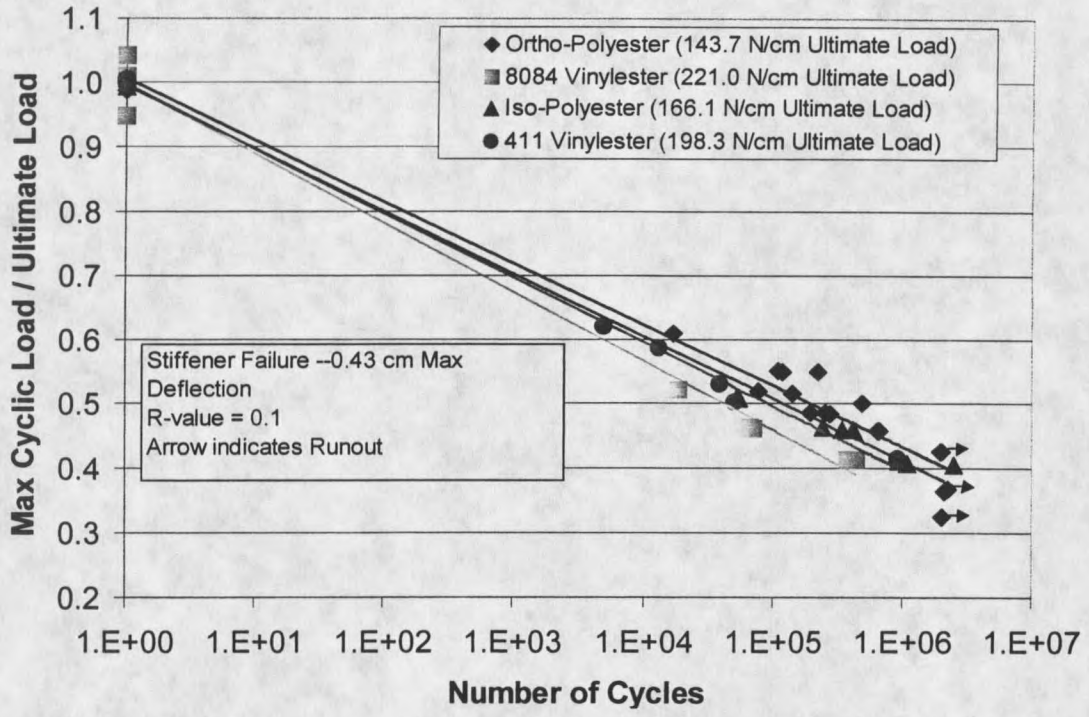


Figure 48. Maximum Cyclic Load / Ultimate Monotonic Load versus Number of Cycles to reach a Deflection of 0.43 cm.

CHAPTER 6

FINITE ELEMENT RESULTS AND CORRELATION WITH EXPERIMENTS

The results of numerical modeling performed with the ANSYS 5.5 finite element analysis (FEA) code are presented in this chapter. Comparisons are made with experimental data, and a methodology for fatigue design is outlined in this chapter. The finite element models were dependent upon accurate elastic and strength properties for the composite system. Properties used in the FEA models were taken from the MSU Database [3].

DCB specimens were first modeled to establish the ability to correlate results from the FEA using the Virtual Crack Closure Method (VCCT) with the established MBT method. The DCB specimens were initially modeled using 3-D continuum elements to justify the use of 2-D plane strain continuum elements. Once these techniques were established, the same method was applied to cracks in skin-stiffener specimens.

DCB models

To implement the FEA models, a well defined fracture toughness database had to be used in conjunction with the engineering and strength material properties. The FEA method was validated with the $[(\pm 45)_9, 90, (\pm 45)_8]$ DCB test results. The DCB models were analyzed to gain confidence in the applied methodology and numerical techniques. The mesh size near the crack front was governed by the (a/da) ratio. Recall that independent work performed by Haugan and Raju [5, 30, 31] demonstrated that (a/da)

ratios must be greater than 25 for accurate G predictions, where (da) is the element size at the crack tip and (a) is the crack length.

A 3-D model was analyzed to observe any possible width effects and to see if any accuracy or information would be sacrificed using a 2-D plane strain or plane stress model. The 3-D model was performed using the critical load for a specified crack length from an actual experimental static DCB test, shown in Figure 49.

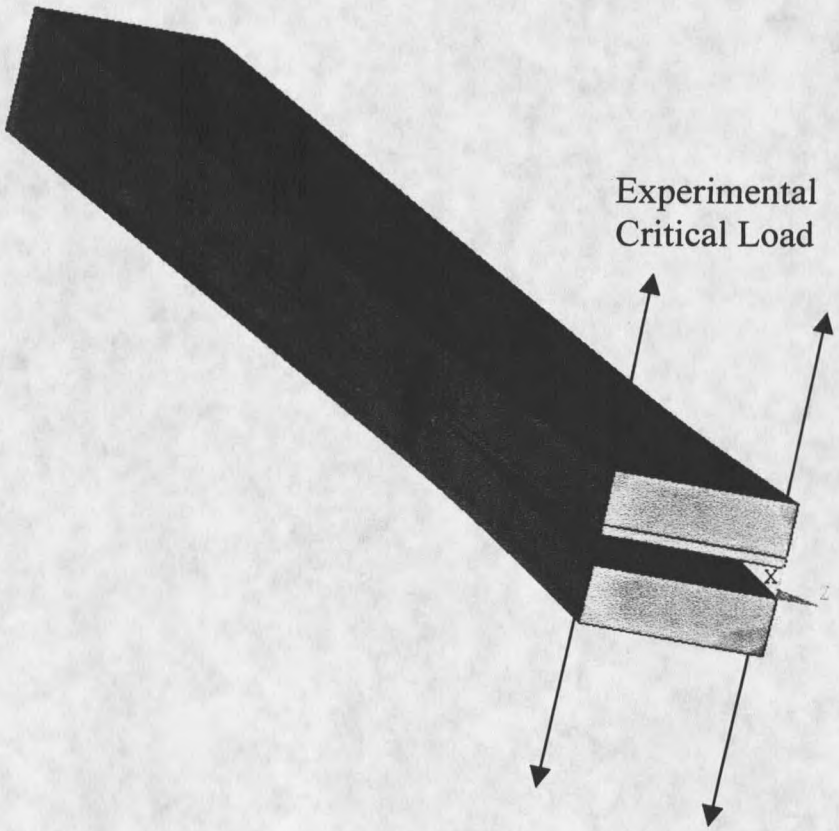


Figure 49. 3-D DCB FEA Model

The actual DCB specimen modeled was DCB 870. The critical load, 23.4 N/cm, was divided by the total number of nodes across the width of the DCB. This force per node value was then applied as a nodal load to each node at the tip of the DCB and boundary conditions were applied as described in Chapter 4. A plot of strain energy, G_I, versus the normalized distance from the DCB center is shown in Figure 50.

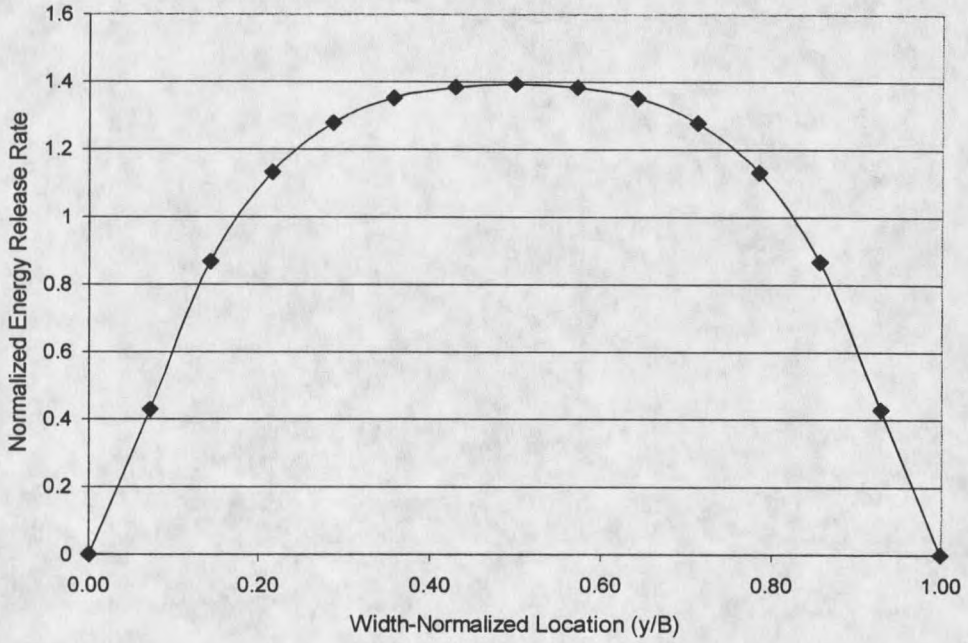


Figure 50. Normalized Strain Energy Release Rate for DCB Model with a 42.7mm Crack Length (3-D solid elements).

The horizontal axis in the figure was defined such that y/B = 0 corresponds to one of the DCB free edges, and y/B = 0.5 corresponds to its center. Each data point in the figure represents the energy release rate at the center of a local area of crack closure. Energy release rates in the figure were normalized by the total energy release rate, for the

entire width, as determined by the finite element results. To avoid later confusion, energy release rates (G_I) for the 3-D model will be for the entire width as "average values".

The results for the DCB were not surprising. Davidson, Kruger and Konig [25] confirmed that peak energy release rates occur near the center of the specimen width for $[\pm 30/0_{12}/\pm 30]_s$ DCBs. They also demonstrated that certain non-symmetric stacking sequences exhibit varying amounts of coupling between the primary bending curvature and either the transverse bending curvature or the twist curvature. Wang and Raju [32] reported a similar trend for skin-stiffeners with plate elements. Raju and Crews observed a rise in G_I-values at the mid-plane section (y/B=0.5) and a significant drop at the free edge in the 3-D analysis of double cantilever beam and other similar specimens [33].

A 2-D plane strain model of DCB 870 was then analyzed to compare to the 3-D results. The 2-D plane strain model used the critical load of 23.4 N/cm, for a specified crack length of 42.7mm, from the experimental static DCB 870 test. The 2-D, 3-D and experimental MBT G_I results for DCB 870 are presented in Table 9. The maximum G_I value in the 3-D case is about 40% higher; it is assumed that, in practice, the crack front will curve sufficiently to flatten the G_I variation through the thickness, so that the average value is more meaningful.

Experimental MBT Mode I DCB		3-D FEA Model (average through thickness)		2-D Plane Strain Model	
G_{Ic} (J/m^2)	% Difference	G_{Ic} (J/m^2)	% Difference	G_{Ic} (J/m^2)	% Difference
255.6	--	243.3	4.8	260.9	2.1

Table 9. Comparison of Three Methods for Calculation of G_I Values in DCB Specimens: MBT, 3-D FEA, and 2-D FEA (DCB Specimen 780 with a 42.7mm Crack Length)

The 2-D plane strain model was then used to correlate incremental increases in crack length for the same experimental DCB sample. The results for G_{Ic} versus crack length are shown in Figure 51.

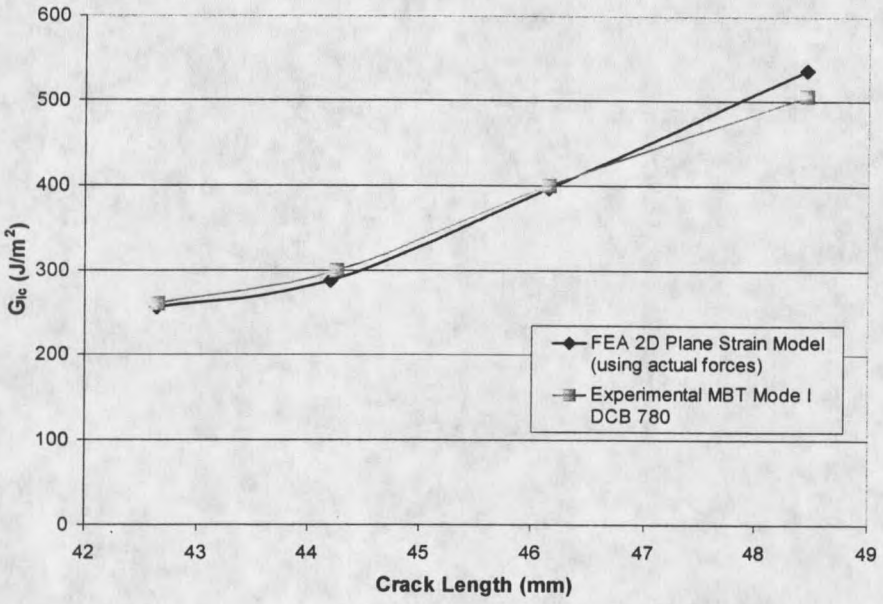


Figure 51. G_{Ic} versus Crack Length Calculated by 2-D Plane Strain FEA Model and MBT (DCB 780 Specimen).

The 2-D plane strain model using experimental crack length and force values is in good agreement with the Modified Beam Theory (MBT). The maximum percent difference was 6%. These results show that the FEA model using the VCCT correlates with the MBT results for several crack lengths and forces. The final deformed shape and stress in the vertical direction for the plane strain model is shown in Figure 52.

The average 3-D model G_I result was lower than the MBT and 2-D plane strain results. The differences in the strain energy may be due to errors in the FEA models, material properties, local affects due to tow debonding or assumptions about the stress

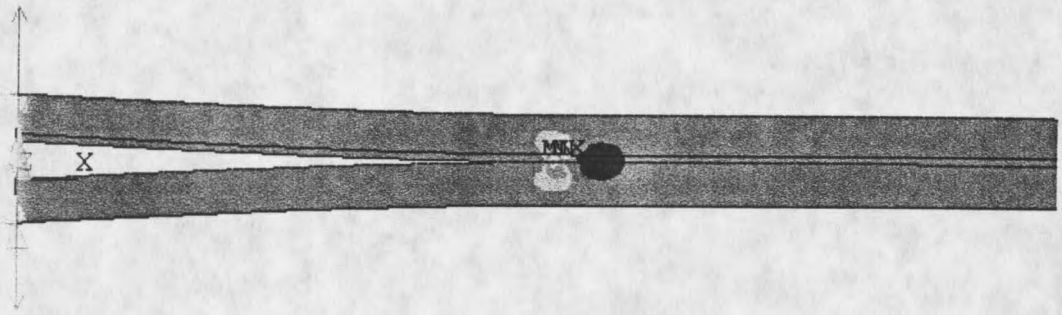


Figure 52. Deformed DCB Model with Transverse Stress Field Contour Plot

region near the crack tip. This may indicate that the DCB specimen was thick enough to behave overall as a plane strain test with negligible edge effects and no plane stress characteristics.

Skin-Stiffener Models

The skin-stiffener was modeled in ANSYS as described in Chapter 4. The goals of the skin-stiffener modeling were to predict static linear displacements, initial damage load and location using the maximum strain failure criterion (Equations 1, 2, & 3). After the initial damage load and location were known, the determination of the critical load to propagate the "pop-in" crack was of interest. Finally, determination of fatigue life at specified load cycles was to be analyzed and predicted using DCB and ENF data. The bend region of the skin-stiffener was the prime area of interest. This was the damage initiation site for both the static and cyclic tests.

Static Skin-Stiffener Comparison

The symmetric half model of the skin-stiffener was incrementally loaded with no damage to confirm the stiffener experimental linear displacement and bending strains. A plot of load versus displacement for the experimental specimen and FEA model are shown in Figure 53. The FEA model showed good agreement with the experimental displacement data. The FEA results differed from the average experimental data by 7%. The difference was attributed to possible differences in material properties for the skin-stiffener in the detail and global regions.

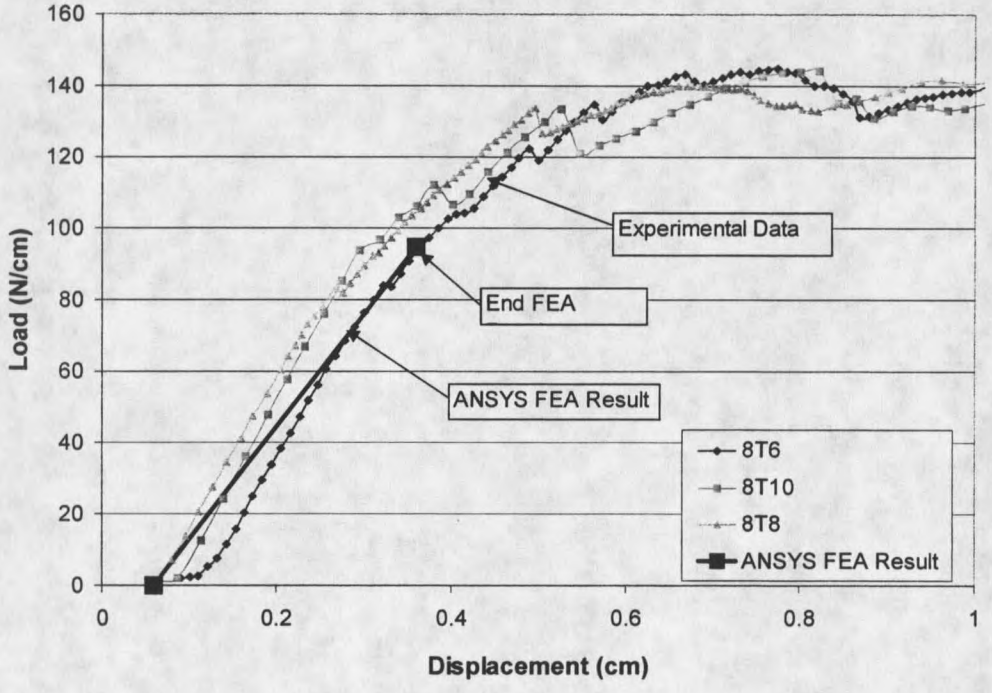


Figure 53. Comparison of Load versus Displacement for FEA Model and Three Experimental Ortho-polyester Skin-Stiffener Test Results

Once displacements and strains were confirmed using the FEA model, initial failure analysis was performed to determine the local failure location and load to initiate damage. Experimental observations showed that delaminations occurred at the (90°/45°) interface. The strains in the bend region were calculated using a load of 1 N/cm. Since the model was a linear elastic analysis, the strains were scaled until failure occurred using the maximum strain criterion (Equations 1, 2, & 3). The 1 N/cm load was multiplied by the scale factor to determine the initial damage load. Initial damage load was obtained by linearly scaling the 1 N/cm load and strains until a maximum strain was obtained. These maximum strain values are listed in Table 3. Before strain results could be extracted from the model, the output had to be viewed in the cylindrical coordinate system used to create the stiffener bend region. Typical contour plots in the bend region for the

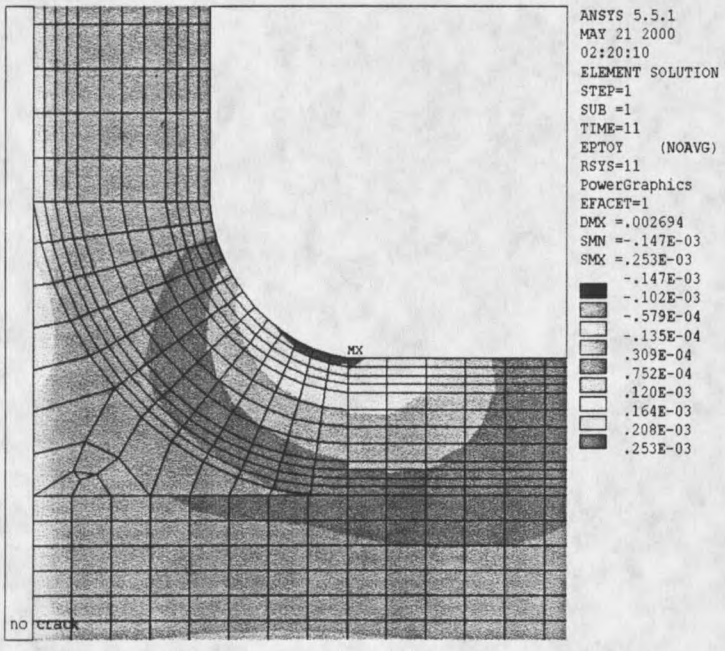


Figure 54. Skin-Stiffener Tangential Strain Plot at the Bend Region (no crack).

tangential and radial strains are presented in Figures 54 and 55 respectively. The strains were rotated from the global coordinate system to the local cylindrical coordinate system so strains were tangent and normal to the bend radius.

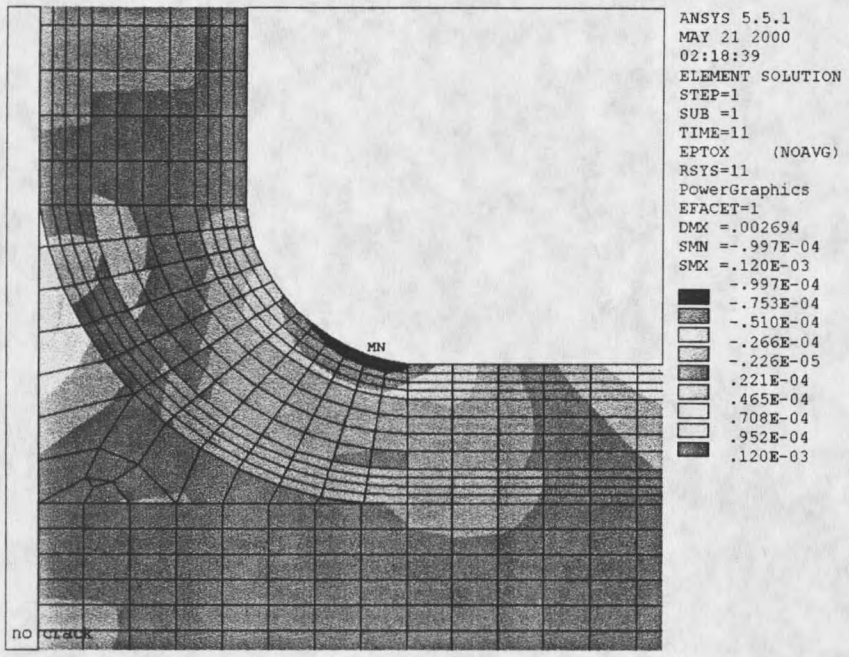


Figure 55. Skin-Stiffener Radial Strain Plot at the Bend Region (no crack).

In the bend region local coordinate system, the (x) direction was the radial direction, the (y) direction was tangent to the bend radius and the (z) direction was orthogonal to (x) and (y).

The predicted initial damage load is shown in Table 10.

Ply	Maximum Strain Criterion Initial Damage Load (N/cm)	Average Experimental Initial Damage Load (N/cm)	Percent Difference (%)
45°	82.6	94.9	13

Table 10. Predicted Initial Damage Load and Location

The maximum strain criterion predicted an initial damage load of 82.6 N/cm. The tensile failure occurred in the bend region 45° ply due to interlaminar radial stresses. The predicted damage load had a percent difference from experimental results of 13%. This was considered to be acceptable accuracy given the complicated damage states outlined in Chapter 5.

Once the initial damage location was determined, the nonsymmetric model was analyzed using a crack length of 2.48 mm inserted between the (45°/90°) plies and an applied load of 128.6 N/cm. The crack used in the model was the observed experimental static "pop-in" crack length (Table 7). A typical plot of the radial stress field in the bend region is shown in Figure 56. In reference to all cracks in the skin-stiffener model, crack front #1 is the lower crack tip extending toward the stiffener flange tip. Crack front #2 is the crack tip extending toward the stiffener web section. FEA results for G_I and G_{II} at the critical load for crack growth are compared with experimental G_I and G_{II} from DCB and ENF tests in Table 11. The cracks in the skin-stiffener are mixed-mode, with both G_I and G_{II} components. The values of G_I and G_{II} calculated by FEA for the skin-stiffener delamination crack at the load which produced crack growth are far below the G_{Ic} and G_{IIc} values from the DCB and ENF tests for the same ply interface.

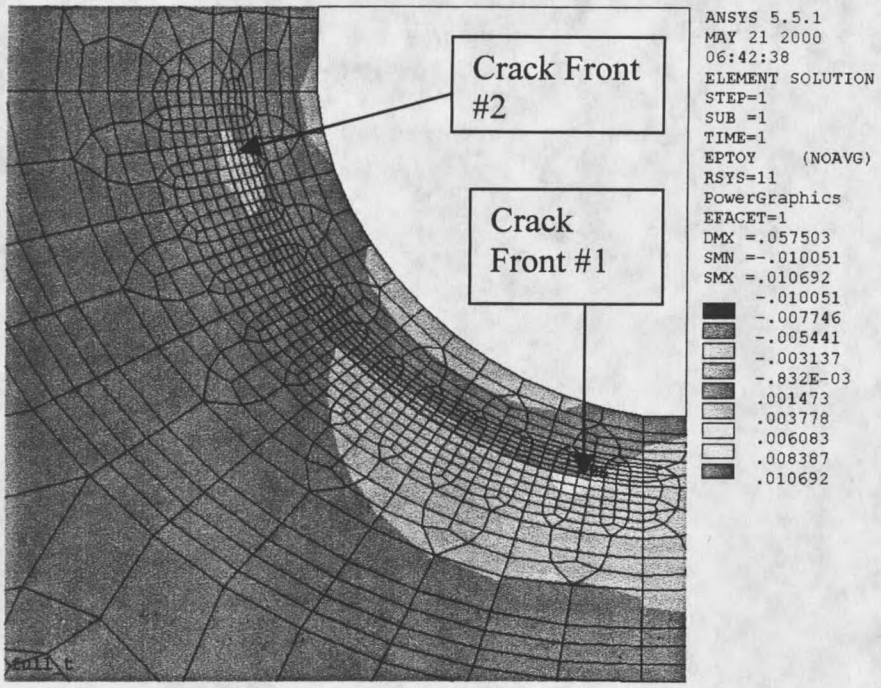


Figure 56. FEA Tangential Strain Plot with Crack Front Locations

To rationalize the apparently very low G values for the skin-stiffener, the use of a mixed-mode criterion for crack growth has been investigated. The skin-stiffener G values shown in Table 11 were inserted into Equation 20 using exponents of 1 (m = n = 2) and ½ (m = n = 1) to determine (F). For crack growth to occur, recall that the sum of the two ratios (F) must be greater than or equal to one.

DCB and ENF Tests		Skin-Stiffener by Ansys FEA	
G_I (J/m^2)	G_{II} (J/m^2)	G_I (J/m^2)	G_{II} (J/m^2)
341.8	941.3	143.1	101.4

Table 11. Strain Energies for 128.6 N/cm Load and 2.48mm crack in Bend Region of Skin-stiffener

Before the mode interaction equation could be used to predict the critical load, G had to be confirmed to vary as a function of P^2 following theoretical expectations [9]. The model was incrementally loaded using 3 load steps of 44, 61 and 79 N/cm. The strain energies (G_I and G_{II}) at crack front #2 and applied loads were parsed from the FEA result file. G versus load is shown in Figure 57.

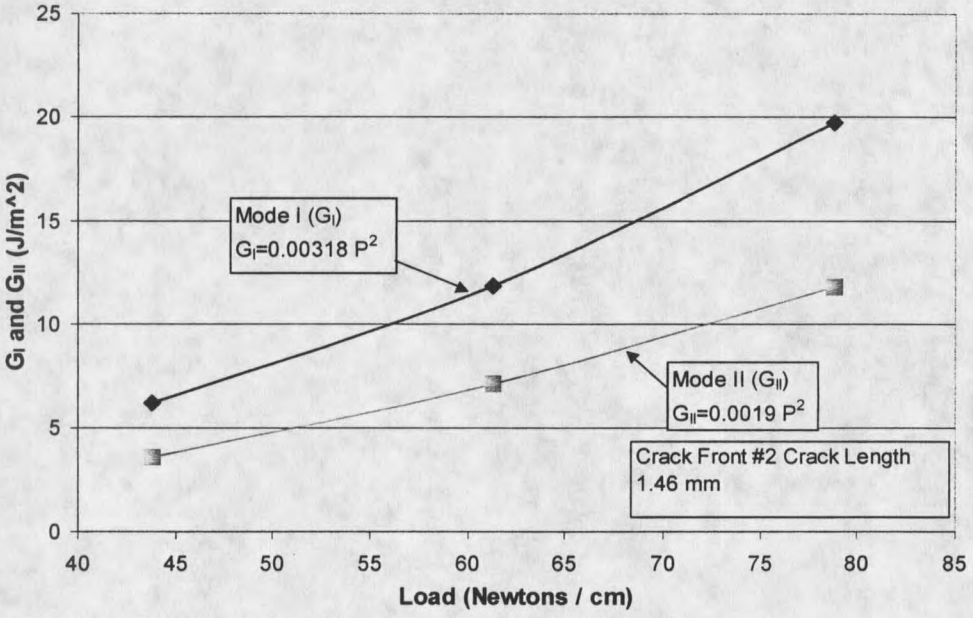


Figure 57. G_I and G_{II} versus Applied Load, Skin-Stiffener Geometry

The assumed variation of G_I and G_{II} with P^2 for a specified crack length fit the FEA results accurately (R=1.0 and 1.0 for mode I and II respectively using the transformed regression method). This demonstrates that a crack model could be run with an arbitrary applied load (P_{model}), and G values could then be determined using the mode

interaction criterion previously described in Chapter 2 (Equation 20). The interaction sum (F) then could be used to scale the load applied to the model (P_{model}) to determine the critical load (P_{cr}) that will propagate the crack. The sequence of events used in determining the critical static load that initiates crack growth for the skin-stiffener is shown in Figure 58 (represented here in terms of a "design" sequence).

Using ratio exponents of 1 and ½, the interaction sums (F) were 0.56 and 0.98 respectively, shown in Table 12. This resulted in predicted crack propagation loads of 172.6 and 130.2 N/cm respectively. The analysis showed that exponents of ½ seem to correlate well with the experimental data. A difference of 1.2% from the experimental critical propagation load of 128.6 N/cm was obtained with ratio exponents of ½ (m = n = 1) compared to a difference of 34.2% with ratio exponents of 1 (m = n = 2).

Recall from elementary fracture mechanics that G varies with square of K. Recall that K is the stress intensity factor. This very important parameter or factor describes all the crack tip stresses for elastic solutions. Since K varies with the square root of G, an interesting point is that since interaction exponents of ½ best correlate with experimental data, the interaction varies linearly with K.

Skin-Siffener Fatigue Comparison

The same skin-stiffener model was used to predict behavior for the fatigue loading tests. Experimental observations showed that delaminations occurred in the (90°/45°) interface. The non-symmetric model was analyzed with various crack lengths

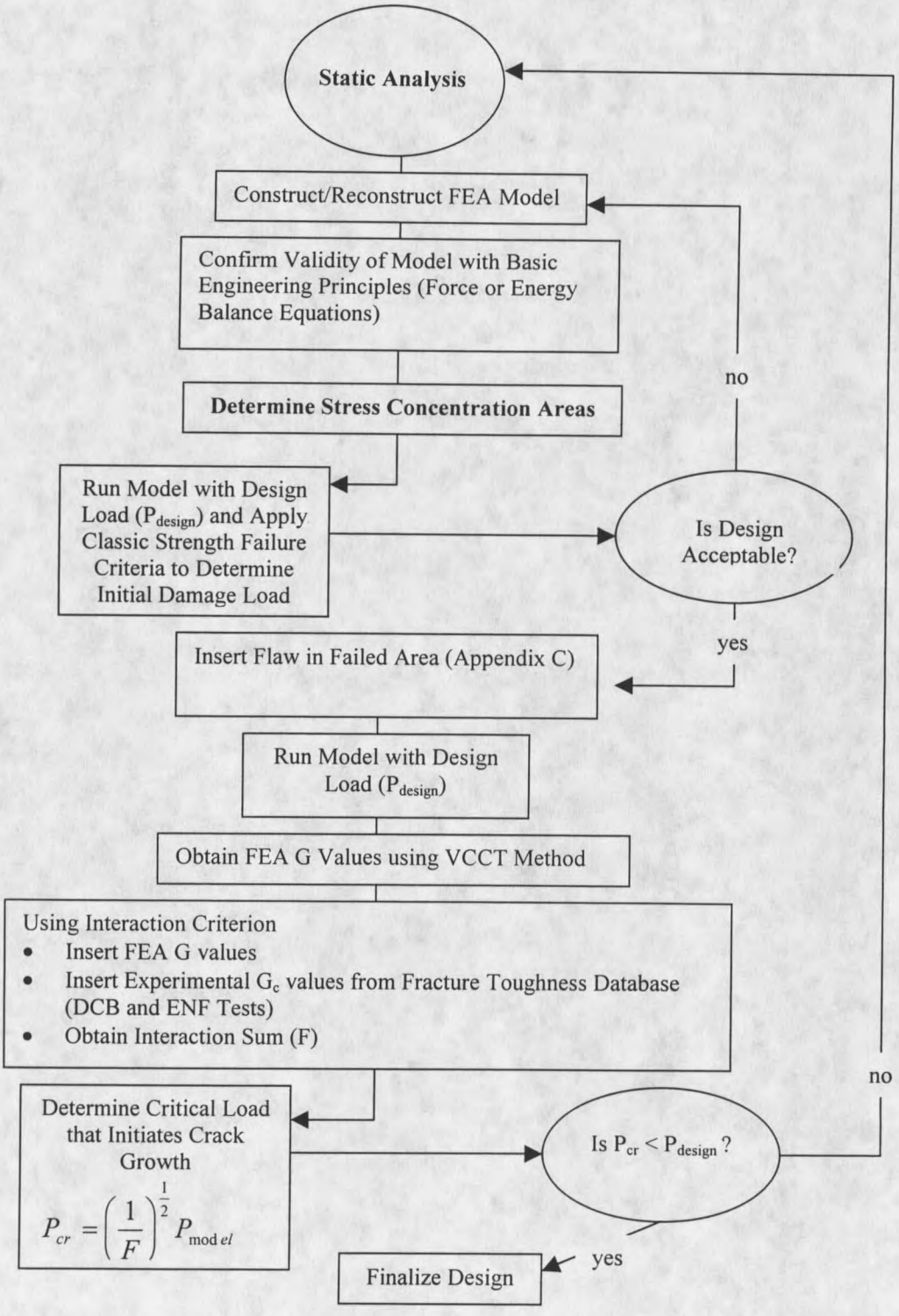


Figure 58 Sequence of Events for Static Analysis of Skin-Stiffener

Empirical from DCB and ENF Tests		Numerical Ansys		Experimental Critical	F Linear Exponent	Predicted Critical	F 1/2 Exponent	Predicted Critical
G_{Ic} (J/m^2)	G_{IIc} (J/m^2)	G_I (J/m^2)	G_{II} (J/m^2)	Load (N/cm)	Ratios (m=n=2)	Load (N/cm)	Ratios (m=n=1)	Load (N/cm)
341.8	941.3	143.1	101.4	128.6	0.56	172.6	0.98	130.2

Table 12. G Values, Interaction Sums and Predicted Critical Loads for the FEA Skin-Stiffener Model

to investigate the mode interaction as crack front #2 propagated toward the web. Crack lengths in the fatigue model were varied from 1.2 mm to 9.0 mm to determine mode interactions for various crack lengths in the bend region. A plot of G versus crack length for crack front #2 is shown in Figure 59. G_I varied from 55% to 99% of the total G (G_T) for crack lengths from 1.2 mm to 9.5 mm as shown in Figure 60. The crack front becomes mode I dominated as the crack progresses around the bend region toward the web of the stiffener.

A similar methodology to that used to predict critical static loads was used to determine the cyclic crack growth rate of the skin-stiffeners at a specified load level. Three specific experimental cases were investigated that were run at various load levels resulting in various crack growth rates (da/dN). The experimental skin-stiffener specimens were 9T9 and 10T3. The average crack length, DCB and ENF experimental G_I and G_{II}, and FEA G_I and G_{II} are shown in Table 13.

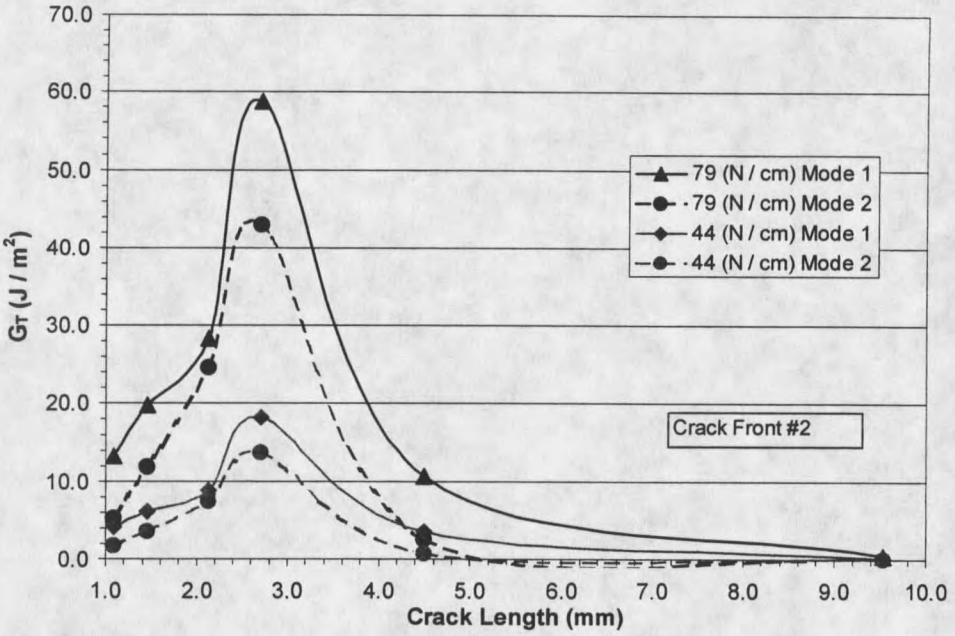


Figure 59. G_T versus Crack Length for Crack Front #2

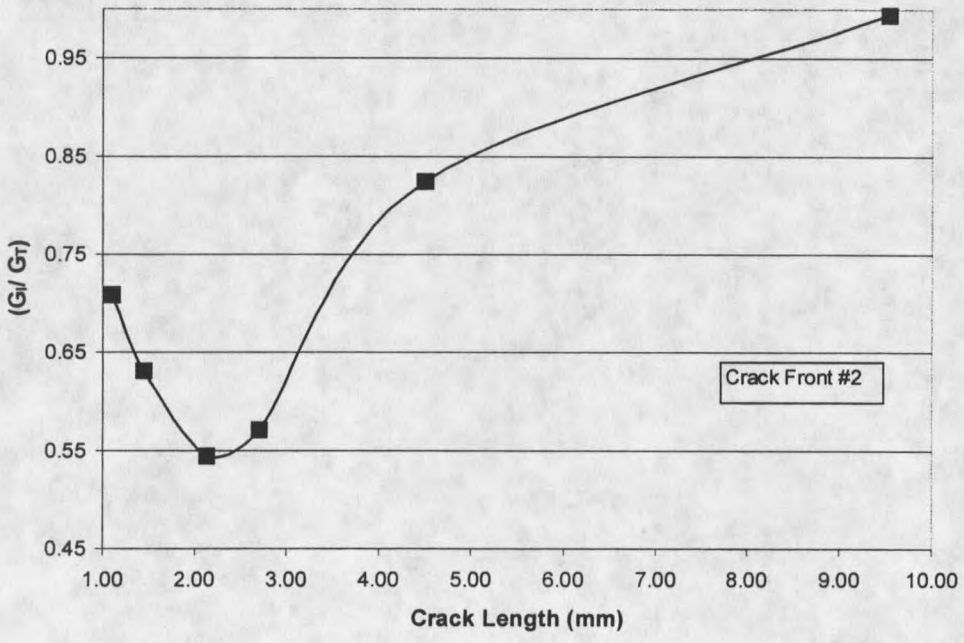


Figure 60. Normalized G_I/G_T versus Crack Length for Crack Front #2 in Bend Region

Specimen	Crack Growth Rate (da/dN)	Crack Length	Corresponding GI and GII from DCB and ENF Data at given (da/dN)		Skin-Stiffener Calculated G_I and G_{II} from FEA	
			G_I	G_{II}	G_I	G_{II}
	(mm/cycle)	(mm)	(J/m^2)	(J/m^2)	(J/m^2)	(J/m^2)
9T9	$8.09x10^{-7}$	2.4	62.9	119	25	20.3
10T3	$9.47x10^{-5}$	2.8	113.8	289.3	58.5	42.5
10T3	$6.31x10^{-5}$	2.9	107.9	268.2	54	38.3

Table 13. Strain Energies and Crack Length for DCB and ENF Crack Growth Compared with Skin-Stiffener Values at the Same Crack Growth Rate

The DCB and ENF G values were obtained from the inverse of the power law curve-fit equation 28 (Figures 36 and 40) relating G and (da/dN) for the DCB and ENF specimens. In Equation 20, if the sum of the two ratios (F) is equal to one, it is assumed that crack growth will occur at the chosen rate (da/dN). Since G is proportional to P^2, the load can be scaled by (F) to obtain the predicted load for the selected growth. Ratio sums (F), predicted load, crack length, crack growth rate and experimental load are presented in Table 14.

Sample	Crack Length (mm)	(da/dN) (mm/cycle)	Ratio Sum (F)		Experimental Load (N/cm)	Predicted Load (m,n=1/2) (N/cm)	Percent Error (%)
			m,n=1	m,n=1/2			
9T9	2.4	8.09×10^{-7}	0.57	1.04	61.3	60.1	2.0
10T3	2.8	9.47×10^{-5}	0.66	1.09	78.8	75.5	4.2
10T3	2.9	6.31×10^{-5}	0.64	1.10	78.8	75.1	4.6

Table 14. Experimental and Predicted Loads for Different Crack Growth Rates in Bend Region of Cyclic Loaded Skin-stiffeners

When the normalized G_I and G_{II} components of the skin-stiffener are compared to the individual mode tests (DCB and ENF), the Mode II G components (Figure 61) possess similar slopes but very different G_{II} values. The Mode I G component (Figure 62) of the stiffener gives approximately half the exponent of the DCB Mode I test but the G_I values are closer together than the G_{II} values. It is believed that these discrepancies are due to geometric effects since the stiffener crack is in the bend region. The results appear to suggest that the crack in the skin-stiffener may grow in mode II (same exponent), but at a greatly reduced G_{II} level due to the mode I contribution. The interaction term (F) which correlates the data best is ½ (m = n = 1), the same as for the static case.

The sequence used in determining the critical fatigue load that produces a particular value of crack growth rate in the skin-stiffener is shown in Figure 63, again cast in terms of design. The overall lifetime would then require integration of the crack growth rate as the crack extends to failure in a particular geometry. For example, a growth rate of 10^{-6} mm/cycle would produce a 2 mm long delamination in $2x10^6$ cycles if the G values remained constant as the crack grew, which is in approximate agreement with Figure 63.

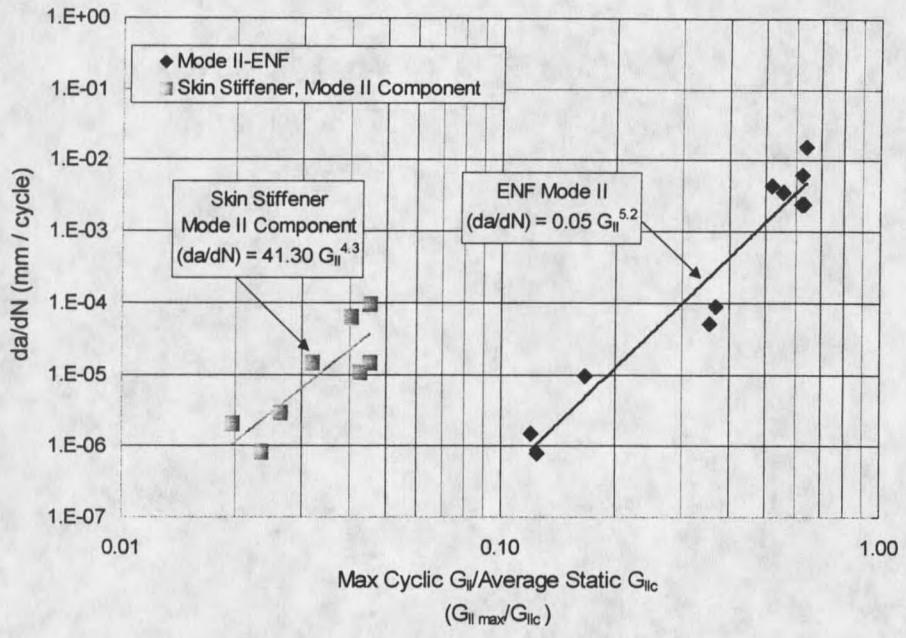


Figure 61. (da/dN) versus (Maximum Cyclic Strain Energy/Average Static Strain Energy), Ortho-polyester Skin-Stiffener Specimens and ENF Specimens

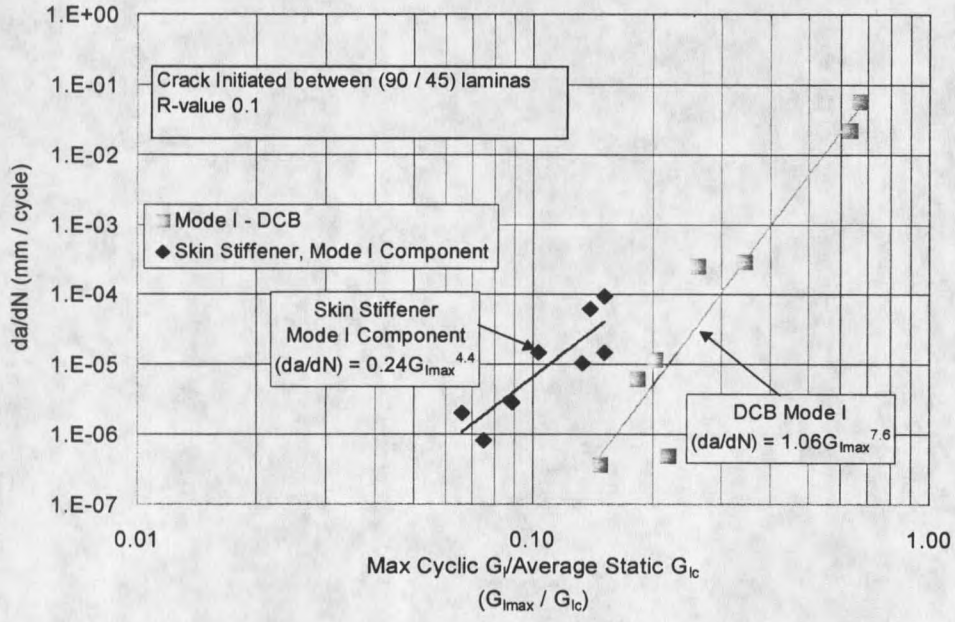


Figure 62. (da/dN) versus (Maximum Cyclic Strain Energy/Average Static Strain Energy), Ortho-polyester Skin-Stiffener Specimens and DCB Specimens

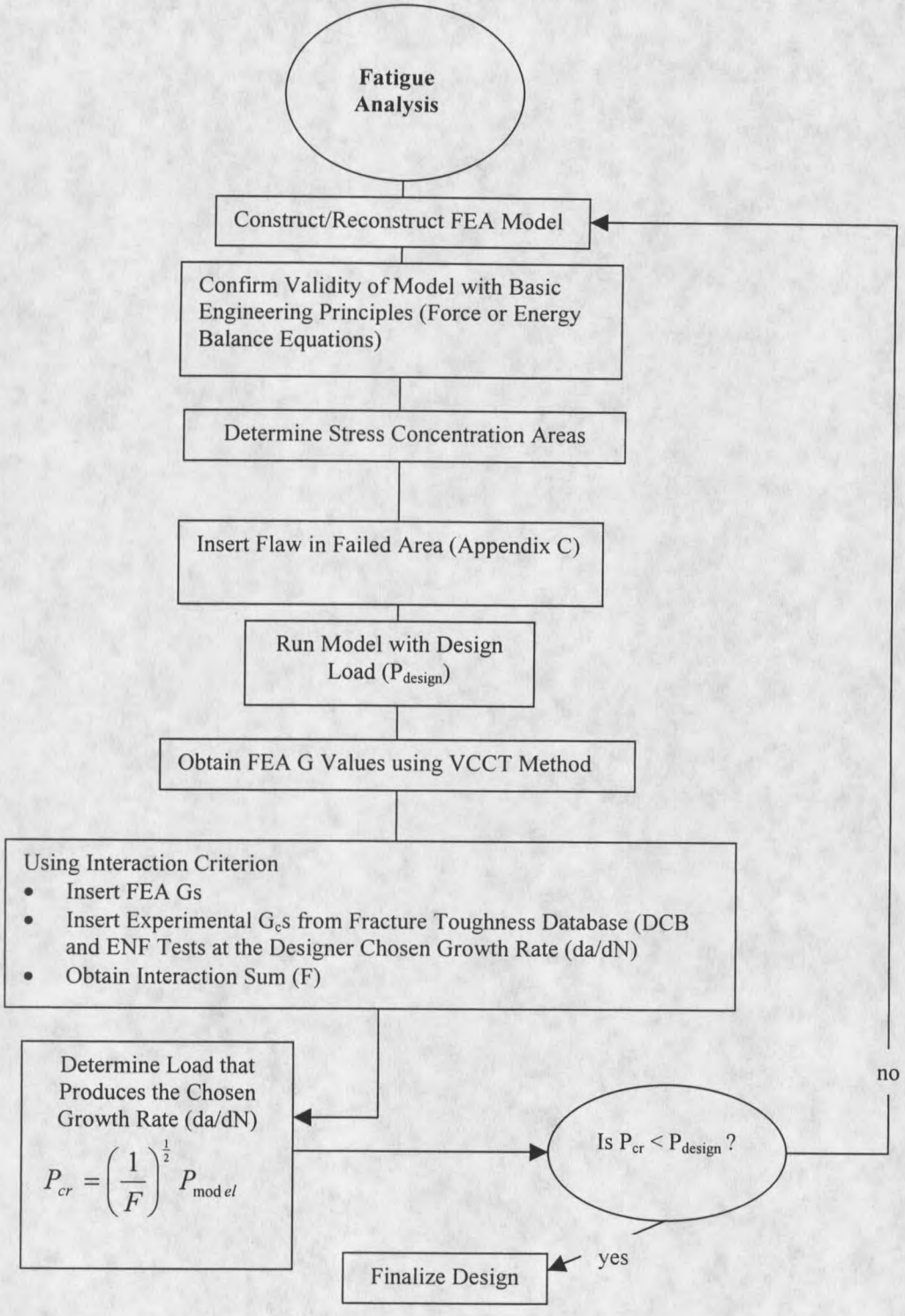


Figure 63. Sequence of Events for Fatigue Crack Growth Analysis

Use of Methodology in Design

The following procedures are illustrated to give the reader an understanding of the experimental tests and analysis that should be performed on a fiber-reinforced structure under static and cyclic loading conditions that have been investigated in this thesis.

Static Analysis

Experimental Testing:

- Obtain material and engineering properties for the fiber-reinforced composite used in the structure.
- Perform Mode I test to obtain G_{Ic} versus Crack Length (if material possesses R-curve effects) relation for the specific fiber-reinforced composite material.
- Perform Mode II test to obtain G_{IIc} fracture toughness.

Analysis:

- Build FEA model with boundary conditions representative of actual structure being analyzed.
- Run model to locate high stress gradient areas.
- Analyze model using classic failure criteria to determine the load at which structure will begin to fail.
- Insert delamination or crack at the failed region in the FEA model. An initial crack length can be determined by setting F = 1, the predicted load as initial experimental damage "pop-in" load and using curve-fitted relations for G_I and G_{II} versus crack length for the substructure (Figure 59). A detailed initial crack length prediction is enclosed in Appendix C.

- Apply operating load to the structure with damage.
- Determine the Mode I and II G values at the crack fronts in the model.
- If the crack possesses Mode I or II only, the FEA model G can be directly compared to the experimental G_c value. If $G > G_c$, the crack front will advance.
- If the crack is mixed-mode, then a mixed-mode criterion must be used to determine if the crack front will advance.

Refer to Appendix B Part A for a sample calculation to determine critical load for crack growth.

Fatigue Analysis

Experimental Testing:

- Obtain complete material and engineering properties for the fiber-reinforced composite used in the structure.
- Perform cyclic Mode I test to obtain da/dN versus G_{Imax} relationship (power law relationship) for the specific fiber-reinforced composite material. To ensure conservative G values, the tests should be performed using short crack lengths to reduce R-curve effects.
- Perform cyclic Mode II test to obtain da/dN versus G_{IIc} relationship. These tests should also be performed using short crack lengths as discussed previously.

Analysis:

- Build FEA model with boundary conditions representative of actual structure being analyzed.
- Run model to local high stress gradient areas.
- Insert a delamination or crack in the highest stress area.
- Apply the maximum cyclic design load to the FEA model.
- Determine the Mode I and II G values at the crack fronts in the model.
- If the crack possesses Mode I or II Gs only, the FEA G can be directly compared to the experimental G_{max}. From the experimental database power law relationship the growth rate of the crack can be determined.
- If the crack is mixed-mode, then a mixed-mode criterion ($m = n = ½$ best fit the experimental data in this thesis) must be used to determine if the crack front will advance.

Refer to Appendix B Part B for a sample calculation to determine load at a specified crack growth rate.

CHAPTER 7

SUMMARY, CONCLUSIONS AND RECOMMENDATIONS

A summary of the experimental and numerical results is presented in this chapter. Recommendations for stiffener analysis and design methodology are based upon these results.

Experimental Summary and Conclusions

DCB and ENF Specimens

- The static Mode I G_{Ic} for the (90°/45°) and (45°/45°) interface double cantilever beam (DCB) specimens showed toughness increases with crack extension (R-curve behavior). This was due to fiber bridging and tow debonding.
- The fatigue Mode I G_I for the (90°/45°) interface DCB specimens also showed toughness increases with crack extension due to fiber bridging and tow debonding. As a result, short crack growth extensions were used to characterize fatigue crack growth and establish a crack growth curve.
- Fracture toughness values for the (90°/45°) interface static Mode II G_{IIc} growth from end notch flexure (ENF) testing were approximately four times greater than Mode I G_{Ic} values.
- Static Mode II ENF specimens with (90°/45°) interface cracks grew in a stable manner for several millimeters due to crack branching or multiple crack fronts and tow debonding.

- Mode II fatigue crack growth also showed toughness increases with crack extension due to multiple crack fronts and tow debonding. A mode II fatigue crack growth curve was established using short crack extensions as with mode I.
- The mode I and II fatigue crack growth exponents were 7.62 and 5.15 respectively.

Skin-Stiffener Specimens

- Static tests on Ortho-polyester matrix skin-stiffeners show that damage initiated in the web-flange transition bend region during tensile pull-off loading. These cracks grew in the (90°/45°) interface. Transverse cracking then occurred through the 90° flange plies. The delaminations grew toward the web centerline and flange-skin interface. Delamination continued toward the flange tip and web centerline until ultimate failure occurred.
- Stiffeners made with tougher resins showed large increases in static initial damage and ultimate loads since delamination resistance is dominated by the toughness and strength of the matrix material.
- Toughened vinylester resin skin-stiffeners were most resistant to damage and ultimate failure under both tensile and fatigue loading, but the normalized strength decreased more rapidly in fatigue than for more brittle matrix systems.

Numerical Techniques and Correlations with Experimental Results

- The Virtual Crack Closure Technique (VCCT) determined G_I predictions typically agreed with the Modified Beam Theory (MBT) values for both static and fatigue loading of DCB test specimens.

- Using FEA analysis for skin-stiffeners, the maximum strain criterion conservatively predicted the initial damage load within 12% of experimental loads.
- FEA calculated G_{Ic} and G_{IIc} values at crack growth in skin-stiffened specimens were far below G_{Ic} and G_{IIc} values found from DCB and ENF tests. An interactive failure criterion with $m = n = ½$ provided a good correlation of skin-stiffener results with ENF and DCB data (1.2% error in load prediction).
- An interactive failure criterion with $m = n = ½$ also correlated the fatigue crack growth rate data between the skin-stiffener specimens and the DCB and ENF specimens. Thus F, the interaction sum, varies linearly with K, the stress intensity factor.
- A methodology for static and fatigue strength prediction of complex substructures like the skin-stiffener geometry has been presented.

Future Work

- Further research is required in the area of mixed-mode static and fatigue fracture for this class of composites. This might include both mixed mode bending tests and other complex geometries of interest in specific applications. These could be modeled with the FEA VCCT method.
- An initial investigation was performed using toughened resins in skin-stiffeners. An in-depth fatigue/toughness study should be performed to justify the use of a polyester or vinylester matrix. Since the 8084 vinylester operated at much higher load levels, it would be of great interest for further study.

REFERENCES CITED

1. Spera, David, A., "Wind Turbine Technology Fundamental Concepts of Wind Turbine Engineering", ASME Press, 1994, pp. 207.

2. Skramsted, Jon, D., "Evaluation of Hand Layup and Resin Transfer Molding in Composite Wind Turbine Manufacturing", *Master's Thesis in Mechanical Engineering, Montana State University-Bozeman,* August 1999.

3. Mandell, J.F., Samborsky, D.D., "DOE/MSU Composite Material Fatigue Database: Test Methods, Materials, and Analysis," *Sandia National Laboratories Contractor Report, SAND97-3002.* December 1997.

4. A&E Documentary, "The Comet", 1989.

5. Haugen, Darrin, J., "Fracture of Skin-Stiffener Intersections in Composite Wind Turbine Blade Structures", *Master's Thesis in Mechanical Engineering, Montana State University-Bozeman,* August 1998.

6. Hyer, Michael, W., "Stress Analysis of Fiber-Reinforced Composite Materials", McGraw Hill Publishers, 1998.

7. Cairns, Douglas, S., Montana State University, Personal Interviews, 1999.

8. Jones, Robert M., "Mechanics of Composite Materials", 2nd Edition, Taylor and Francis, Inc., 1999.

9. Broek, D., "Elementary Engineering Fracture Mechanics," *4th Edition,* Kluwer Academic Publishers, 1986.

10. Russell, A.J., Street, K.N., "Moisture and Temperature Effects on the Mixed –Mode Delamination Fracture of Unidirectional Graphite/Epoxy," *Delamination and Debonding of Materials*, ASTM STP 876, W. S. Johnson, Ed., American Society for Testing and Materials, Philadelphia, 1985, pp. 349-370.

11. Reeder, J.R., "A Bilinear Failure Criterion for Mixed-Mode Delamination," *Composite Materials: Testing and Design (Eleventh Volume),* ASTM STP 1206, E. T. Camponeschi, Jr., Ed., American Society for Testing and Materials, Philadelphia, 1993, pp. 303-322.

12. Russell, A.J., Street, K.N., "Factors Affecting the Interlaminar Fracture Energy of Graphite/Epoxy Laminates", *Proceedings, Fourth International Conference on Composite Materials*, Japan Society for Composite Materials, 1982, pp. 279.

13. Crews, J.H., Jr. and J.R.Reeder. "A Mixed-Mode Bending Apparatus for Delamination Testing", NASA TM 100662, August 1988.

14. Reeder, J.R. and J.H.Crews, Jr. "Redesign of the Mixed-Mode Bending Test for Delamination Toughness", *Composites Design, Manufacture and Application, ICCM/8 Conference Proceedings*, SAMPLE, S.W. Tsai and G.S. Springer, eds., July 1991, pp. 36-1-36-B-10.

15. Reeder, J.R., Crews, J.H. Jr., "Mixed Mode Bending Method for Delamination Testing," *AIAA Journal,* 1990, pp. 1270-1276.

16. Rybicki, E.F., Kanninen, M.F., "A Finite Element Calculation of Stress Intensity Factors by a Modified Crack Closure Integral", *Engineering Fracture Mechanics*, Vol. 9, 1977, pp. 931-938.

17. Raju, I.S., "Simple Formulas for Strain-Energy Release Rates with Higher Order and Singular Finite Elements," *NASA Contractor Report 178186*, December 1986.

18. "Standard Test Method for Mode I Interlaminar Fracture Toughness of Unidirectional Fiber-Reinforced Polymer Matrix Composites, D 5528 – 94a", *1997 Annual Book of ASTM Standards*, Vol. 15.03, 1997, pp.271-279.

19. Russel, A.J. and Street, K.N., "The Effect of Matrix Toughness on Delamination: Static and Fatigue Fracture under Mode II Shear Loading of Graphite Fiber Composites," *Toughened Composites*, ASTM STP 937, N.J. Johnston, Ed., ASTM, Philadelphia (1987), pp 275.

20. Konig, M., Kruger, R., Kussmaul, K., Von Alberti, M., Gadke, M., "Characterizing Static and Fatigue Interlaminar Fracture Behavior of a First Generation Graphite/Epoxy Composite,: *13th Composite Materials: Testing and Design, Thirteenth Volume*, ASTM STP 1242, S.J. Hooper, Ed., American Society for Testing and Materials, 1997, pp. 60-81.

21. Mandell, J.F., Tsai, J.Y., "Effects of Porosity on Delamination of Resin-Matrix Composites", *Flight Dynamics Laboratory Contractor Report*, April 1990.

22. Kenane, M., and Benzeggagh, M.L., "Mixed-Mode Delamination Fracture Toughness of Unidirectional Glass/Epoxy Composites Under Fatigue Loading", *Composites Science and Technology*, Volume 57, 1997, pp.597-605.

23. "Volume I, Procedures, Chapter 3 Structural Analysis, Section 3.9 Fracture Mechanics," *ANSYS User's Manual,* pp. 3-163.

24. Alif, N., Carlsson, L.A., Gillespie, J.W., "Mode I, Mode II, and Mixed Mode Interlaminar Fracture of Woven Fabric Carbon/Epoxy," Composite *Materials: Testing and Design, Thirteenth Volume*, ASTM STP 1242, S.J. Hooper, Ed., American Society for Testing and Materials, 1997, pp. 82-106.

25. Davidson, B. D., Kruger, R., Konig, M., "Effect of Stacking Sequence on Energy Releae Rate Distributions in Multidirectional DCB and ENF Specimens," Engineering Fracture Mechanics, Vol 55, No. 4, 1996, pp. 557-569.

26. "Standard Test Method for Plane-Strain Fracture Toughness of Metallic Materials, ASTM E399", 1996 Annual Book of ASTM Standards, Vol. 3.01, 1996, pp 407-437.

27. Bradley, W.L., "Chapter 5, Relationship of Matrix Toughness to Interlaminar Fracture Toughness," *Application of Fracture Mechanics to Composite Materials*, K. Friedrich, Ed., 1989, pp. 159-187.

28. Oerzco, Ricardo, "Effects of Toughened Matrix Resins on Composite Materials for Wind Turbine Blades", Master's Thesis in Mechanical Engineering, Montana State University-Bozeman, July 1999.

29. Li, Mei, "Temperature and Moisture Effects on Composite Materials for Wind Turbine Blades", Master's Thesis in Mechanical Engineering, Montana State University-Bozeman, July 1999.

30. Wang, J.T., Raju, I.S., Sleight, D.W., "Composite Skin-Stiffener Debond Analyses Using Fracture Mechanics Approach with Shell Elements," *Composites Engineering*, Vol. 5, No. 3, 1995, pp. 277-296.

31. Raju, I.S., Sistla, R., Krishnamurthy, T., "Fracture Mechanics Analyses for Skin-Stiffener Debonding," *Engineering Fracture Mechanics*, Vol. 54, No. 3, 1996, pp. 371-385.

32. Wang, J.T., Raju, I.S., "Strain Energy Release Rate Formulae for Skin-Stiffener Debond Modeled with Plate Elements", Engineering Fracture Mechanics, Vol 54, No 2, 1996, pp. 211-228.

33. Raju, I.S., Shivakumar, K.N., and Crews, Jr., J.H., "Three-Dimensional Elastic Analysis of a Double Cantilever Beam Specimen", AIAA Journal 26, 1988, pp. 1493-1498.

APPENDIX A

TEST RESULTS

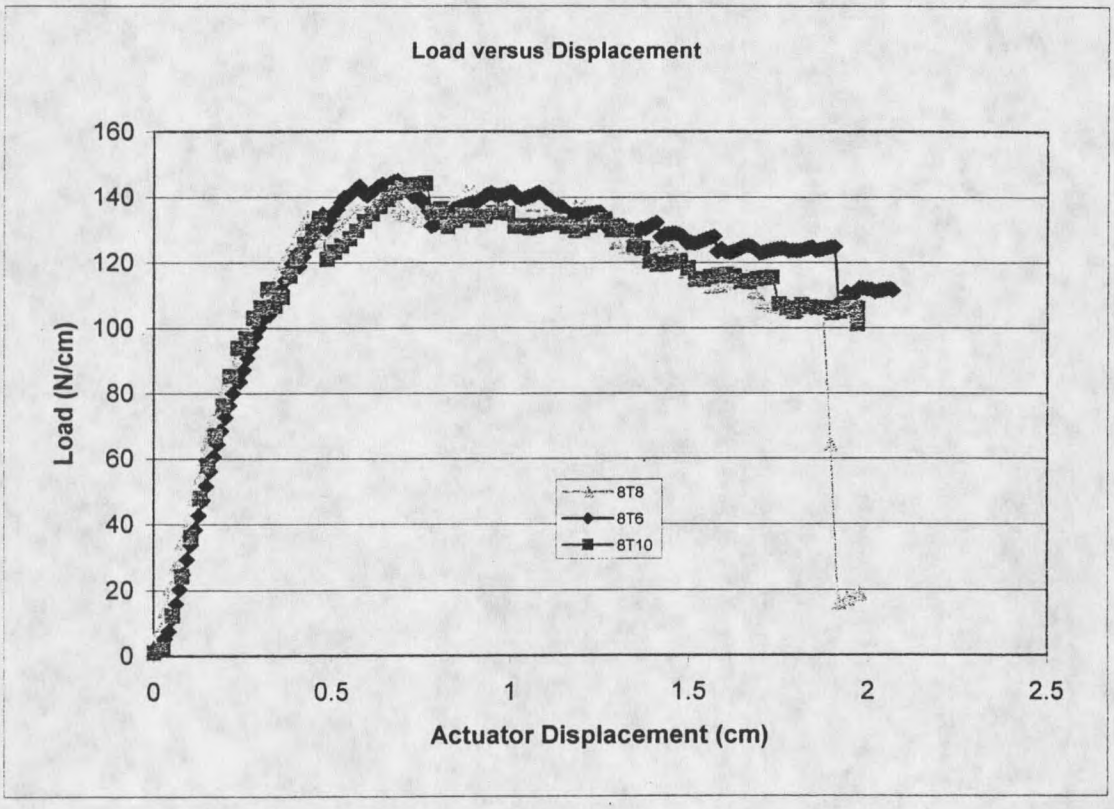
Ortho-Polyester Skin-Stiffener
Static Crack Growth Tests

Specimen	"Pop-in" Load (load that initiated cracking in bend region) (N / cm)	Initial Crack (crack resulting from "Pop-in" Load) (mm)	Critical Load (load at which growth in initial crack occurred) (N / cm)	Final Crack (length of crack after critical load applied) (mm)	Average Crack (average of initial and final crack lengths) (mm)
18T2	see note(a)	2.3	129.1	3.4	2.9
18T4	89.3	1.9	134.8	2.8	2.4
18T5	85.8	1.9	119.1	2.8	2.4
18T6	99.8	1.8	134.8	2.6	2.2
18T3	99.8	1.9	133.1	2.8	2.4
18T10	99.8	2.0	120.8	3.5	2.8
Average	94.9	2.0	128.6	3.0	2.5
Stand. Dev.	6.8	0.1	7.9	0.3	0.2

(a) no initial damage load obtained

Ortho-Polyester
Static Test Specimens

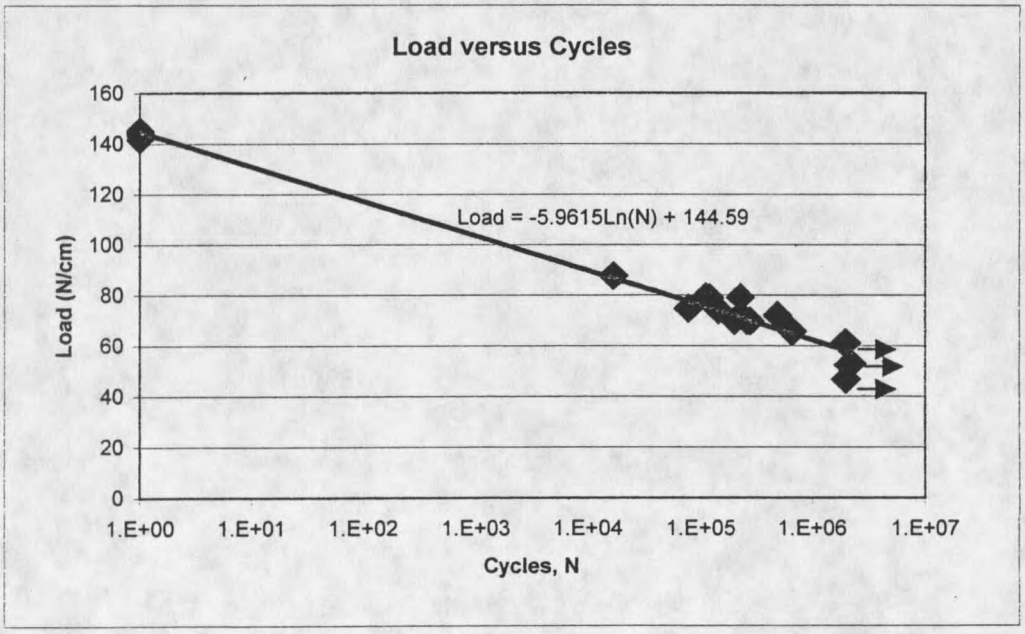
specimen	width (mm)	Load at Initital Damage (N)	Displacement at Initial Damage (mm)	Maximum Load (N/cm)	Displacement at Maximum Load (mm)
8T6	24.1	83.3	2.0	145.0	6.8
8T8	24.1	83.9	2.3	142.0	9
8T10	24.1	93.8	2.3	144.0	7.6
average	24.1	87.0	2.2	143.0	7.8
Stand. Deviation	0.0	5.9	0.2	1.4	1.1



Ortho-Polyester
Fatigue Test Specimens

specimen	width (mm)	load level (maximum cyclic load) (N/cm)	Normalized Load (max. cyclic load/ avg. max. static load) (Cyclic/Monotonic)	cycles (cycles to failure failure when max. disp. = 0.43cm)	
10T12	24.9	46.6	0.32	1999047	runout
10T7	24.9	52.3	0.36	2114649	runout
8T9	23.9	52.9	0.37	2216888	runout
8T14	24.4	61.1	0.42	1987449	runout
9T9	23.9	61.1	0.42	1949129	runout
10T11	24.6	72.0	0.50	487960	
10T4	24.4	65.6	0.46	651491	
10T8	24.9	65.7	0.46	658000	
8T4	24.4	69.6	0.48	278040	
8T5	24.4	69.8	0.49	257160	
8T13	24.4	69.8	0.49	198600	
9T10	23.9	74.7	0.52	77642	
9T1	24.1	74.1	0.52	142897	
8T7	24.1	78.8	0.55	118855	
8T12	23.9	78.9	0.55	225934	
8T11	24.1	79.2	0.55	110102	
10T5	24.4	87.7	0.61	16809	
average	24.2	76.6	0.53		
Stand. Deviation	0.2	5.9	0.04		

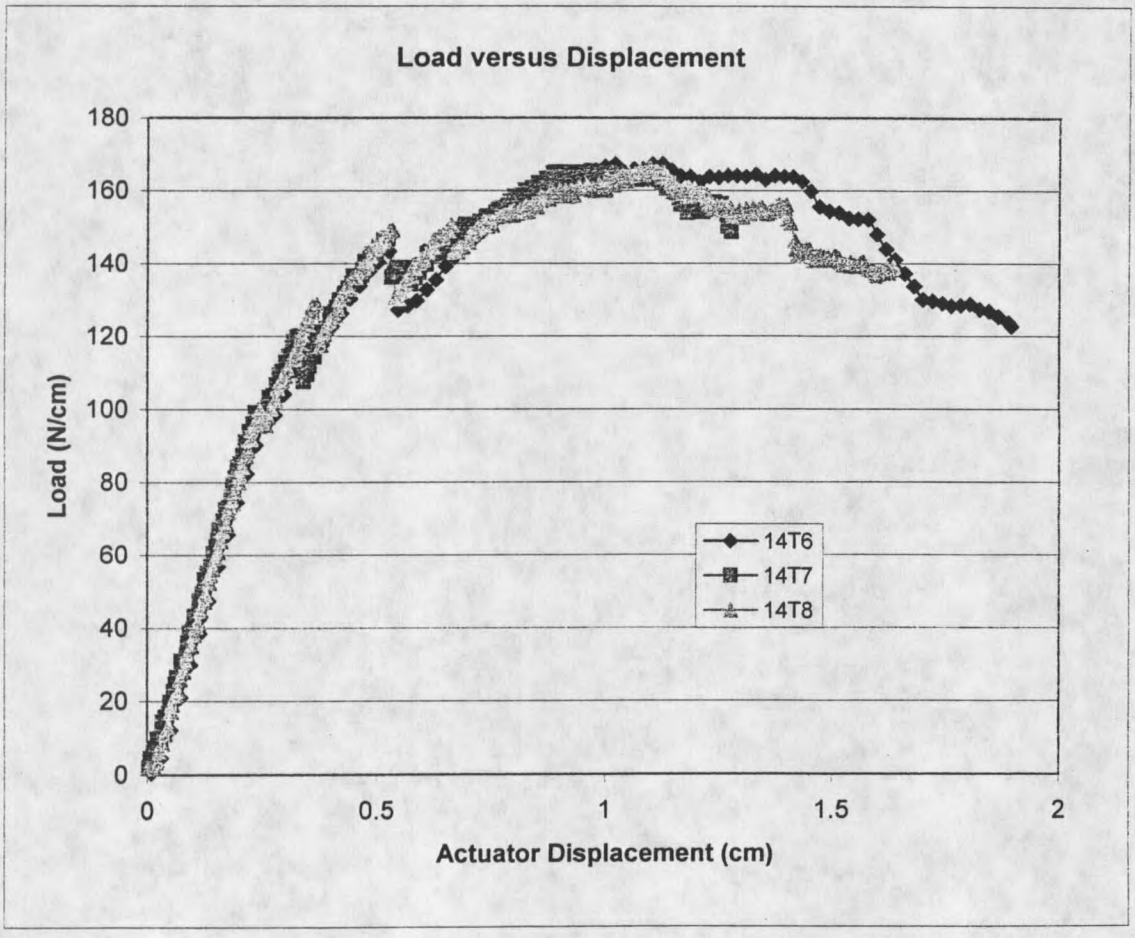
R Value = 0.1



Iso-Polyester

Static Test Specimens

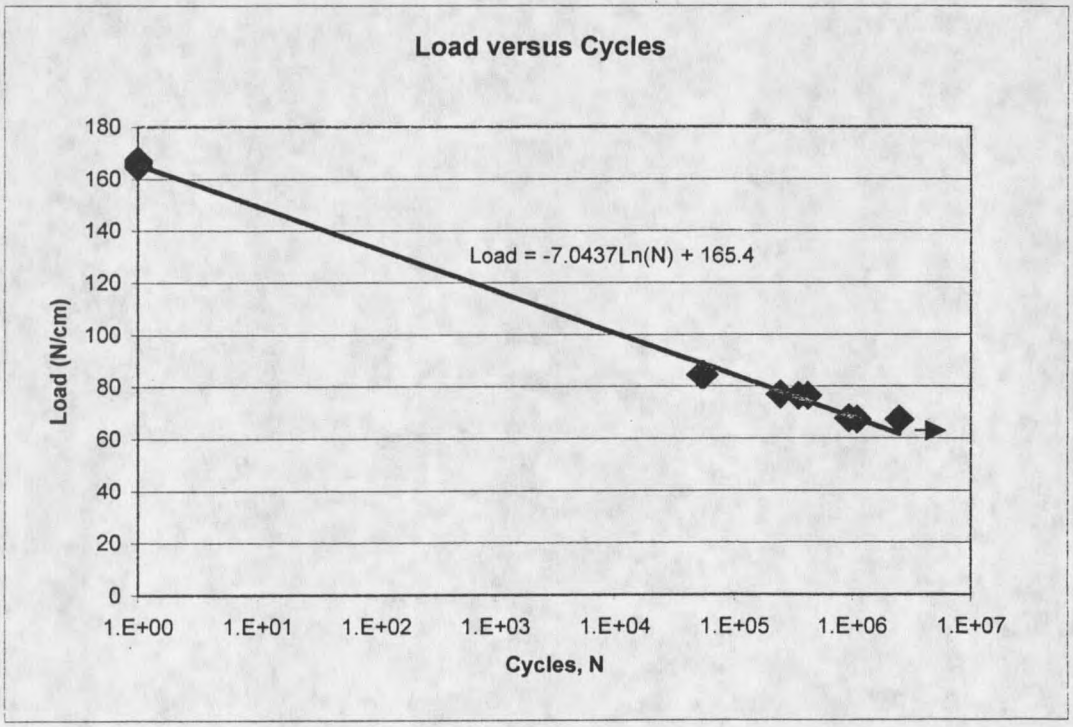
specimen	width (mm)	Load at Initital Damage (N)	Displacement at Initial Damage (mm)	Maximum Load (N/cm)	Displacement at Maximum Load (mm)
14T6	22.6	95.7	2.6	167.2	1
14T7	22.8	99.1	2.3	164.9	0.9
14T8	22.9	99.7	2.4	166.2	1.1
average	22.8	98.2	2.4	166.1	1.0
Stand. Deviation	0.2	2.2	0.1	1.2	0.1



Iso-Polyester
Fatigue Test Specimens

specimen	width (mm)	load level (maximum cyclic load) (N/cm)	Normalized Load (max. cyclic load/ avg. max. static load) (Cyclic/Monotonic)	cycles (cycles to failure failure when max. disp. = 0.43cm)	
14T13	23.1	84.4	0.51	52444	
14T12	23.1	84.4	0.51	54870	
14T4	23.1	76.3	0.46	422760	
14T5	23.1	76.9	0.46	244840	
14T1	22.4	76.4	0.46	349160	
14T3	25.4	67.2	0.40	2511234	runout
14T10	25.4	67.2	0.40	1096320	
14T9	23.1	67.7	0.41	934200	
average	23.6	75.1	0.45		
Stand. Deviation	1.1	7.2	0.04		

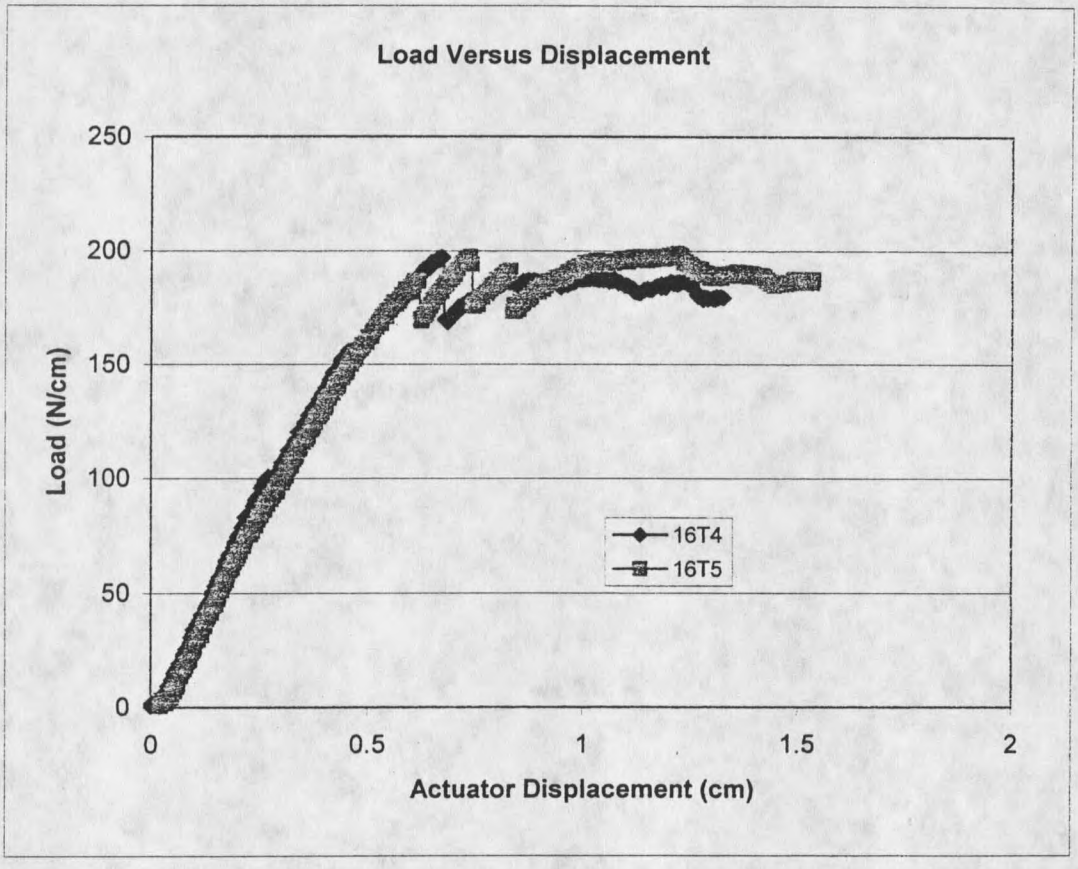
R Value = 0.1



411 Vinylester

Static Test Skin-Stiffener Specimens

specimen	width (mm)	Load at Initital Damage (N)	Displacement at Initial Damage (mm)	Maximum Load (N/cm)	Displacement at Maximum Load (mm)
16T4	22.6	100.9	2.7	197.6	6.7
16T5	22.8	186.8	6.2	199	7.3
Average	22.7	143.9	4.4	198.3	7.0
Stand. Deviation	0.1	60.7	2.4	1.0	0.4

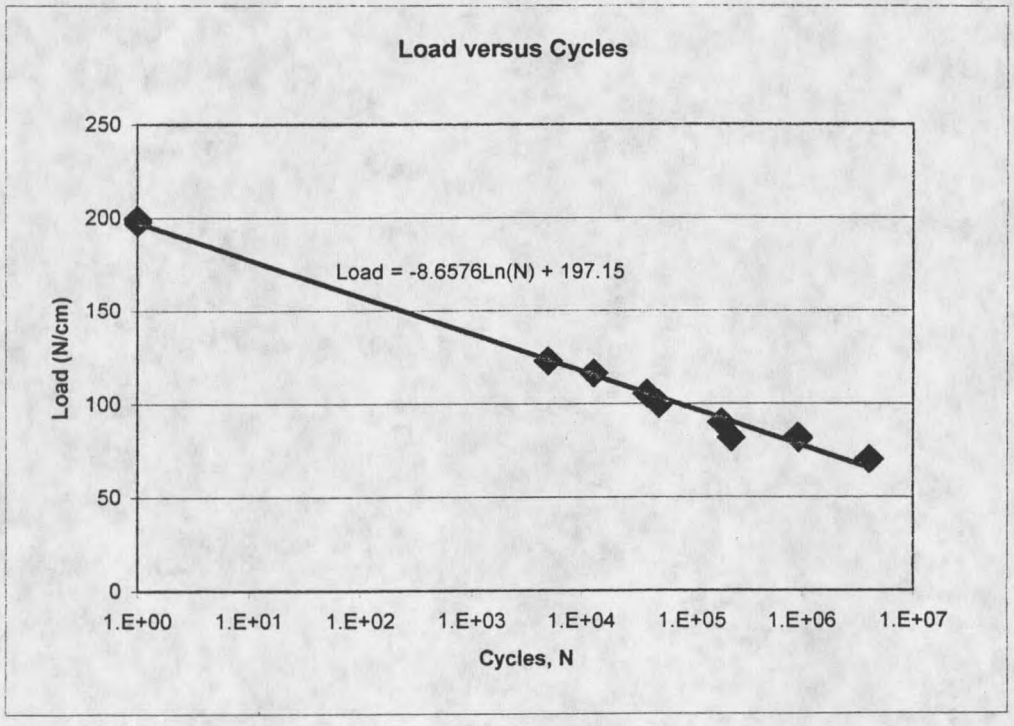


411 Vinylester

Fatigue Skin-Stiffener Specimens

specimen	width (mm)	load level (maximum cyclic load) (N/cm)	Normalized Load (max. cyclic load/ avg. max. static load) (Cyclic/Monotonic)	cycles (cycles to failure failure when max. disp. = 0.43cm)
16T9	24.9	123.0	0.62	4960
16T3	24.1	116.2	0.59	13000
16T6	25.4	99.8	0.50	50360
16T7	24.9	105.4	0.53	39131
16T14	25.4	81.4	0.41	925360
16T12	25.4	82.3	0.41	911320
16T13	25.1	90.0	0.45	183689
16T8	24.6	81.8	0.41	227040
16T11	25.1	70.1	0.35	4056872
Average	25.0	101.3	0.51	
Stand. Deviation	0.5	17.2	0.09	

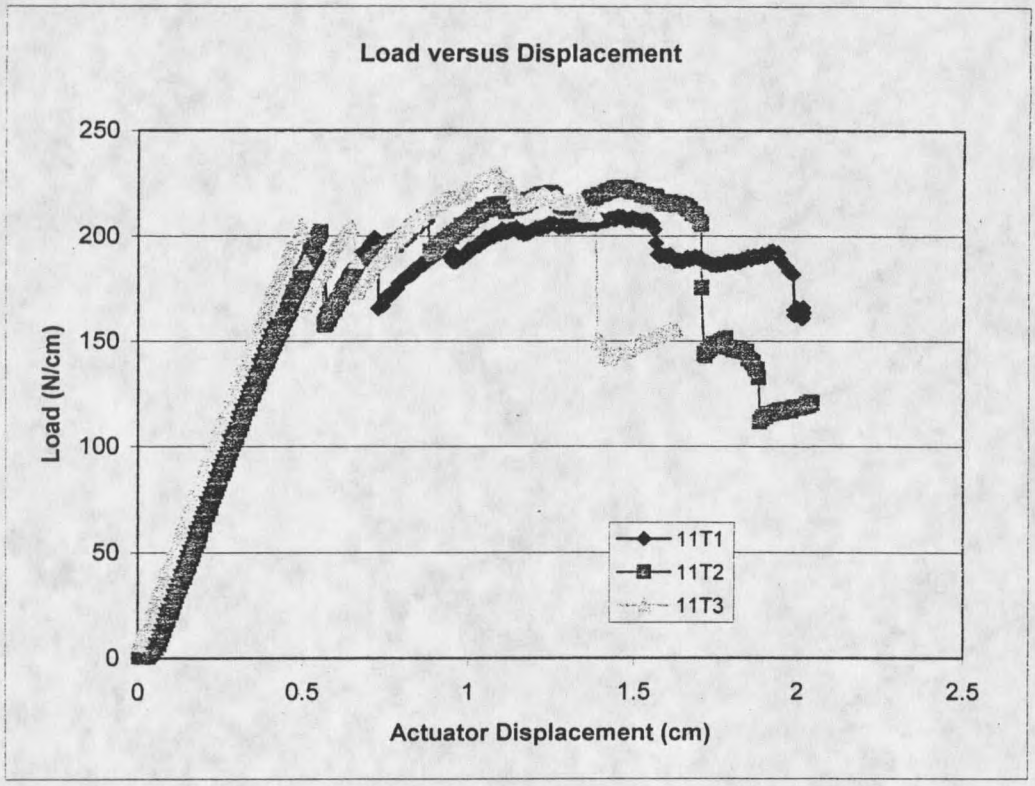
R Value = 0.1



8084 Vinylester

Static Skin-Stiffener Specimens

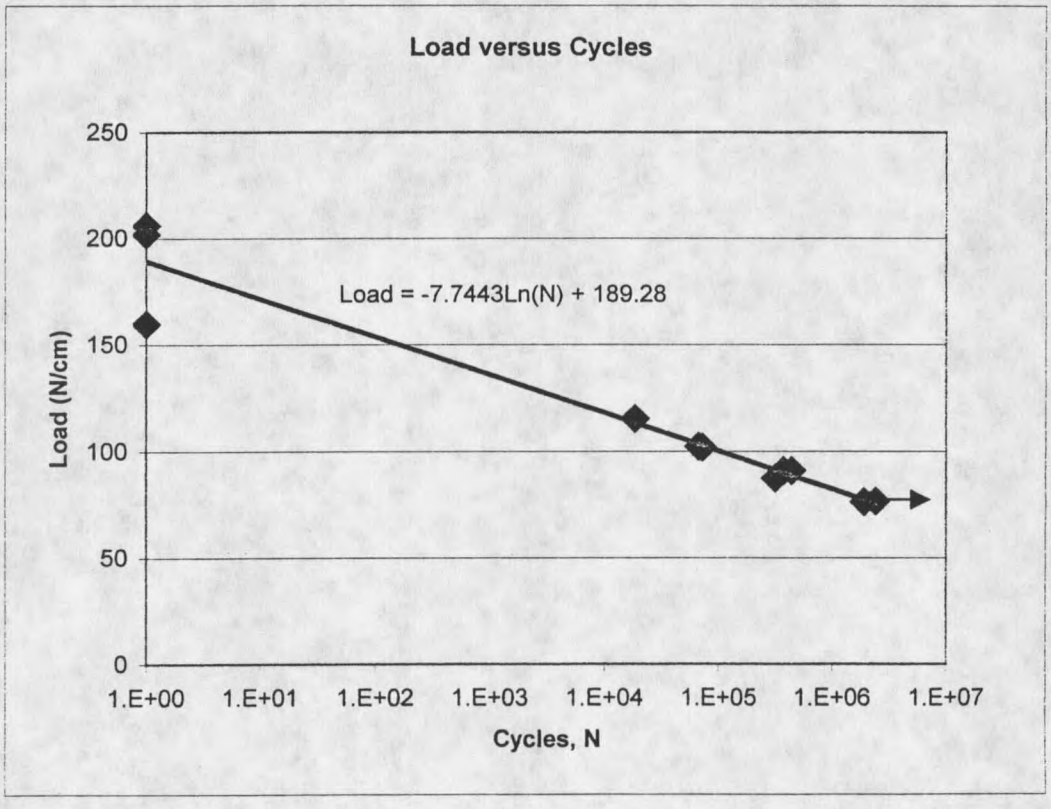
specimen	width (mm)	Load at Initital Damage (N)	Displacement at Initial Damage (mm)	Maximum Load (N/cm)	Displacement at Maximum Load (mm)
11T1	2.5	159.8	3.9	209.5	14.6
11T2	2.5	201.9	5.5	223.1	14.7
11T3	2.5	206.0	4.9	230.4	10.9
Average	2.5	204.0	5.2	221.0	12.8
Stand. Dev.	0.0	2.9	0.4	10.6	2.7



8084 Vinylester
Fatigue Skin-Stiffener Specimens

specimen	width (mm)	load level (maximum cyclic load) (N/cm)	Normalized Load (max. cyclic load/ avg. max. static load) (Cyclic/Monotonic)	cycles (cycles to failure failure when max. disp. = 0.43cm)	
11T9	2.5	115.3	0.52	18420	
11T5	2.5	102.3	0.46	66640	
11T7	2.5	101.9	0.46	71780	
11T4	2.4	91.0	0.41	374640	
11T13	2.4	91.0	0.41	439600	
11T14	2.5	76.3	0.35	1901840	
11T10	2.5	76.7	0.35	2402371	runout
11T11	2.5	87.4	0.40	315930	

R Value = 0.1

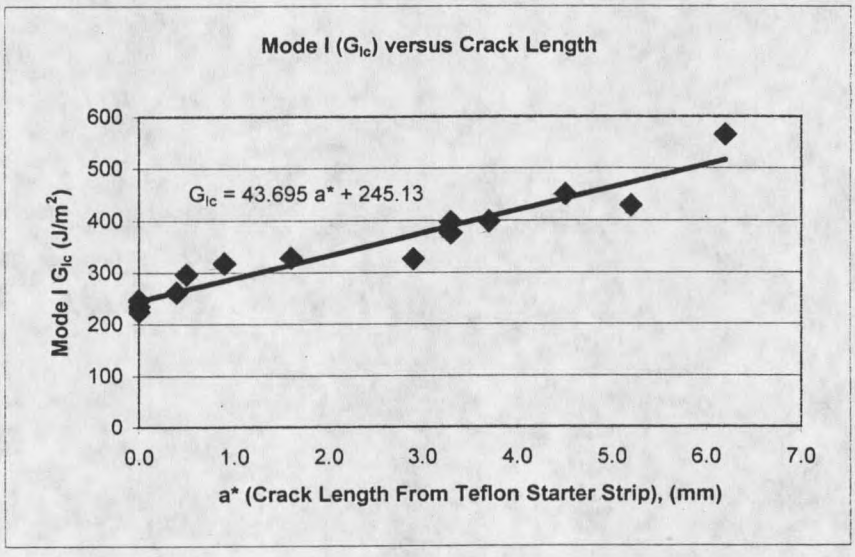


600 Series DCB Monotonic Data

$[(45),90_2,(45)]_4$ Ply Layup

Test Specimen	Total Hinge Distance (mm)	a* (mm)	Max Load (N)	Average Disp. (mm)	Width (mm)	G_{Ic} (J/m^2)
dcb600a	22.5	0.0	113.0	0.8	26.9	234.8
dcb600b	23.0	0.5	123.2	1.0	26.9	296.0
dcb600c	25.4	2.9	127.2	1.2	26.9	326.4
dcb600d	26.2	3.7	136.6	1.4	26.9	398.7
dcb600e	27.7	5.2	139.7	1.5	26.9	428.6
dcb608a	23.8	0.0	107.9	0.9	26.9	224.9
dcb608b	24.2	0.4	114.4	1.0	26.9	261.5
dcb608c	25.4	1.6	122.5	1.2	26.9	328.2
dcb608d	27.1	3.3	133.0	1.4	26.9	396.6
dcb611a	21.1	0.0	114.8	0.8	26.9	246.8
dcb611b	22.0	0.9	123.2	1.0	26.9	317.6
dcb611c	24.4	3.3	132.1	1.2	26.9	376.0
dcb611d	25.6	4.5	137.9	1.5	26.9	450.4
dcb611e	27.3	6.2	151.2	1.8	26.9	565.2

a*=distance from the teflon starter strip

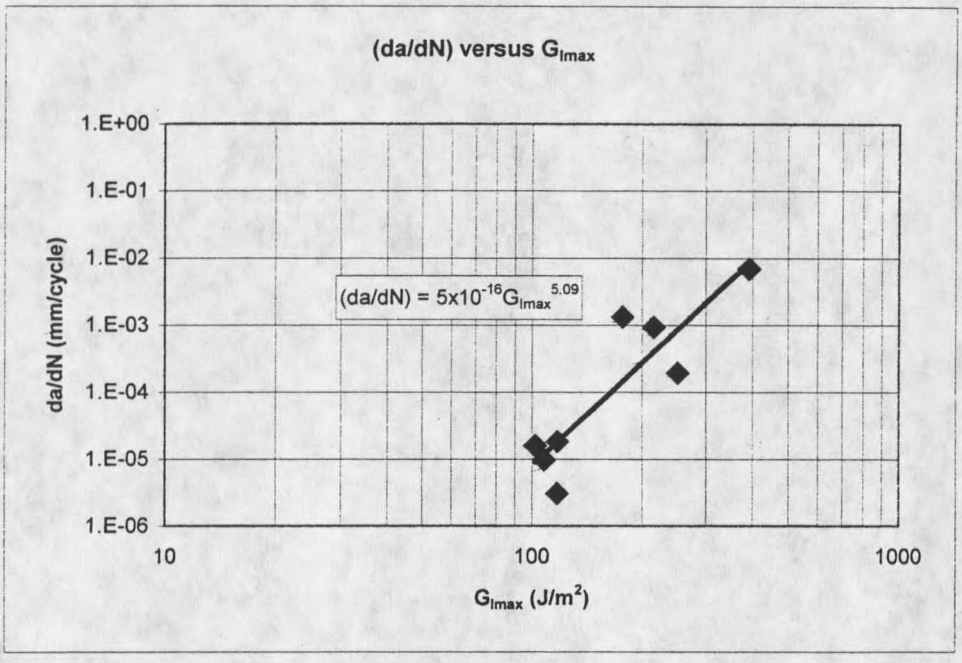


600 Series DCB Fatigue Data

$[(45),90_2,(45)]_4$ Ply Layup

Test Specimen	Average Overall Crack (mm)	a* Initial Crack (mm)	a* Final Crack (mm)	Max Load (N)	Initial Disp. (mm)	Final Disp. (mm)	Cycles	da/dN (mm/cycle)	G_{Ic} (J/m^2)	Width (mm)
dcb613	21.2	0.7	0.9	62.2	0.7	0.8	65208	3.07E-06	117.0	26.9
dcb621	27.8	0.7	1.8	77.0	2.5	2.6	158	6.96E-03	391.8	26.9
dcb610	24.5	0.4	0.6	67.2	0.8	0.8	10848	1.84E-05	117.4	26.9
dcb612	22.7	0.4	1.7	63.2	0.7	0.7	132755	9.79E-06	107.9	27.2
dcb616	26.9	0.6	2.0	77.0	1.4	1.7	7205	1.94E-04	249.7	26.9
dcb620	26.1	2.0	2.5	95.5	1.0	1.1	572	9.27E-04	214.8	26.9
dcb604	29.8	1.6	2.9	87.0	1.0	1.1	1019	1.32E-03	176.5	26.9
dcb602	32.2	3.5	4.8	67.2	0.9	0.9	80276	1.59E-05	102.1	26.9

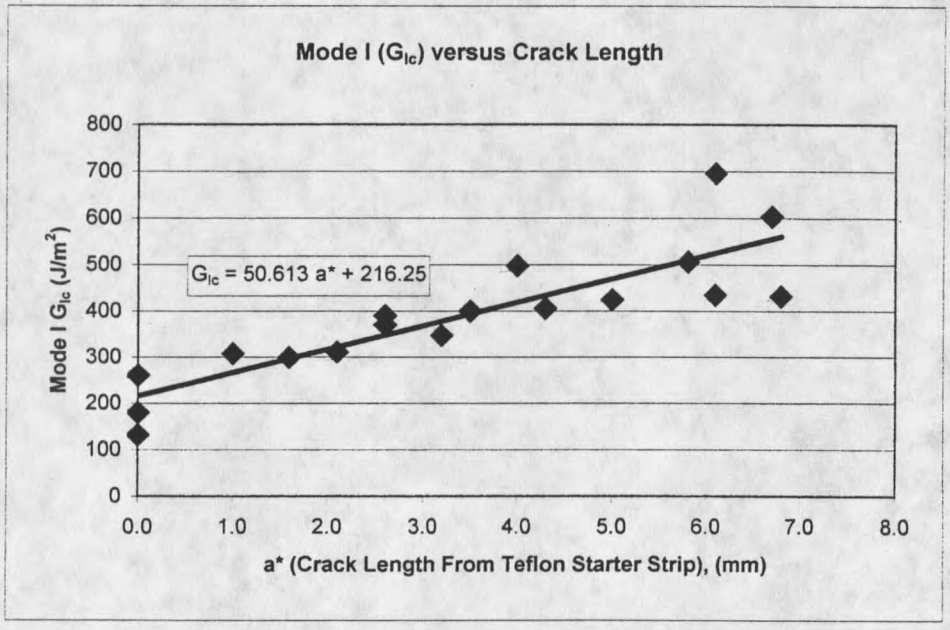
a*=distance from the teflon starter strip



700 Series DCB Monotonic Data
$[(45)_9, 90, (45)_8]$ Layup

Specimen	Total Hinge Distance (mm)	a* (mm)	Max Load (N)	Average Disp. (mm)	Width (mm)	G_{Ic} (J/m^2)
dcb705	37.3	5.0	87.3	3.1	25.4	424.1
dcb751	38.0	0.0	62.7	1.9	25.4	180.6
dcb751b	39.0	1.0	76.3	2.7	25.4	308.1
dcb751c	41.2	3.2	79.6	3.0	25.4	347.5
dcb751d	42.0	4.0	91.2	3.9	25.4	498.0
dcb752	38.0	0.0	56.0	1.5	25.4	132.3
dcb752b	40.1	2.1	81.1	2.6	25.4	311.4
dcb752c	42.3	4.3	91.0	3.2	25.4	405.5
dcb752d	44.1	6.1	92.5	3.5	25.4	434.6
dcb750c	40.6	2.6	96.5	2.6	25.4	370.2
dcb750d	44.8	6.8	99.1	3.3	25.4	431.6
dcb780a	42.7	0.0	64.5	2.9	25.4	260.9
dcb780b	44.3	1.6	66.5	3.4	25.4	299.8
dcb780c	46.2	3.5	74.6	4.2	25.4	400.0
dcb780d	48.5	5.8	83.0	5.0	25.4	505.9
dcb780e	49.4	6.7	87.8	5.7	25.4	603.5
dcb781a	40.9	2.6	81.8	3.3	25.4	390.1
dcb781b	44.4	6.1	104.1	5.0	25.4	696.1

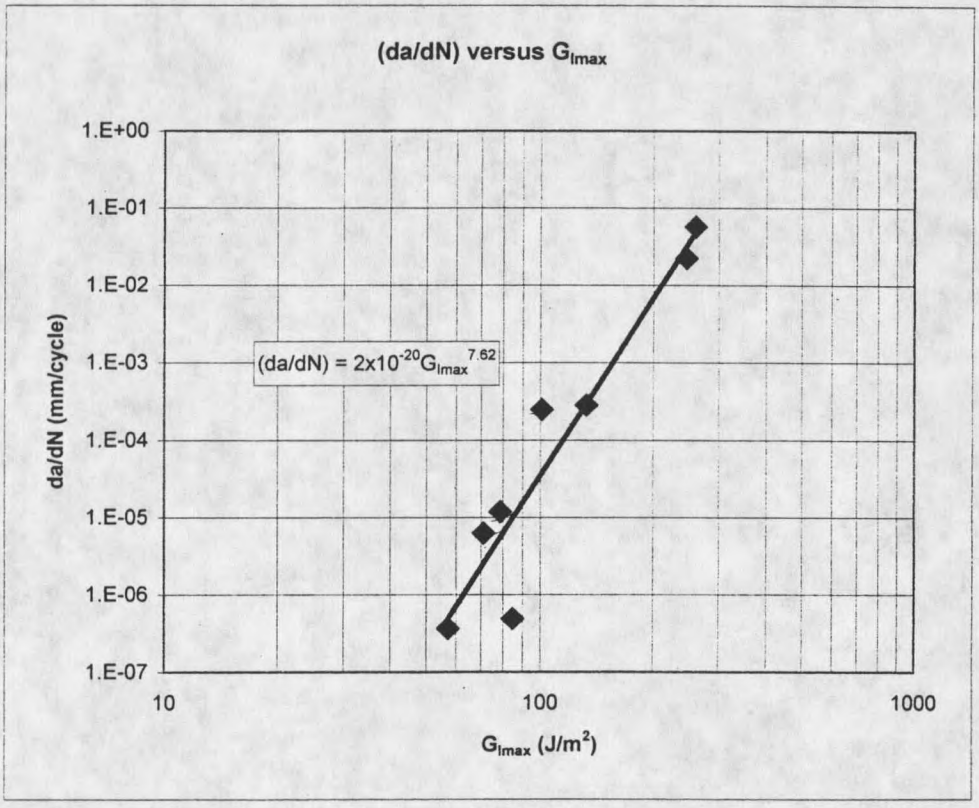
a*=distance from the teflon starter strip



700 Series DCB Fatigue Data
$[(45)_9, 90, (45)_8]$ Layup

Test Specimen	Average Overall Crack (mm)	a* Initial Crack (mm)	a* Final Crack (mm)	Max Load (N)	Initial Disp. (mm)	Final Disp. (mm)	Cycles	da/dN (mm/cycle)	G_{Ic} (J/m^2)	Width (mm)
dcb706	42.4	3.5	7.7	68.1	2.4	2.8	188	2.23E-02	244.5	25.7
dcb701	44.1	1.6	1.9	36.3	1.6	1.9	614691	4.88E-07	84.7	25.7
dcb702	41.2	0.5	0.8	45.8	1.4	1.7	1207	2.49E-04	100.8	25.7
dcb703	38.8	2.3	4.5	41.7	1.1	1.4	186960	1.18E-05	78.6	25.7
dcb704	40.8	1.3	3.0	35.8	1.3	1.4	270352	6.29E-06	71.0	25.1
dcb708	42.3	5.5	6.1	31.5	1.2	1.4	1642000	3.65E-07	57.1	25.4
dcb707	39.3	3.5	5.0	55.4	1.5	1.7	5262	2.85E-04	132.5	25.7
dcb700	39.9	0.8	4.9	68.6	2.5	2.6	72	5.74E-02	259.1	25.7

a*=distance from the teflon starter strip



800 Series ENF Monotonic Data
$[(45)_9, 90, (45)_8]$ Layup

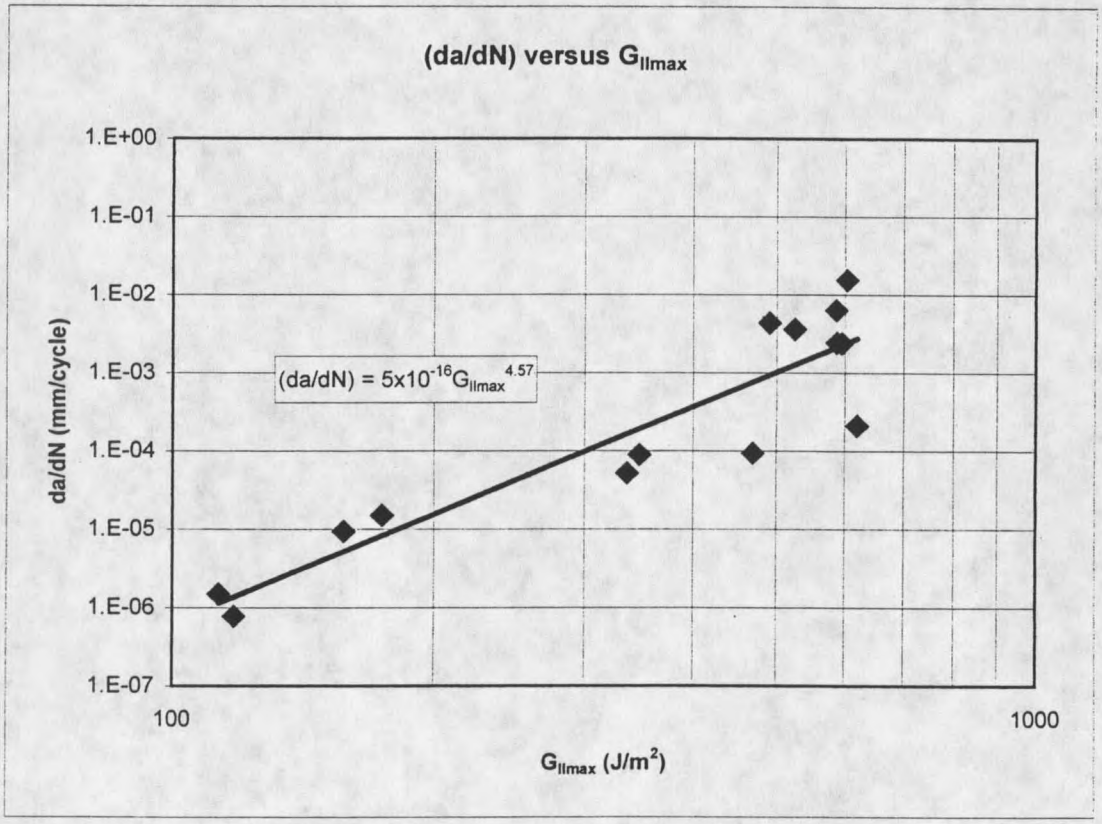
Sample	Crack Length (mm)	a* (mm)	Max Load (N)	Average Disp. (mm)	Width (mm)	Height (mm)	G_{IIc} (J/m^2)
ENF831	25.7	1.6	873.1	2.7	24.1	24.1	762.5
ENF828	27.3	0.9	854.0	2.7	26.4	24.1	822.1
ENF827	28.1	0.7	1054.2	2.8	27.4	23.9	1240.8

a*=distance from the teflon starter strip

800 Series ENF Fatigue Data
$[(45)_9, 90, (45)_8]$ Layup

Test Coupon	Average Overall Crack (mm)	a* Initial Crack (mm)	a* Final Crack (mm)	Max Load (N)	Initial Disp. (mm)	Final Disp. (mm)	Cycles	da/dN (mm/cycle)	G_{IIc} (J/m^2)	Width (mm)
ENF713	32.2	1.0	4.0	650.7	2.4	2.9	14233	2.11E-04	619.9	25.1
ENF714	35.5	0.9	6.0	522.4	2.0	2.3	54707	9.32E-05	469.6	25.3
ENF716	25.5	1.3	2.5	443.1	1.5	1.7	80000	1.50E-05	174.3	25.4
ENF818	31.3	1.4	4.3	503.5	1.9	2.1	56009	5.18E-05	335.9	24.4
ENF819	27.8	1.4	3.4	551.1	1.9	2.1	22329	8.96E-05	347.2	24.4
ENF817	26.9	1.7	3.4	383.3	1.4	1.6	181578	9.36E-06	157.7	24.4
ENF823	27.2	1.0	3.7	722.8	2.7	2.8	427	6.32E-03	585.7	24.1
ENF824	27.3	0.8	3.6	741.0	2.7	2.8	1174	2.39E-03	595.0	24.6
ENF829	28.1	1.0	4.3	702.8	2.7	2.9	1356	2.43E-03	587.0	24.1
ENF830	26.9	1.5	3.6	723.7	2.6	2.7	585	3.59E-03	524.8	24.1
ENF840	26.2	1.4	2.7	734.8	2.7	2.8	298	4.36E-03	490.3	24.6
ENF841	27.4	1.8	5.2	771.4	2.8	2.8	219	1.55E-02	603.2	24.4
ENF842	25.8	0.8	1.1	364.7	2.6	2.7	385316	7.79E-07	117.7	24.6
ENF845	23.9	1.1	1.9	391.4	1.4	1.6	536447	1.49E-06	113.1	24.9

a*=distance from the teflon starter strip



APPENDIX B

SAMPLE CALCULATIONS

APPENDIX B

PART A

STATIC SAMPLE CALCULATION

- Mode I G_I versus crack length emperical relation derived from experimental DCB Monotonic Tests :

$G_{ModeI} = 50.61\,a + 216.25$

$216.25 + 50.61\,a$

- (Mode II G_{II} constant in relation to crack length)

- Desired Crack Length to be analyzed (mm) :

$a = 3;$

- Experimental Mode I & II Energies (J / m^2) resulting from Inverse of Emperical Relationships of crack length versus G :

$G_{ModeI} = 50.61\,a + 216.25$

368.08

$G_{ModeII} = 941.8$

941.8

- Load applied to the model by the designer (N / cm) :

$P_{model} = 128;$

- Numerical Mode I & II Energies (J / m^2) :

$G_{ModeI\text{-}Num} = 143;$
$G_{ModeII\text{-}Num} = 141;$

- Interaction Criterion to Determion Ratio Sum (F) :

$$F = \left(\frac{G_{ModeI\text{-}Num}}{G_{ModeI}}\right)^{\frac{1}{2}} + \left(\frac{G_{ModeII\text{-}Num}}{G_{ModeII}}\right)^{\frac{1}{2}}$$

1.01023

- **Predicted Load (N / cm) :**

$$P_{predict} = \left(\frac{1}{F}\right)^{\frac{1}{2}} P_{model}$$

127.35

APPENDIX B

PART B

FATIGUE SAMPLE CALCULATION

- **Mode I (da / dN) versus G_I emperical relation derived from experimental DCB Fatigue Tests :**

$$\text{Equation1} = (\Delta a \Delta N_{\text{ModeI}}) == 2 * 10^{-20} * G_{\text{ModeI}}^{7.6239}$$

$$\Delta a \Delta N_{\text{ModeI}} == \frac{G_{\text{ModeI}}^{7.6239}}{50000000000000000000}$$

- **Inverse of (da / dN) versus G_I :**

```
Solve[Equation1, GModeI]
```

$$\{\{G_{\text{ModeI}} \to 383.57\, \Delta a \Delta N_{\text{ModeI}}^{0.131166}\}\}$$

- **Mode II (da / dN) versus G_{II} emperical relation derived from experimental ENF Fatigue Tests :**

```
Equation2 = (ΔaΔNModeII) == 5*10^-16*GModeII^4.5765
```

$$\Delta a \Delta N_{\text{ModeII}} == \frac{G_{\text{ModeII}}^{4.5765}}{2000000000000000}$$

- **Inverse of (da / dN) versus G_{II} :**

```
Solve[Equation2, GModeII]
```

$$\{\{G_{\text{ModeII}} \to 2204.91\, \Delta a \Delta N_{\text{ModeII}}^{0.218508}\}\}$$

- **Rate for crack tip to grow chosen by the designer (mm / cycle) :**

```
ΔaΔNModeI = 9.47*10^-5
```

0.0000947

```
ΔaΔNModeII = 9.47*10^-5
```

0.0000947

- **Experimental Mode I & II Energies resulting from Inverse of Emperical Relationships (J / m^2) :**

$G_{ModeI} = 383.5696\ (\Delta a \Delta N_{ModeI})^{0.131166}$

113.783

$G_{ModeII} = 2204.9\ (\Delta a \Delta N_{ModeII})^{0.21850}$

291.22

- **Load applied to the model by the designer (N / cm) :**

$P_{model} = 78.8;$

- **Numerical Mode I & II Energies (J / m^2) :**

$G_{ModeI\text{-}Num} = 58.5;$
$G_{ModeII\text{-}Num} = 42.5;$

- **Interaction Criterion to Determion Ratio Sum (F) :**

$$F = \left(\frac{G_{ModeI\text{-}Num}}{G_{ModeI}}\right)^{\frac{1}{2}} + \left(\frac{G_{ModeII\text{-}Num}}{G_{ModeII}}\right)^{\frac{1}{2}}$$

1.09905

- **Predicted Load (N / cm) :**

$$P_{predict} = \left(\frac{1}{F}\right)^{\frac{1}{2}} P_{model}$$

75.1653

APPENDIX C
DETERMINATION OF FEA INITIAL CRACK LENGTH

```
<<NumericalMath`PolynomialFit`
```

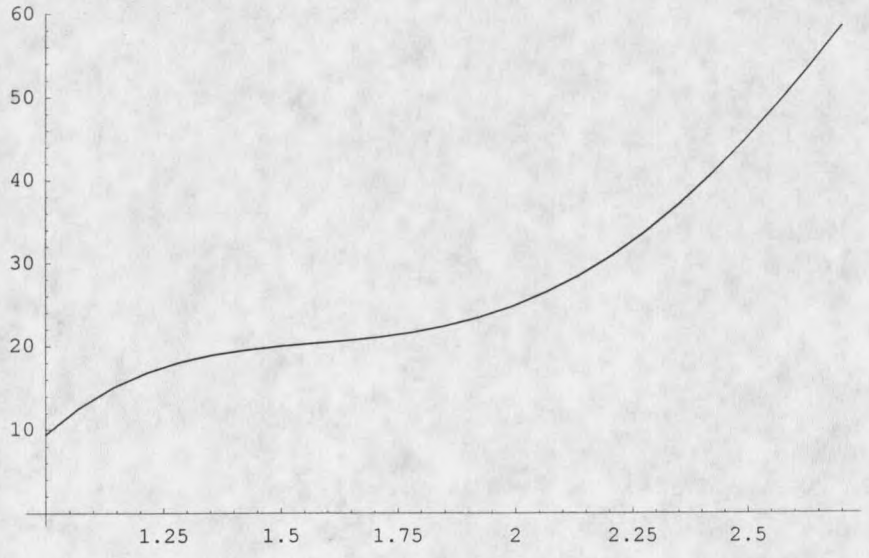
5th order polynomial that fits the Mode I G_I data (Figure 59).

```
g1 =
PolynomialFit[{{1.09,13.25},{1.46,19.74},{2.13,28.37},{2.7,58.75},
{4.5,10.72}},5];

Expand[g1[x]]
```

$$-211.436 + 484.68\,x - 370.825\,x^2 + 120.097\,x^3 - 13.1529\,x^4$$

```
Plot[g1[x], {x, 1, 2.7}];
```




```
<<NumericalMath`PolynomialFit`
```

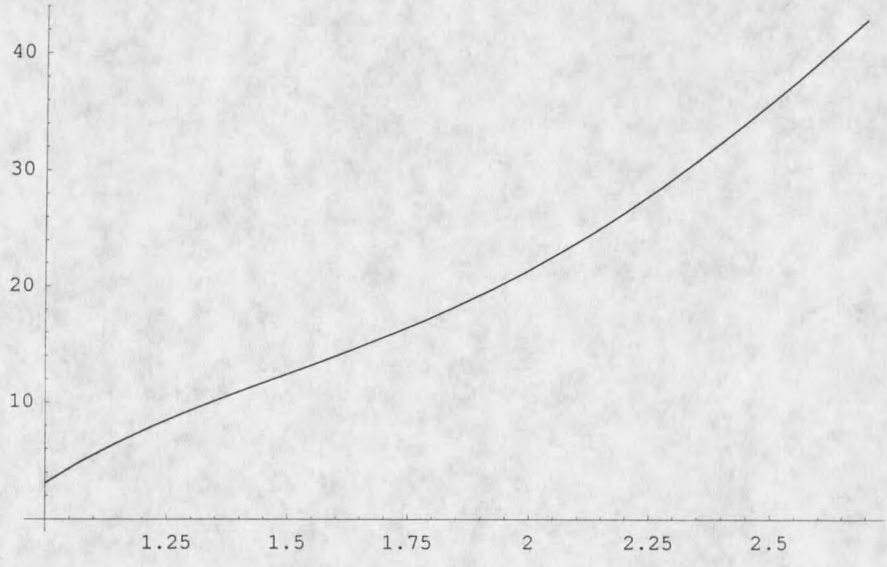
5th order polynomial that fits the Mode II G_{II} data (Figure 59).

```
g2 =
PolynomialFit[{{1.09,5.25},{1.46,11.81},{2.13,24.55},{2.7,43.04},{
4.5,2.54}},5];

Expand[g2[x]]
```

$$-78.3085 + 168.775\,x - 125.469\,x^2 + 43.057\,x^3 - 5.02718\,x^4$$

```
Plot[g2[x], {x, 1, 2.7}];
```



5th order polynomial that fits the Mode I G_I verus a for 79 N/cm Applied Load data (Figure 59) in Bend Region of FEA Skin-Stiffener Model:

```
G1 = -211.436 + 484.68 * a - 370.825 * a^2 + 120.097 * a^3 - 13.1529 * a^4;
```

5th order polynomial that fits the Mode II G_{II} verus a for 79 N/cm Applied Load data (Figure 59) in Bend Region of FEA Skin-Stiffener Model:

```
G2 = 78.3085 + 168.775 * a - 125.469 * a^2 + 43.057 * a^3 - 5.02718 * a^4;
```

Interaction Criterion:

```
Equation3 = ((G1/G1c)^(1/2) + (G2/G2c)^(1/2)) == F;
```

Experimental Mode I GI versus Crack Length Relation for Experimental DCB data (Figure 33).

```
G1c = 50.613 * a + 216.25;
```

Experimental Mode II GII for Experimental ENF data (Table 5).

```
G2c = 941.8;
```

G versus Load Squared Relation:

```
Equation6 = Pcrit == (1/F)^(1/2) * 79;
```

Experimental "Pop-in" Load for Skin Stiffener:

```
Pcrit = 94.9;
```

Determination of Minimum Crack Length for Insertion into the FEA Skin-Stiffener Model:

```
Solve[{Equation3, Equation6}, {a, F}]
```

```
{{F → 0.692982, a → 1.45375 - 0.347503 i},
 {F → 0.692982, a → 1.45375 + 0.347503 i},
 {F → 0.692982, a → 1.73935}, {F → 0.692982, a → 4.43627}}
```

Smallest real root gives a crack length of 1.73 mm (actual experimental Crack Length was 2.0 mm).

APPENDIX D
SAMPLE FEA BATCH FILE

```
!  sample batch file for a Mode I DCB test

/prep7


!  Element Type--Plane82--Plane Strain
et,1,plane82
keyopt,1,3,2


!  variables
!  height of enf
h=0.3295
t1=0.1725
t2=h-t1
t3=0.02756

!  crack length
a=1.74
!  length of specimen
l=6

!  Skin and Flange Material Properties  45's
!  Material Set #1
mp,ex,1,1.713e6
mp,ey,1,1.15e6
mp,ez,1,1.713e6
mp,gxy,1,.1068e7
mp,gyz,1,.5973e6
mp,gxz,1,.6636e6
mp,nuxy,1,0.288
mp,nuyz,1,0.288
mp,nuxz,1,0.434

!  Skin and Flange Material Properties  0's
!  Material Set #2
mp,ex,2,1.29e6
mp,ey,2,1.29e6
mp,ez,2,5.00e6
mp,gxy,2,6.636e5
mp,gyz,2,6.636e5
mp,gxz,2,6.636e5
mp,nuxy,2,0.29
mp,nuyz,2,0.29
mp,nuxz,2,0.29
```

```
!  Keypoints for thin  section
k,1,0,0,0
k,2,a-0.2,0,0
k,3,a,0,0
k,4,a+0.2,0,0
k,5,l,0,0
k,6,l,t1,0
k,7,a+0.2,t1,0
k,8,a,t1,0
k,9,a-0.2,t1,0
k,10,0,t1,0
k,11,0,0,0
k,12,a-0.2,0,0
k,13,0,-t2,0
k,14,a-0.2,-t2,0
k,15,a,-t2,0
k,16,a+0.2,-t2,0
k,17,l,-t2,0
k,18,a+0.2,t3,0
k,19,a,t3,0
k,20,a-0.2,t3,0
k,21,0,t3,0
k,22,l,t3,0

!k,100,0,0,-1

!create cart. coord. system
!cskp,12,0,1,2,100

!create areas
a,21,20,9,10  !area 1
a,20,19,8,9  !area 2
a,19,18,7,8  !area 3
a,18,22,6,7  !area 4
a,11,12,14,13  !area 5
a,12,3,15,14  !area 6
a,3,4,16,15
a,4,5,17,16
a,1,2,20,21
a,2,3,19,20
a,3,4,18,19
a,4,5,22,18
```

```
esize,h/8


!  Turn on mapped meshing
mshkey,1

!  mesh 90 plies
mat,2
amesh,9,12,1

!  mesh 45 plies
mat,1
amesh,1,4,1
amesh,5,8,1

/solu

!apply ux=0 on top of dcb
allsel
nsel,s,loc,x,0,0.001
nsel,r,loc,y,t1-0.001,t1
d,all,ux,0

!apply nodal force
f,all,fy,14.9


!apply ux=0 on top of dcb
allsel
nsel,s,loc,x,0,0.001
nsel,r,loc,y,-t2+0.001,-t2
d,all,ux,0

d,all,uy,0

allsel

!  Solving Time Steps and Nonlinear Deformation
 nlgeom,on
 time,11
 deltim,5
 neqit,10

! /solu
```

APPENDIX E
DATA ACQUISTION PROGRAMS

Time Delay
10.000000

Time In Seconds
1.984000

Max Load, In pounds
0.488281

Load Offset
0.000000

Min Load, In pounds
-0.549316

Max. Position, Inches
0.102539

Position Offset
0.000000

Min. Position, Inches
0.100098

format (%.6f)
%.6f

Transpose Array?
don't transpose

append to file

The Save box
C:\fatigue data\fatigue\cal.dat

Max Compressive Strain 1
0.00000000

Min compressive Strain 1
0.00000000

Strain Offset
0.00000000

First put cal.dat in the save box below.
Second, Make the position offset 0.00000000
Third, run the program once, with the single arrow right below the edit pull down menu.
Fourth, copy the min position inches into the position offset box.
Fifth, run again. The min and max positions should be equal to zero (or pretty close)
Sixth, change cal.dat to the appropriate file name.
Seventh, hit the run continuous button (right in between the single arrow and the stop sign). It will save data until you stop it now, in the file you told it to save it in.
By the way, the stop sign stops testing.

Input channels
0:2

device
2

scan rate
10000.00

strain input channels
0:2

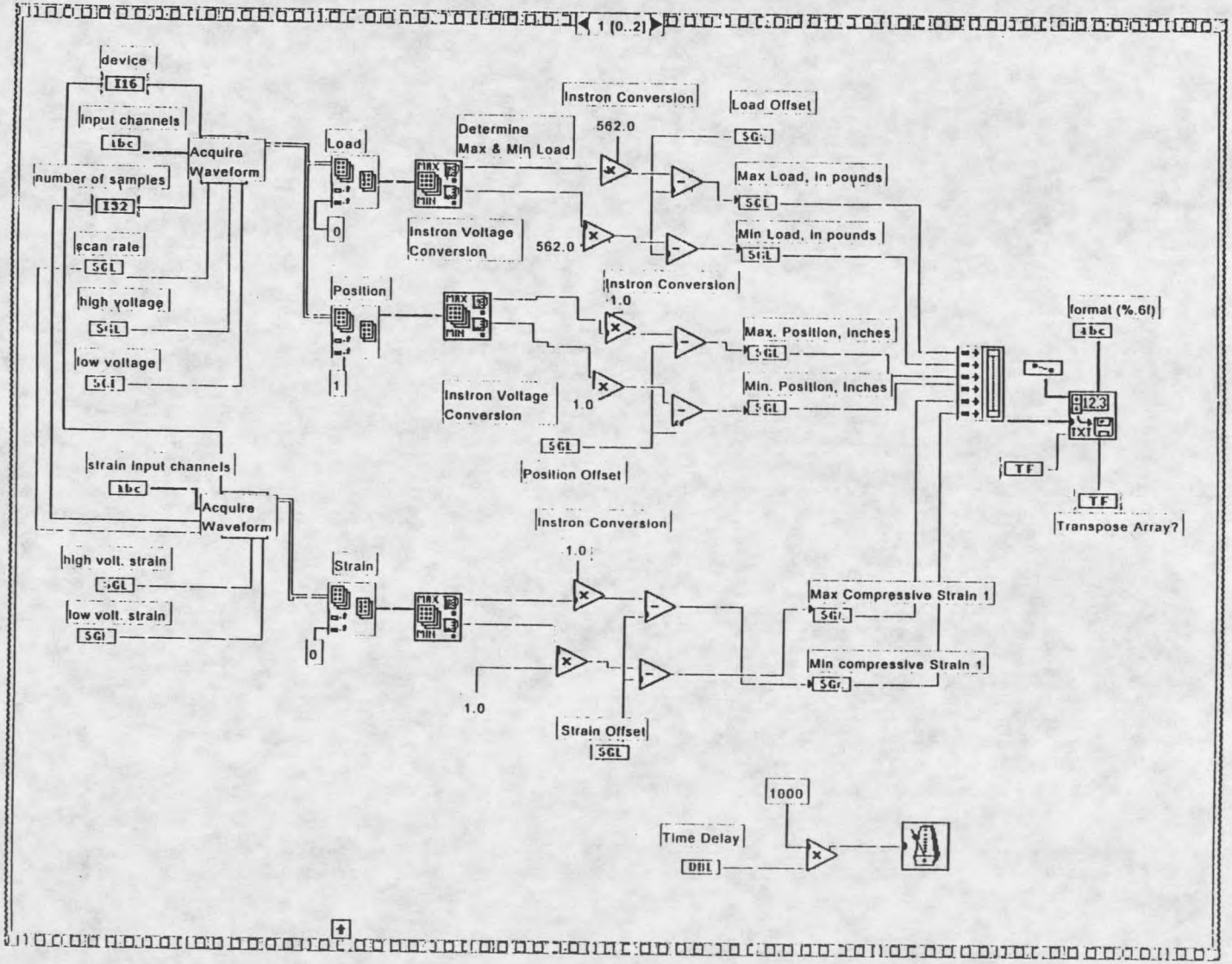
number of samples

high voltage
0.00

low voltage
0.25

high volt. strain
0.00

low volt. strain
0.25


1 (0..2)
device
I16
input channels
abc
Acquire Waveform
number of samples
I32
scan rate
SGL
high voltage
SGL
low voltage
SGL
Load
0
Determine Max & Min Load
Instron Conversion
562.0
Load Offset
SGL
Max Load, in pounds
SGL
Instron Voltage Conversion
562.0
Min Load, in pounds
SGL
Position
1
Instron Conversion
1.0
Max. Position, inches
SGL
Instron Voltage Conversion
1.0
Min. Position, inches
SGL
SGL
Position Offset
format (%.6f)
abc
TF
Transpose Array?
strain input channels
abc
Acquire Waveform
high volt. strain
SGL
low volt. strain
SGL
Strain
0
Instron Conversion
1.0
Max Compressive Strain 1
SGL
1.0
Min compressive Strain 1
SGL
Strain Offset
SGL
1000
Time Delay
DBL

0 [0..2]

MONTANA STATE UNIVERSITY - BOZEMAN
3 1762 10340652 4